

High Pressure Ignition Chemistry of Alternative Fuels

Bryan William Weber, Ph.D.

University of Connecticut, 2014

Abstract

High Pressure Ignition Chemistry of Alternative Fuels

Bryan William Weber

B.S., Case Western Reserve University, 2009

M.S., University of Connecticut, 2010

A Dissertation

Submitted in Partial Fulfillment of the
Requirements for the Degree of Doctor of Philosophy
at the
University of Connecticut

2014

Copyright ©2014 Bryan William Weber



This work is licensed under a Creative Commons Attribution-NonCommercial-NoDerivatives 4.0 International License.

http://creativecommons.org/licenses/by-nc-nd/4.0/deed.en_US

APPROVAL PAGE
Doctor of Philosophy Dissertation
High Pressure Ignition Chemistry of Alternative Fuels

Presented by
Bryan William Weber, B.S., M.S.

Major Advisor _____

Chih-Jen Sung

Associate Advisor _____

Baki Cetegen

Associate Advisor _____

Michael Renfro

University of Connecticut

2014

Acknowledgements

So long, and thanks for all the fish.

Contents

Acknowledgements	ii
Contents	iii
List of Figures	vi
List of Tables	xi
Chapter 1 Introduction	1
1.1 Background.....	1
1.2 Recent Work on the Combustion of Alcohols	5
1.3 Recent Work on Ignition of Methylcyclohexane	9
1.4 Summary.....	11
1.5 Organization of this Work.....	12
Chapter 2 Experimental Facilities	13
2.1 Rapid Compression Machine	13
2.1.1 Experimental Procedure.....	13
2.1.2 Test Gas Mixture Preparation	18
2.1.3 Definition of Ignition Delay.....	19
2.1.4 Non-Reactive Experiments	20
2.1.5 Reaction Chamber Homogeneity.....	21
2.1.6 Determination of Reactant Temperature	21
2.1.7 Determination of Compressed Temperature	23

2.1.8	Uncertainty of Ignition Delay and Compressed Temperature	25
2.1.8.1	Uncertainty in Initial Temperature	28
2.1.8.2	Uncertainty in Initial Pressure	28
2.1.8.3	Uncertainty in Compressed Pressure	29
2.1.8.4	Uncertainty in the Specific Heat.....	30
2.2	Fast Sampling System.....	33
2.2.1	Experimental Procedure.....	35
2.3	Gas Chromatograph/Mass Spectrometer	36
2.3.1	Theory of Gas Chromatography/Mass Spectrometry	36
2.3.1.1	Gas Chromatography	36
2.3.1.2	Mass Spectrometry	38
2.3.2	Identification and Quantification of Species using GC/MS	40
2.3.3	Experimental Procedure.....	41
Chapter 3	The Butanol Isomers	43
3.1	Structure of the Butanol Isomers	43
3.2	Experimental Procedure	44
3.3	Experimental Results	45
3.4	Simulation Results	49
3.5	Discussion.....	52
3.6	Conclusions.....	61
Chapter 4	<i>i</i>-Pentanol	63
4.1	Structure of <i>i</i> -Pentanol	63
4.2	Procedures.....	64
4.3	Model Improvements	65
4.4	Experimental & Modeling Results	66
4.5	Discussion.....	68
4.6	Conclusions.....	72

Chapter 5 Methylcyclohexane	74
5.1 Structure of Methylcyclohexane	74
5.2 Procedures	74
5.3 Model Improvements	75
5.4 Experimental Results	76
5.5 Comparison to Model	77
5.6 Discussion	82
5.6.1 Path Analysis	82
5.6.2 Sensitivity Analysis	86
5.7 Conclusions	92
Chapter 6 Conclusions and Future Directions	94
References	95
Appendix A Definition of Species Names in the Methylcyclohexane Mechanism	108
Appendix B CanSen	131

List of Figures

2.1	Schematic of the RCM. Not to scale	15
2.2	Photograph of the RCM.	16
2.3	Representative pressure trace indicating the definition of the first stage and overall ignition delays and the corresponding non-reactive pressure trace. EOC stands for End of Compression.	20
2.4	Creviced piston installed in the present RCM.	22
2.5	GC/MS sample injection valve.	38
2.6	Schematic of the transmission quadrupole in an MS.	39
2.7	Example mass spectrum for a given scan during a GC/MS analysis	41
2.8	Example TIC for a GC/MS analysis	41
3.1	Skeletal structures of the butanol isomers	43
3.2	Ignition delays of the four isomers of butanol at compressed pressure $P_C = 15$ bar. Dashed lines are least squares fits to the data.	47
3.3	Ignition delays of the four isomers of butanol at compressed pressure $P_C = 30$ bar. Dashed lines are least squares fits to the data.	47
3.4	Pressure traces of the 15 bar <i>t</i> -butanol experiments, in stoichiometric air.	48
3.5	Pressure traces of the 30 bar <i>t</i> -butanol experiments, in stoichiometric air.	48
3.6	Ignition delays of three equivalence ratios of <i>t</i> -butanol in air, for $P_C = 30$ bar. Lines represent least squares fits to the data.	49

3.7	Pressure traces of the 30 bar <i>t</i> -butanol experiments, $\phi = 0.5$ in air.	50
3.8	Pressure traces of the 30 bar <i>t</i> -butanol experiments, $\phi = 2.0$ in air.	50
3.9	$P_C = 15$ bar, stoichiometric mixtures in air. Comparison of VPRO simulations using the kinetic mechanism of Sarathy et al. [119] with experimental ignition delays.	51
3.10	$P_C = 30$ bar, stoichiometric mixtures in air. Comparison of VPRO simulations using the kinetic mechanism of Sarathy et al. [119] with experimental ignition delays.	51
3.11	Comparison of VPRO simulations using the kinetic mechanism of Sarathy et al. [119] (solid lines) and the MIT mechanism [34, 120] (dotted lines) with the experimental ignition delay results (dashed lines) for stoichiometric mixtures of <i>i</i> -butanol in air at $P_C = 15$ bar (squares) and $P_C = 30$ bar (circles).	52
3.12	Comparison of the simulations using the kinetic mechanism of Sarathy et al. [119] for three equivalence ratio mixtures of <i>t</i> -butanol in air at $P_C = 30$ bar.	52
3.13	Pressure traces of selected <i>t</i> -butanol experiments compared with the corresponding non-reactive and simulated traces, using the mechanism of Sarathy et al. [119].	53
3.14	Pathway analysis for simulations of <i>n</i> -butanol at temperature of 750 K, in stoichiometric air, using the mechanism of Sarathy et al. [119]. Percentages in normal text represent an initial condition of 15 bar; bold text is for 30 bar.	54
3.15	Pathway analysis for simulations of <i>s</i> -butanol at temperature of 750 K, in stoichiometric air, using the mechanism of Sarathy et al. [119]. Percentages in normal text represent an initial condition of 15 bar; bold text is for 30 bar.	54
3.16	Pathway analysis for simulations of <i>t</i> -butanol at temperature of 750 K, in stoichiometric air, using the mechanism of Sarathy et al. [119]. Percentages in normal text represent an initial condition of 15 bar; bold text is for 30 bar.	54
3.17	Pathway analysis for simulations of <i>i</i> -butanol at temperature of 750 K, in stoichiometric air, using the mechanism of Sarathy et al. [119]. Percentages in normal text represent an initial condition of 15 bar; bold text is for 30 bar.	54

3.18 Total cumulative heat release and cumulative heat release by important reactions (inset) as a function of fuel consumption from a simulation using the mechanism of Sarathy et al. [119] with initial conditions of 750 K and 30 bar, in stoichiometric air. See Fig. 3.19 for definitions of reactions in the inset.	56
3.19 Reactions causing the most heat release in the ignition of the butanol isomers. The reaction number refers to Fig. 3.18.	56
3.20 Linear brute force sensitivity analysis of the ignition delay with respect to the A-factors of the listed reactions in the mechanism from Sarathy et al. [119]. Positive quantities indicate the ignition delay is increased when the A-factor is halved.	59
 4.1 Skeletal structure of <i>i</i> -pentanol	63
4.2 Shock tube and RCM ignition delay times from Tsujimura et al. [77] at 7 atm compared with model predictions by the model from Sarathy et al. [75].	67
4.3 Shock tube and RCM ignition delay times from Tsujimura et al. [77] at 20 atm compared with model predictions by the model from Sarathy et al. [75].	67
4.4 Shock tube and RCM ignition delay times from Sarathy et al. [75] at 40 atm compared with model predictions by the model from Sarathy et al. [75].	67
4.5 Experimental reactive (red), simulated reactive (blue), and experimental non-reactive (gray) pressure profiles at 40 atm for lean <i>i</i> -pentanol/air mixtures.	67
4.6 Experimental reactive (red), simulated reactive (blue), and experimental non-reactive (gray) pressure profiles at 40 atm for stoichiometric <i>i</i> -pentanol/air mixtures.	67
4.7 Experimental reactive (red), simulated reactive (blue), and experimental non-reactive (gray) pressure profiles at 40 atm for rich <i>i</i> -pentanol/air mixtures.	67
4.8 Sensitivity of the ignition delay to changes in the reaction rate coefficients for three equivalence ratios. Initial conditions for constant-volume adiabatic simulations are 800 K and 20 atm.	71

4.9	Sensitivity of the ignition delay to changes in the reaction rate coefficients for three equivalence ratios. Initial conditions for constant-volume adiabatic simulations are 689 K and 40 atm.	71
4.10	Reaction path analysis for <i>i</i> -pentanol at 800 K, 20 atm, and three equivalence ratios, based on constant-volume adiabatic simulations. Plain text: $\phi = 0.5$. Bold text: $\phi = 1.0$. Italic text: $\phi = 2.0$. The flux is integrated up to 20% fuel consumption.	72
5.1	Skeletal structure of methylcyclohexane	74
5.2	Experimentally measured ignition delays at $P_C = 50$ bar for the mixture conditions in Table 5.1	77
5.3	Comparison of experimental and simulated ignition delays for three pressures for Mix #1. The data at 15.1 and 25.5 bar are from the study of Mittal and Sung [89].	79
5.4	Comparison of experimental and simulated ignition delays for three pressures for Mix #2. The data at 15.1 and 25.5 bar are from the study of Mittal and Sung [89].	79
5.5	Comparison of experimental and simulated ignition delays for three pressures for Mix #3. The data at 15.1 and 25.5 bar are from the study of Mittal and Sung [89].	79
5.6	Comparison of selected simulated and experimental pressure traces at $P_C = 50$ bar. Red lines indicate that the pressure profile of the reactive simulation deviates from the non-reactive case prior to EOC. Solid lines: experiment; dashed lines: reactive simulation; dot-dot-dashed lines: non-reactive simulation.	81
5.7	Comparison of the present model with the experiments from Vasu et al. [83] and Vanderover and Oehlschlaeger [84] near 50 atm and for stoichiometric mixtures in O_2/N_2 air.	82
5.8	Comparison of mechanism performance with the activation energy of ketohydroperoxide decomposition set at 41.6 kcal mol ⁻¹ (blue) and 39.0 kcal mol ⁻¹ (red). Experimental ignition delays are shown in green symbols.	82

5.9 Path analysis of MCH combustion. Initial conditions are 25.5 bar and Mix #1 ($\phi = 1.0$) and 700 K (plain text), 800 K (bold text), 900 K (italic text). Note that not all possible reaction pathways are shown for each species.	84
5.10 Sensitivity of the ignition delay to various reaction rates for Mix #1 ($\phi = 1.0$), 25.5 bar and three temperatures (700, 800, and 900 K). At 700 K, the sensitivity of the overall ignition delay is in red and the sensitivity of the first stage ignition delay is in blue. At 800 K, the sensitivity of the overall ignition delay is in grey and the sensitivity of the first stage ignition delay is in green. At 900 K, the sensitivity of the overall ignition delay is in black. Numbers in parentheses represent the ranking of the first stage sensitivity indices.	90
5.11 Species mentioned in Fig. 5.10 or Table 5.2 and not included in Fig. 5.9.	90

List of Tables

2.1	Mixtures studied in the uncertainty analysis.	31
2.2	Symbols in Eq. (2.22). Reproduced from the work of York et al. [116].	32
3.1	HHV of Ethanol, Butanol Isomers, and Gasoline	43
3.2	Experimental Conditions and Reactant Purities	46
4.1	HHV of Ethanol, <i>i</i> -Pentanol, and Gasoline	63
4.2	<i>i</i> -pentanol Experimental Conditions	64
5.1	Molar Proportions of Reactants in MCH Experiments	74
5.2	Reactions that eliminate the first inflection point for a nominal case with two-stage ignition.	89

Chapter 1

Introduction

1.1 Background

The world relies heavily on combustion to provide energy in useful forms for human consumption; combustion currently represents over 80% of the world energy production [1] and is predicted to decrease in importance only slightly by 2040 [2]. In particular, the transportation sector accounts for nearly 40% of the energy use in the United States and of that, more than 90% is supplied by combustion of fossil fuels [3]. Unfortunately, emissions from the combustion of traditional fossil fuels have been implicated in a host of deleterious effects on human health and the environment [4] and fluctuations in the price of traditional fuels can have a negative impact on the economy [5].

Despite its shortcomings, combustion is currently the only energy conversion mechanism that offers the immediate capability to generate the sheer amount of energy required to run the modern world. Since we cannot eliminate combustion as an important energy conversion method, we must instead ameliorate the shortcomings of a primarily combustion-based energy economy. A two-pronged approach has developed to achieve the necessary improvements. These prongs include: 1) development of new fuel sources and 2) development of new combustion technologies. First, using new sources of fuel for combustion-based energy conversion can reduce the economic impact

Add lit
review
for
sam-
pling
from
RCM
in gen-
eral

of swings in the price of current fuels, in addition to potentially reducing emissions. Second, using new combustion technologies can reduce harmful emissions while simultaneously increasing the efficiency of combustion processes, thereby reducing fuel consumption.

Many new sources of fuels have been investigated recently. The most promising of these in the long term are renewable biological sources, which are used to produce fuels known as biofuels. The advantage of biofuels over traditional fuels lies in their feedstocks. Whereas traditional fuel feedstocks generally require millions of years to be produced, biofuel feedstocks are replenished on an annual basis. Furthermore, biofuels offer the potential to offset carbon emissions created from their combustion by reusing the emitted carbon to grow the plants from which the fuels are produced.

However, the combustion properties of biofuels may be substantially different from the traditional fuels they are intended to replace. This makes it difficult to quickly switch the energy economy to biofuels and necessitates medium-term investigation of alternative sources for traditional fuels. These sources include shale oil and liquefied coal, which have different chemical compositions than traditional fuel sources and therefore fuels made from these alternative sources have different combustion properties. Collectively, all of these fuels created from non-traditional sources are known as alternative fuels.

In addition to new fuel sources, new engine technologies are rapidly being developed. These include engines capable of operating in favorable combustion regimes, such as so-called Low Temperature Combustion (LTC) engines and Homogeneous Charge Compression Ignition (HCCI) engines. These devices avoid regions in the temperature-equivalence ratio space where combustion generates a large amount of emissions and operate in regions where efficiency is maximized and emissions are reduced. Other devices, such as the well-known catalytic converter, operate on the exhaust after it leaves the cylinder to improve emissions characteristics.

Neither of these approaches is able to mitigate all of the negative impacts of combustion by itself. By switching to biofuels but retaining the same engines, the efficiency and emissions targets may not be met; by only developing new engines, our sources of fuel will continue to cause eco-

nomic distress, turmoil, and negative effects on the environment. It will take a concerted effort to bring these two pathways of innovation together.

Unfortunately, there are many roadblocks on the way to combining new fuels in new engines. For instance, one can imagine the design and testing process of new engines and fuels becoming circular: the “best” alternative fuel should be tested in the “best” engine, but the “best” engine depends on which is selected as the “best” alternative fuel. One way to cut this circle short is by employing computer-aided design and modeling of new engines with new fuels to design engines to be fuel-flexible. Accurate and predictive models of combustion processes can be used to computationally test the efficacy of new technologies and fuels before they undergo expensive real-world testing. The key to this process is the development of accurate and predictive combustion models.

Substantial work has been put forth recently to develop and validate predictive combustion models for several alternative fuels. These studies include calculation and measurement of reaction rate coefficients, measurement of global and local combustion properties, and development of model construction methodologies. Nevertheless, much of the work is still ongoing, and there is substantial room for extending the state-of-the-art knowledge, especially at high-pressure conditions relevant to combustion in engines.

A combustion model for the combustion of a given fuel in a given device must necessarily accurately model the complete interaction of the operating elements of the device. This includes sub-models for the chemical reactions that the fuel and oxidizer undergo as well as the interaction of the fuel/oxidizer mixture with the operation of the device. The first of these is known as a chemical kinetic model or reaction mechanism; the second typically includes such effects as turbulence interaction, heat transfer, liquid spray dynamics, fluid mechanics, etc., each of which are typically modeled independently.

Chemical kinetic models for the combustion of large molecules are typically built in a hierarchical fashion, as described by Westbrook and Dryer [6]. That is, the model for the combustion of heptane contains the model for the combustion of hexane added to the model of combustion for pentane, and so on down to the models for hydrogen and carbon monoxide combustion. There-

fore, it is important to thoroughly validate the models for smaller species while building models of higher hydrocarbons and other molecular types. Work has been ongoing to explore the chemistry of small molecules for decades. Notable recent kinetic mechanisms to emerge from this work include the GRI-Mech series of mechanisms (most recently, version 3.0 [7]), USC-Mech v2 [8], and the AramcoMech series of mechanisms, most recently version 1.3 [9].

In addition, validation of kinetic models for the combustion of larger fuels has proceeded in parallel with the small molecule chemistry. Given their projected importance to combustion, one focus of the larger molecule work has naturally been on biofuels. These biofuels typically include chemical species such as alcohols and esters – neat alcohols can be used as fuels, while esters are typically found as components of biodiesel fuels. A review by Kohse-Höinghaus et al. [10] covers much of the experimental data available until 2010. Since then an enormous amount of data has been produced for both alcohols and esters. Since the focus of this study is on alcohols, I will highlight alcohols in the following sections.

Model construction and validation has also been focused on alternative “traditional” fuels, that is, fuels that are chemically similar to traditional fuels but produced from alternative sources such as shale oil or coal liquefaction. Traditional fuels and alternative “traditional” fuels typically contain hundreds or thousands of chemical components. This makes building and using models containing every species present in the fuel intractable on current computer hardware. Therefore, a more useful approach to building models for these fuels is to define a surrogate fuel. Surrogate fuels are made of a limited number of chemical components to ensure that model building and use are tractable, but the components are chosen so that the surrogate fuel faithfully reproduces the physical and chemical properties of the real fuel.

Much progress has been made recently to construct surrogates for typical transportation fuels. For instance, work on diesel surrogate formulation has recently been reviewed by Pitz and Mueller [11], work on gas turbine fuel surrogates has been briefly summarized by Dooley et al. [12], and work on gasoline surrogates has been summarized in the work of Anand et al. [13] and Pitz et al. [14]. One typical component class in the surrogate formulations is a cycloalkane or alkyl-

cycloalkane (collectively known as naphthenes), due to this class' presence in nearly all transportation fuels [14–17]. One particular cycloalkane, methylcyclohexane (MCH), has been suggested in several surrogate formulations, including those by Bielefeld et al. [18] and Naik et al. [19]. Recent work on MCH combustion will also be highlighted in the following sections.

1.2 Recent Work on the Combustion of Alcohols

Among the alcohols being considered as biofuels, two criteria are typically used to judge the suitability of a species: 1) its ease of production and 2) its potential as a “drop-in” replacement for current fuels. Because of these criteria (among others), much research recently has focused on the isomers of butanol, the C₄ alcohols, and *i*-pentanol, a C₅ alcohol. This is because these fuels are easy to produce by a number of biological pathways [20] and offer similar properties as gasoline for use in typical automotive transportation applications [21, 22].

One of the most common biofuels currently in use is ethanol (C₂H₆O). Although ethanol is ubiquitous at gasoline pumps, it suffers from several disadvantages that suggest it needs to be replaced [23]. In particular, ethanol has a much lower energy density than gasoline, reducing volumetric fuel economy, and ethanol is typically produced from crops that would otherwise be used as food sources [24].

n-Butanol has recently been identified as one of a suite of so called “second generation” biofuels intended to supplement or replace the “first generation” biofuels currently in use, such as ethanol [25, 26]. The second generation biofuels will help alleviate some of the problems identified with the first generation biofuels, including concerns about feedstocks. In addition to the normal (*n*) isomer, there are three other isomers of butanol—*s*-, *i*-, and *t*-butanol. Biological production pathways have been identified for *n*-, *s*-, and *i*-butanol [26, 27], but *t*-butanol is a petroleum derived product. Nevertheless, *t*-butanol is currently used as an octane enhancer in gasoline.

In the last five years, research into the combustion characteristics of the isomers of butanol has exploded, so exemplary references are provided here except for the articles of particular interest to

this work. In addition to applied engine research [28–30], fundamental combustion measurements have been made using many different systems. These include laminar flame speeds [31], jet-stirred reactor chemistry [32], low-pressure flame structure [33, 34], atmospheric pressure flame structure [35], pyrolysis [36–38], flow reactors [39, 40], and ignition delays, which will be discussed in more detail shortly. Other researchers have measured or calculated the reaction rate constants of reactions of butanol with various radicals, including OH [41–49], HO₂ [50–52], and CH₃ [53, 54].

Several studies of ignition delay of the butanol isomers have been conducted in both shock tubes and RCMs, including work in shock tubes by Moss et al. [55], Black et al. [56], Noorani et al. [57], Zhang et al. [58], Stranic et al. [59], Yasunaga et al. [60], Heufer et al. [61], Vranckx et al. [62], and Zhu et al. [63] and work in RCMs by Weber et al. [64], Weber and Sung [65], Weber et al. [66], and Karwat et al. [67]. These studies have covered a wide range of temperature-pressure regimes, from 1–90 bar and 675–1800 K.

Among the shock tube ignition studies, Moss et al. [55] have done measurements for all four isomers of butanol at 1 and 4 bar and 1200–1800 K, over equivalence ratios of $\phi = 0.5, 1.0$, and 2.0 and fuel mole percents of $0.25, 0.5$, and 1.0% . Black et al. [56] investigated autoignition for *n*-butanol from 1100–1800 K and 1, 2.6, and 8 atm over $\phi = 0.5, 1.0$, and 2.0 and fuel mole percentages of $0.6, 0.75$, and 3.5% . Noorani et al. [57] investigated the ignition delays of the primary alcohols from C₁–C₄ at pressures of 2, 10, and 12 atm under dilute conditions for equivalence ratio $\phi = 0.5, 1.0$, and 2.0 , and temperatures from 1070–1760 K. Zhang et al. [58] measured ignition delays of *n*-butanol at pressures of 2 and 10 atm, temperatures in the range of 1200–1650 K, and for equivalence ratios of $0.5, 1.0$, and 2.0 . Stranic et al. [59] measured ignition delays of all four isomers of butanol over the pressure range 1.5–43 atm, temperature range 1050–1600 K, and equivalence ratios of 0.5 and 1.0 . These studies showed generally good agreement of the ignition delays for *n*-butanol, but Stranic et al. [59] found that their ignition delays for the other isomers of butanol were shorter than the ignition delays measured by Moss et al. [55]. Stranic et al. [59] were unable to determine the reason for the discrepancy.

Yasunaga et al. [60] measured ignition delays of *s*-, *t*-, and *i*-butanol a pressure of 3.5 atm and

temperatures between 1250–1800 K. In addition, Yasunaga et al. [60] measured reactant, intermediate, and product species during pyrolysis of all four butanol isomers by sample extraction from their shock tube and analysis by gas chromatography. Other researchers have measured species profiles during the pyrolysis of butanol isomers in a shock tube by optical techniques, including Cook et al. [68], Stranic et al. [69, 70], and Rosado-Reyes and Tsang [71, 72]. At Stanford University, researchers measured the time-histories of the fuel, OH, H₂O, C₂H₄, CO, and CH₄ were measured behind reflected shock waves for *n*-, *s*-, and *i*-butanol [68–70]. Rosado-Reyes and Tsang [71, 72] measured the thermal decomposition of *n*- and *s*-butanol in a single-pulse shock tube and derived rate expressions for the decomposition reactions.

Heufer et al. [61] reported high pressure ignition delay results of stoichiometric *n*-butanol/air mixtures under the conditions behind the reflected shock of approximately 10–42 bar and 770–1250 K. The results of Heufer et al. [61] showed an interesting non-Arrhenius behavior at temperatures lower than about 1000 K for the pressure range studied. They found that the rate of increase of ignition delay with decreasing temperature appears to change around 1000 K. Vranckx et al. [62] further developed the low-temperature oxidation mechanism of *n*-butanol by performing experiments between 61–92 bar and 795–1200 K and updating a kinetic model with a butyl-peroxy sub-mechanism. They showed improved agreement with predictions of low-temperature butanol ignition delays, but incorrectly predicted the existence of two-stage ignition phenomena.

Zhu et al. [63] measured the ignition delays of *n*-butanol in a shock tube using a newly developed technique known as constrained reaction volume (CRV). In traditional shock tube experiments, it is difficult to measure ignition delays longer than approximately 1–10 ms because fluid-dynamic effects and other phenomena invalidate the assumptions typically used to calculate the thermodynamic state. In the CRV strategy, the reactants are effectively limited to a small region in the shock tube ensuring that the conditions under which ignition occurs are constant enthalpy/nearly constant pressure and are well characterized for longer time scales than in traditional shock tube experiments. Zhu et al. [63] were thus able to measure ignition delays of *n*-butanol between temperatures of 716–1121 K, pressures of 20 and 40 atm, and equivalence ratios of $\phi = 0.5, 1.0$, and 2.0. Using

the CRV strategy and constant enthalpy/constant pressure modeling assumptions, Zhu et al. [63] demonstrated that one recent kinetic model was able to predict the ignition delay of *n*-butanol well for most of the conditions they studied.

Ignition delay experiments of the butanol isomers have also been performed in rapid compression machines (RCMs). Weber et al. [64] studied the ignition delays of *n*-butanol for low- to intermediate-temperature conditions between 675–925 K, pressures of 15 and 30 bar, and equivalence ratios of $\phi = 0.5, 1.0$, and 2.0. Weber et al. [64] found no evidence of two-stage ignition or non-Arrhenius behavior in their results. Weber et al. [64] also found that models available until the time of their work (2011) were unable to predict the ignition delays of *n*-butanol, over-predicting the ignition delay by approximately one order of magnitude. Subsequently, Weber and Sung [65] extended their study to the other isomers of butanol, covering temperatures between 715–910 K, pressures of 15 and 30 bar, and the stoichiometric equivalence ratio. Results from the study by Weber and Sung [65] are presented in Chapter 3. In summary, Weber and Sung [65] found that the order of reactivity—in terms of the inverse of ignition delay—of the butanol isomers changes when the pressure is changed from 15 to 30 bar. Moreover, Weber and Sung [65] found unique pre-ignition heat release behavior during the ignition of *t*-butanol that was not present during the ignition of the other isomers.

Weber et al. [66] studied the autoignition of *i*-butanol at three mixture conditions, including $\phi = 0.5$ with air as the oxidizer and $\phi = 0.5$ and 2.0 where the O₂:N₂ ratio in the oxidizer was changed while the fuel mole fraction was held constant to change the equivalence ratio. Weber et al. [66] found that a newly developed kinetic model for *i*-butanol combustion was able to predict the stoichiometric (from the work of Weber and Sung [65]) and lean ignition delays in air, but was unable to capture the dependence of the ignition delays on the initial oxygen concentration. In addition, Zhu et al. [63] and Weber et al. [64] noted similar inability to predict the dependence of ignition delay on initial oxygen concentration for *n*-butanol for several different kinetic mechanisms.

Karwat et al. [67] studied the ignition delays of *n*-butanol for stoichiometric mixtures over temperatures from 920–1040 K and pressures near 3 atm. Karwat et al. [67] found good agreement of

the ignition delays with the kinetic model developed in the study of Black et al. [56]. In addition, Karwat et al. [67] used a high-speed sampling valve to remove gas samples from the reaction chamber during the induction period of *n*-butanol ignition. They quantified mole fractions of CH₄, CO, C₂H₄, C₃H₆, C₂H₄O, C₄H₈O, 1-C₄H₈, and *n*-butanol at several times during the ignition. Comparison of the time histories of these species with predictions from the model by Black et al. [56] showed that, although the model is able to predict the ignition delay well, it is not able to reproduce the time history of species concentrations very well, particularly C₂H₄. This result demonstrates the importance of rigorously validating a kinetic model over a wide range of conditions and for a wide range of validation targets.

In comparison to the butanol isomers, *i*-pentanol has received significantly less focus in the literature. Studies of the combustion of *i*-pentanol have been conducted in JSRs [73–75], low-pressure flow reactors [76], counterflow flame experiments [75], shock tubes [75, 77, 78], and RCMs [75, 77]. Other studies have investigated the efficacy of using *i*-pentanol in an HCCI engine [79–81]. Finally, studies described in this work have been conducted to determine the ignition properties of *i*-pentanol (see Chapter 4). Both the works by Sarathy et al. [75] and Tsujimura et al. [77] developed detailed kinetic models for the combustion of *i*-pentanol whose validation was based, in part, on ignition delay experiments. Using shock tubes and RCMs in concert, these studies were able to provide ignition delays for temperatures, pressures, and equivalence ratios of 650–1450 K, 7–60 bar, and $\phi = 0.5, 1.0$, and 2.0, respectively. These studies generally found good agreement of their models with their validation data sets, although Sarathy et al. [75] found that their model had difficulty predicting rich ignition delays. In addition, substantial pre-ignition heat release was observed for all of the equivalence ratios at 40 bar in the RCM measurements, similar to *t*-butanol.

1.3 Recent Work on Ignition of Methylcyclohexane

Several studies have suggested the use of methylcyclohexane (MCH) as a component in surrogate formulations [18, 19], as discussed previously. Furthermore, MCH is the simplest branched

or substituted cycloalkane, and can therefore provide a base from which to build models of the combustion of other, larger, naphthenes.

Substantial experimental and modeling work has been conducted for naphthenes in general, and MCH in particular. Pitz and Mueller [11] has conducted an extensive review of the work on naphthenes, so only studies involving homogeneous ignition of MCH are discussed here. Ignition delays of MCH have been measured in shock tubes [82–87] and RCMs [14, 88, 89] by a number of researchers. These studies collectively cover the temperature-pressure space in the range of 700–2100 K and 1–70 atm. To complement this experimental work, a number of kinetic models for MCH combustion have been constructed, notably by Pitz et al. [14] and Orme et al. [86].

The study of Rotavera and Petersen [82] measured ignition delays of MCH behind reflected shock waves near 1 and 10 atm for equivalence ratios of $\phi = 0.5, 1.0$, and 2.0 . They compared their measured ignition delays with predictions from the model of Pitz et al. [14] and found generally good agreement. Hong et al. [87] measured ignition delays for conditions of temperature between 1280–1480 K, pressures of 1.5 and 3 atm, and equivalence ratios of $\phi = 1.0$ and 0.5 . Hong et al. [87] compared their measurements with three mechanisms from the literature, including those by Pitz et al. [14] and Orme et al. [86] and found relatively good agreement for their conditions.

However, other studies have found that the existing models are not able to predict ignition delays at conditions for which they were not validated—that is, the models are not truly predictive. For instance, previous work conducted in an RCM by Mittal and Sung [89] measured the ignition delays of MCH/O₂/N₂/Ar mixtures at pressures of 15.1 and 25.5 bar, for three equivalence ratios of $\phi = 0.5, 1.0$, and 1.5 , and over the temperature range of 680–840 K. They compared their measured ignition delays to simulated ignition delays computed using the mechanism of Pitz et al. [14] and found that the model over-predicted both the first stage and overall ignition delay substantially [89]. Moreover, studies conducted in shock tubes by Vasu et al. [83] and Vanderover and Oehlschlaeger [84] came to similar conclusions in their studies, which collectively considered conditions between 795–1560 K and 1–70 atm. Further studies conducted in this work have expanded the validation range of MCH ignition data and substantially improved the predictive ability of kinetic models of

MCH combustion (see Chapter 5).

1.4 Summary

Due to its relevance in predicting the performance of a fuel in existing and advanced engines, ignition delay is a very common measure of the global performance of a kinetic mechanism. Ignition delays for homogeneous systems are typically measured in shock tubes or RCMs, where the effects of fluid motion and turbulence are generally minimized. However, as demonstrated for the case of butanol isomers, *i*-pentanol, and methylcyclohexane, the validation target of ignition delays is necessary but not sufficient to develop truly predictive models.

Work has begun to utilize homogeneous ignition experimental platforms to measure characteristics other than ignition delays—see, for instance, the work by Karwat et al. [67] to measure species profiles in their RCF using gas sampling; the work by Das et al. [90] and Uddi et al. [91] to directly measure the temperature in the reaction chamber of an RCM using mid-IR laser light absorption; and the work by Stranic et al. [70] to perform simultaneous concentration measurements of multiple species in their shock tube.

Moreover, fuels often exhibit substantially different ignition behavior at engine-relevant, high-pressure, low- to intermediate-temperature conditions. Therefore it is critically important to generate validation datasets at these conditions.

Thus, the objectives of this work can be stated succinctly as follows:

1. Generate ignition delay datasets for alternative fuels at high-pressure, low-temperature conditions that have not been studied extensively in previous work
2. Develop and characterize a new experimental apparatus to enable ex situ species measurements from the reaction chamber of the rapid compression machine during the ignition delay
3. Use the data acquired from Item 1 and Item 2 to extend the validation of new and existing chemical kinetic models for the combustion of alternative fuels

4. Analyze new and existing chemical kinetic models to help understand the cause of discrepancies and clarify the important reaction pathways in high-pressure alternative fuel ignition

1.5 Organization of this Work

The remainder of this work is structured as follows. Chapter 2 describes the experimental facilities used in this work, including the rapid compression machine and the newly-developed fast sampling system. Detailed uncertainty analyses are considered for the appropriate apparatuses. The subsequent sections are organized by the fuel studied: Chapter 3 considers the butanol isomers, Chapter 4 considers *i*-pentanol, and Chapter 5 considers methylcyclohexane. Finally, Chapter 6 presents conclusions based on this work and recommendations for future directions.

Chapter 2

Experimental Facilities

2.1 Rapid Compression Machine

2.1.1 Experimental Procedure

The studies in this dissertation were conducted using the Rapid Compression Machine (RCM) constructed by Mittal around 2005 and described in the work of Mittal and Sung [92] and Mittal [93]. This RCM has been used to study the autoignition behavior of a number of fuels, including *n*-decane, methylcyclohexane, hydrogen, syngas, dimethyl ether, methanol, toluene, benzene, di-isobutylene, iso-octane, jet fuel, and gasoline [12, 89, 90, 94–106], in addition to the studies presented in this work.

A modern RCM operates by rapidly compressing (hence the name) a test gas mixture to targeted pressure and temperature conditions. The compression is effected by either a single piston or dual, opposed pistons. Upon reaching the targeted state, the piston (or pistons) is stopped and fixed in place so that the reactions proceed in a constant volume reactor. When studying autoignition with an RCM, the primary data are the measured pressure traces during and after the compression stroke. These pressure traces are processed to derive information such as the pressure and temperature at the end of compression (EOC) and the ignition delay. It is also possible to employ laser diagnostics

or extract gas samples from the reactor to examine reaction pathways in more detail.

The present RCM is a pneumatically-driven/hydraulically-stopped single-piston arrangement. A schematic of the RCM is shown in Fig. 2.1 and an image is shown in Fig. 2.2. The RCM consists of four chambers and three pistons that are used to control the machine. The chambers are called the reaction chamber, the hydraulic chamber, the pneumatic chamber, and the driving tank; similarly, the pistons are called the reactor, hydraulic, and pneumatic pistons and are each installed in the chamber of the same name. The rear of the reaction chamber is bolted to the front of the hydraulic chamber; seals in the face of the hydraulic chamber prevent oil from leaking into and contaminating the reaction chamber. The driving tank and the rear of the pneumatic chamber are connected by a union; a seal around the circumference of the pneumatic piston seals gas in the driving tank from the front of the pneumatic chamber. Thus, the pneumatic piston can be driven by pressure from the driving tank on its rear and pressure from the pneumatic chamber on its front. The three pistons are connected by a rod running from the front of the pneumatic piston to the rear of the reactor piston so that they move as one; this will be referred to as the piston assembly.

At the start of an experimental run, with the piston in the EOC position, the reaction chamber is vacuumed to less than 1 Torr. Next, the piston assembly is retracted by pressurizing the front face of the piston in the pneumatic chamber. For safety, and to prevent damage to the RCM, the driving tank should be filled to limit the acceleration of the piston assembly during the retraction. The pressure on the front of the pneumatic piston pulls the piston assembly rearward and seats the rear of the hydraulic piston onto an O-ring in the rear of the hydraulic chamber. The hydraulic chamber is filled with oil to a pressure of approximately 800 psi, providing a rearward force on the front face of the hydraulic piston. Then, the air pressure is released from the front of the pneumatic chamber and the driving tank is filled to the desired driving pressure. The force on the hydraulic piston opposes the force on the pneumatic piston from the driving tank and the piston assembly remains at rest. Then, the reaction chamber is filled with the required initial pressure of test gas mixture from the mixing tank. Finally, compression is triggered by releasing the hydraulic pressure through an electrically-operated solenoid valve. The piston assembly is driven forward by the unbalanced

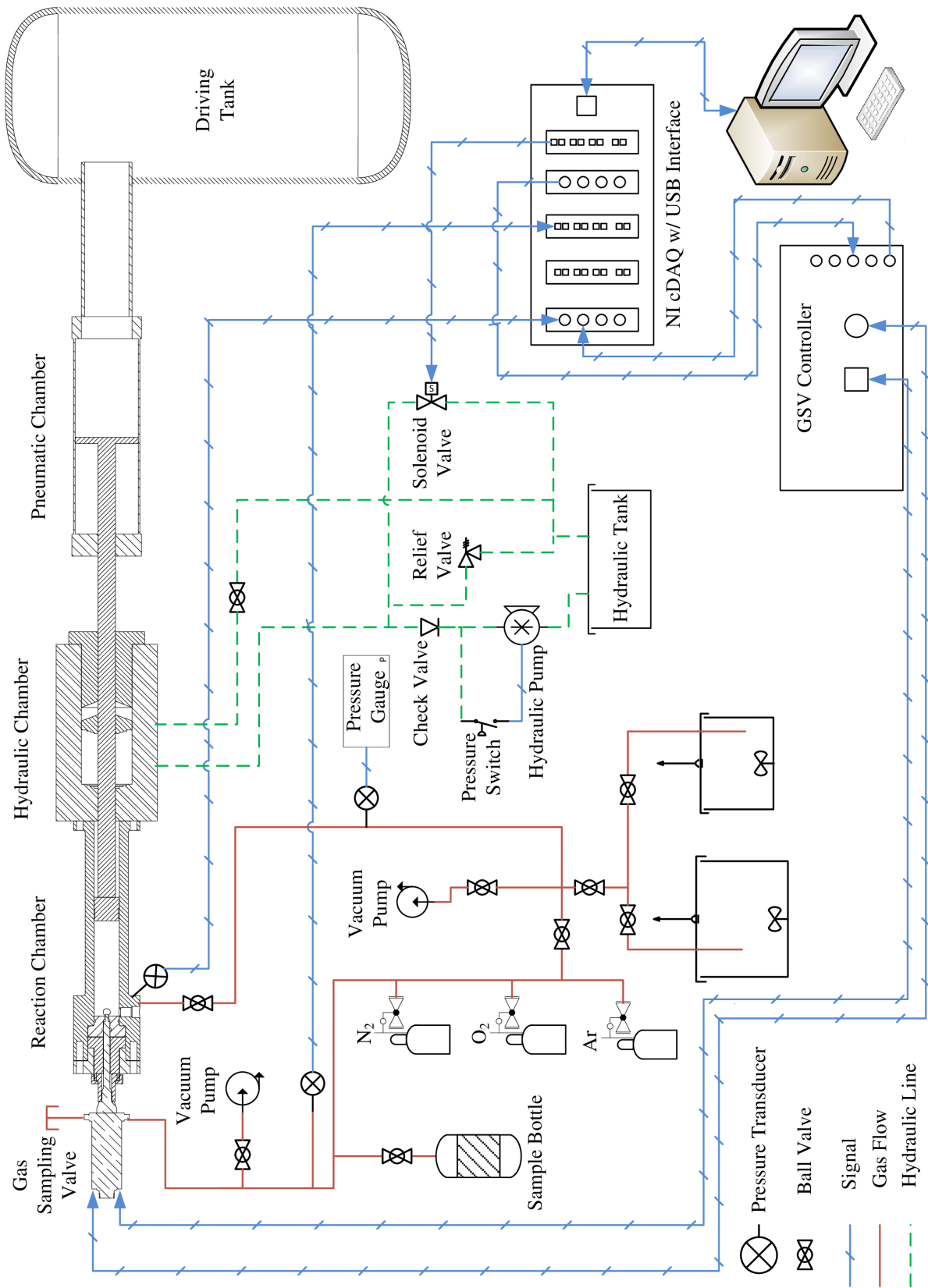


Figure 2.1: Schematic of the RCM. Not to scale

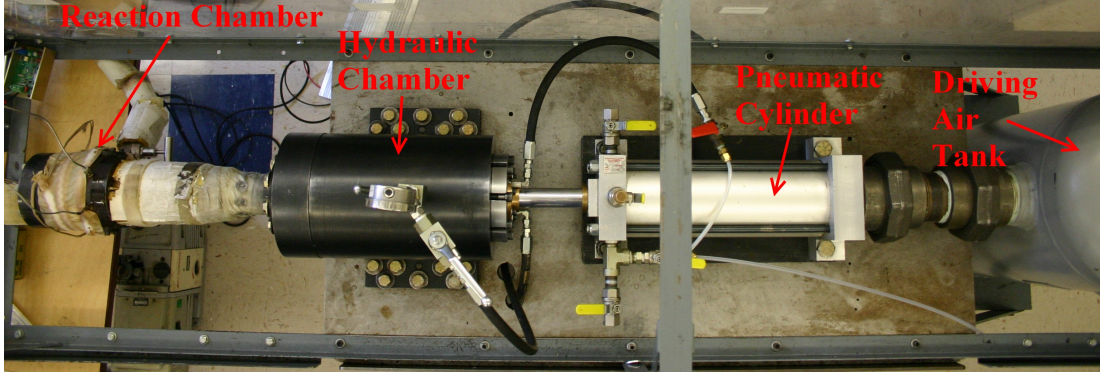


Figure 2.2: Photograph of the RCM.

force from the pressure in the driving tank on the pneumatic piston. The gases in the reaction chamber are brought to the compressed pressure (P_C) and compressed temperature (T_C) conditions in approximately 30–50 ms.

The required driving pressure for a given EOC pressure can be estimated from a force balance between the force on the pneumatic piston from the driving tank and the force on the reactor piston from the test gases, as shown in Eq. (2.1c).

$$P_{d,\min} \cdot A_p = P_{r,EOC} \cdot A_r \quad (2.1a)$$

$$P_{d,\min} \cdot \frac{\pi d_p^2}{4} = P_{r,EOC} \cdot \frac{\pi d_r^2}{4} \quad (2.1b)$$

$$P_{d,\min} = P_{r,EOC} \cdot \frac{d_r^2}{d_p^2} \quad (2.1c)$$

In Eq. (2.1), $P_{d,\min}$ is the minimum driving pressure, A_p is the cross-sectional area of the pneumatic piston, $P_{r,EOC}$ is the pressure in the reactor at the EOC (i.e. P_C), A_r is the cross-sectional area of the reactor piston, d_p is the diameter of the pneumatic piston, and d_r is the diameter of the reactor piston.

The minimum driving pressure is such that the piston does not rebound at the EOC due to pressure on the reactor piston. So that the driving pressure can be much lower than the EOC pressure, the diameter ratio of the reactor piston to the driver piston is 2/5, allowing a factor of 6.25 lower driving pressure than EOC pressure. The actual driving pressure should exceed the minimum by

some safety margin so that the reactor remains at constant volume even if there is some pressure rise due to heat release in the reaction chamber prior to the main ignition.

There is not a theoretical upper limit on the driving pressure. It is desired that the piston should reach the EOC conditions in as short a time as possible to minimize heat loss from the reactants to the reactor walls and minimize the time for reactions to occur during the compression stroke. This implies that the driving pressure should be made as high as possible so that the highest piston velocity is achieved. However, higher piston velocities require a higher deceleration at the EOC. In the present RCM, the deceleration is provided by venting the hydraulic oil between steps on the hydraulic piston and matched steps on the front of the hydraulic chamber. If the piston is overdriven—that is, the driving pressure is too high—the piston will not be sufficiently decelerated by the oil venting and will impact the front of the hydraulic chamber at high velocity. This can damage the RCM and cause the piston to rebound elastically. It also generates substantial noise in the pressure trace and should be avoided.

Typical driving gas pressures are between 50 psi for $P_C = 15$ bar experiments to 125 psi for $P_C = 50$ bar experiments. These driving pressures represent a good compromise between the minimum required for no rebound at EOC due to pressure and no rebound at EOC due to elastic reaction. Nonetheless, a small amount of piston rebound can be expected during/after the main ignition event. This small rebound may have an effect on the computation of ignition delay if it reduces the pressure rise rate during the ignition; it is expected that this effect will be very small relative to the typical random uncertainty in ignition delay experiments. Moreover, the driving pressures required to balance the full pressure rise during to ignition are more likely cause elastic rebound, especially for high P_C when the post-ignition pressure rise is greater.

The EOC conditions (P_C and T_C) can be independently varied. This is made possible by independent variation of the compression ratio, initial pressure and initial temperature, and the specific heat ratio of the test gases. The compression ratio can be increased by adding spacers onto the rear of the hydraulic chamber, increasing the stroke, and can be reduced by adding split shims onto the rear of the reaction chamber, increasing the EOC clearance length. Adjustment of the specific

heat ratio of the gas can be accomplished by substituting components (i.e. substituting Ar for N₂ results in higher P_C and T_C if all other conditions are fixed). The initial temperature is controlled by heaters, as described in the following section.

2.1.2 Test Gas Mixture Preparation

Fuel/oxidizer pre-mixtures are prepared in two mixing tanks, one approximately 17 L and the other approximately 15 L in volume. These large volumes allow many runs to be conducted from one mixture preparation. The mixing tanks are connected to the reaction chamber by flexible stainless steel manifold tubing. The tanks, reaction chamber, and connecting manifold are wrapped in heating tape and insulation to control the initial temperature of the mixture. Temperature controllers from Omega Engineering use thermocouples placed on the lid of each mixing tank, approximately in the center of each mixing tank, embedded in the wall of the reaction chamber, and near the inlet valve of the reaction chamber to control the preheat temperature of the mixture. A static pressure transducer measures the pressure in the manifold and mixing tanks. This transducer is used during mixture preparation and to measure the initial pressure of a given experiment. Two transducers are for various experiments in this work, as described below in Sec. 2.1.8.2.

Most of the fuels studied in this work are liquids at room temperature and pressure and have relatively low vapor pressure. A similar procedure, outlined below, was used for all of the butanol isomers, *iso*-pentanol, and methylcyclohexane; specific procedures are given in the chapter relevant to each fuel. First, the mixing tanks are vacuumed to an ultimate pressure less than 5 Torr. The liquid fuel is massed in a syringe to a precision of 0.01 g prior to injection through a septum. Proportions of O₂, N₂, and Ar are added manometrically at room temperature. The preheat temperature of the RCM is set above the saturation point for each fuel to ensure complete vaporization. The vapor pressure as a function of temperature is calculated according to fits taken from Yaws [107]. A magnetic stirrer mixes the reactants. The temperature inside the mixing tank is allowed to equilibrate for approximately 1.5 h.

This approach to mixture preparation has been validated in several previous studies by with-

drawing gas samples from the mixing tank and analyzing the contents by GC/MS [64], GC-FID [94], and GC-TCD [90]. These studies have verified the concentration of *n*-butanol, *n*-decane, and water, respectively. In addition, both the work by Kumar et al. [94] on *n*-decane and the study of Weber et al. [64] on *n*-butanol confirmed that there was no fuel decomposition over the course of a typical set of experiments. Furthermore, within this study, each new mixture preparation is checked against previously tested conditions to ensure reproducibility.

2.1.3 Definition of Ignition Delay

The pressure in the reaction chamber during an experiment is monitored by a Kistler 6125B piezo-electric dynamic pressure transducer. The charge signal from the transducer is amplified and converted to a voltage by a Kistler 5010B charge amplifier. The voltage is sent to a National Instruments cDAQ equipped with the NI-9215 module. The signal is recorded by a LabView VirtualInstrument at 50 kHz.

Figure 2.3 shows a representative pressure trace from these experiments with methylcyclohexane (MCH) at $P_C = 50$ bar, $T_C = 761$ K, and $\phi = 1.5$ (See Chapter 5). Note that Fig. 2.3 shows a case with two stages of ignition; not all of the fuels studied had conditions that showed two-stage ignition. Nonetheless, the ignition delay is consistently defined in all the work in this study. The definitions of the EOC and the ignition delays are indicated on the figure. The end of compression time is defined as the time when the pressure reaches its maximum before first stage ignition occurs, or for cases where there is no first stage ignition, the maximum pressure before the overall ignition occurs. The first stage ignition delay is the time from the end of compression until the first peak in the time derivative of the pressure. The overall ignition delay is the time from the end of compression until the largest peak in the time derivative of the pressure.

Each unique P_C and T_C condition is repeated at least 5 times to ensure repeatability of the experiments. The experiment closest to the mean of the runs at a particular condition is chosen for analysis and presentation. The standard deviation of all of the runs at a condition is less than 10% of the mean in all cases.

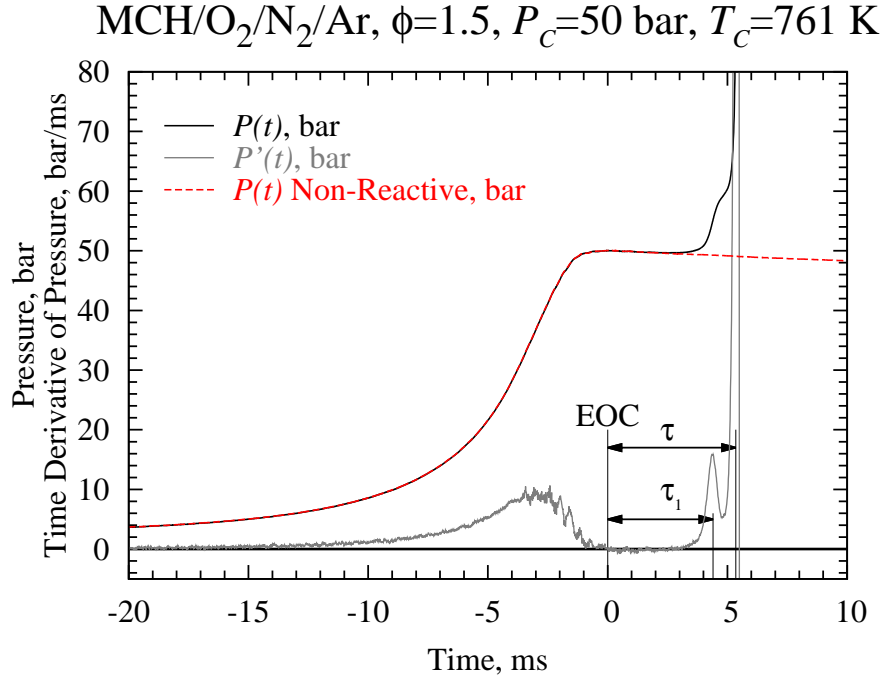


Figure 2.3: Representative pressure trace indicating the definition of the first stage and overall ignition delays and the corresponding non-reactive pressure trace. EOC stands for End of Compression.

2.1.4 Non-Reactive Experiments

Figure 2.3 also shows a non-reactive pressure trace. Due to heat loss from the test mixture to the cold reactor walls, the pressure and temperature of the gas in the reaction chamber will decrease after the end of compression. A non-reactive pressure trace is measured that corresponds to each unique P_c and T_c condition studied to quantify the effect of the heat loss on the ignition process and to verify that no heat release has occurred during the compression stroke. The non-reactive pressure trace is acquired by replacing the oxygen in the oxidizer with nitrogen, so that the specific heat ratio of the initial mixture is maintained, but the heat release due to exothermic oxidation reactions is eliminated. Maintaining a similar specific heat ratio ensures that the non-reactive experiment faithfully reproduces the conditions of the reactive experiment. A representative non-reactive pressure trace is shown in Fig. 2.3 corresponding to the experimental conditions in the figure.

2.1.5 Reaction Chamber Homogeneity

An RCM to be used for studies of homogeneous chemistry—as in this study—must ensure that homogeneous conditions exist inside the reaction chamber for the duration of the experiment. Due to the high piston velocities required to minimize heat loss and reaction during the compression stroke, complex fluid mechanical effects can strongly affect the state of the reactants at the EOC. The most important of these effects is caused by the motion of the piston itself, where the piston pushes the wall boundary layer into a roll-up vortex [108]. This cold vortex mixes with the hotter gases near the center of the reaction chamber and causes large spatial inhomogeneities of temperature and species.

To facilitate spatially homogeneous conditions in the reactor and reduce the effect of the roll-up vortex, it is necessary to trap the boundary layer. This is accomplished on the present RCM by a crevice machined into the crown of the piston, shown in cross-section in Fig. 2.4. The boundary layer enters the crevice through the converging section as the piston moves forward and is trapped within the crevice. The dimensions of the crevice were optimized by Mittal [93] through CFD simulations for high-pressure conditions. Subsequently, Mittal and Sung [109] experimentally showed that the optimized crevice design provides homogeneous conditions in the reaction chamber up to approximately 150 ms after the EOC. By using PLIF measurements of acetone-seeded mixtures, Mittal and Sung [109] showed that there was a core region of gases near the center of the reactor whose temperature remained spatially homogeneous.

2.1.6 Determination of Reactant Temperature

Two independent thermodynamic properties are required to fix the thermodynamic state of the reactants in the reaction chamber at a given time. The first property is the pressure, measured by the dynamic pressure transducer, as discussed previously; the second property is chosen to be the temperature.

In general, it is rather difficult to directly measure the temperature of the gases in the reaction

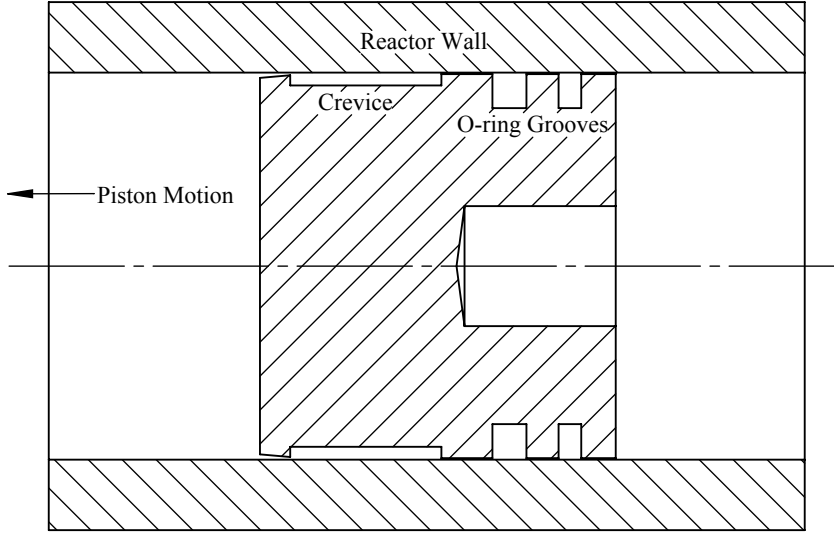


Figure 2.4: Creviced piston installed in the present RCM.

chamber during and after compression. Intrusive methods such as thermocouples may introduce inhomogeneities into the reaction chamber and non-intrusive optical techniques are difficult to set up and require extensive calibration at the pressures of interest in RCM studies. Thus, the temperature is determined indirectly by applying an assumption called the “adiabatic core hypothesis” to the reaction chamber [92, 108].

If all of the gases in the reaction chamber were compressed isentropically, the temperature at the end of compression could be found by the following relations:

$$\ln(\text{CR}) = \int_{T_0}^{T_{ic}} \frac{1}{T(\gamma - 1)} dT \quad (2.2a)$$

$$\ln\left(\frac{P_{ic}}{P_0}\right) = \int_{T_0}^{T_{ic}} \frac{\gamma}{T(\gamma - 1)} dT \quad (2.2b)$$

where CR is the volumetric compression ratio, T_0 is the initial temperature, T_{ic} is the temperature at the end of isentropic compression, γ is the temperature-dependent ratio of specific heats, P_{ic} is the pressure at the end of isentropic compression, and P_0 is the initial pressure.

However, experiments show that the measured pressure in the reaction chamber does not reach the value of P_{ic} calculated by using the geometric compression ratio. The difference is due to finite heat loss from the reactants to the reactor walls and the crevice volume during the compression. Under the adiabatic core hypothesis, it is assumed that the heat loss from the reactants only occurs in a thin boundary layer near the wall, and the central core region is unaffected by heat loss (i.e. the core is adiabatic) [110]. Thus, the heat loss is modeled as an effective reduction in the compression ratio, and the temperature during the compression stroke can be calculated by:

$$\ln\left(\frac{P_C}{P_0}\right) = \int_{T_0}^{T_C} \frac{\gamma}{T(\gamma - 1)} dT \quad (2.3)$$

where P_C is the measured pressure at the end of compression, T_C is the temperature at the end of compression, and the other variables are the same as in Eq. (2.2).

After the end of compression, the pressure in the reaction chamber decreases, as can be seen in Fig. 2.3. This pressure decrease is caused by heat loss from the reactants in the constant volume reaction chamber and is accompanied by a decrease in the temperature of the reactants. To model the thermodynamic state after the end of compression, the adiabatic core hypothesis is applied, and the heat loss is assumed to occur only in a thin boundary layer near the reactor walls. Thus, the core region is modeled as adiabatic, and the heat loss from the boundary layer is modeled as an isentropic volume expansion.

2.1.7 Determination of Compressed Temperature

In general, the specific heat ratio used in Eqs. (2.2) and (2.3) is an unknown function of temperature and composition, so Eq. (2.3) cannot be integrated directly to find T_C . If the specific heats are parameterized with a linear fit and the composition is assumed to be fixed, it is possible to integrate Eq. (2.3) directly, but this process is quite tedious; nonetheless, it will be applied in Sec. 2.1.8 to determine the uncertainty of T_C . In general, the simplest method of calculating T_C is to use software to numerically integrate Eq. (2.3).

In this work, the CHEMKIN-Pro [111] software is used to perform the numerical integration and calculation of T_C . The CHEMKIN-Pro software provides the facility for a user-specified volume as a function of time to be applied to a homogeneous, adiabatic reactor. Since the adiabatic core of the reaction chamber is modeled as undergoing an isentropic volumetric compression followed by an isentropic volumetric expansion, the user-specified volume functionality is used to compute the RCM reactor state as a function of time. A volume trace for simulation is computed from the measured pressure trace using the isentropic relation:

$$\frac{V_2}{V_1} = \left[\frac{P_1}{P_2} \right]^{\frac{1}{\gamma}} \quad (2.4)$$

where V_1 and V_2 are the volumes at consecutive time points, P_1 and P_2 are the pressures at consecutive time points, and γ is the temperature dependent specific heat. This equation is applied during and after the compression stroke to calculate the volume trace. To achieve the best representation of the experiment, the reactive pressure trace is used until EOC; after EOC, the corresponding non-reactive pressure trace is used. In Eq. (2.4) it is assumed that changes in composition of the reactants are negligible during the compression stroke. The initial volume is arbitrarily taken to be equal to 1.

For use in Eq. (2.4), γ is tabulated for each time point. Thus, the temperature at each time point must also be computed by using the isentropic relation for temperature:

$$\frac{T_2}{T_1} = \left[\frac{P_2}{P_1} \right]^{\frac{\gamma-1}{\gamma}} \quad (2.5)$$

where T_2 and T_1 are the temperatures at consecutive time points. Since T_2 depends on the value of γ , which in turn depends on T_2 , Eq. (2.5) is iterated until the temperature changes by less than one tenth of one percent on consecutive iterations. Once again, it is assumed that changes in composition have a negligible influence on the ratio of specific heats. The temperature calculated by Eq. (2.5) is typically within 1K of the temperature calculated by CHEMKIN-Pro.

2.1.8 Uncertainty of Ignition Delay and Compressed Temperature

The uncertainty of the compressed temperature is an important parameter to report. Since T_C is not measured, we must perform an uncertainty propagation analysis on the equation used to calculate T_C , Eq. (2.3). First, we simplify the term involving γ in Eq. (2.3). By definition, γ is the ratio of the specific heat at constant pressure to that at constant volume

$$\gamma \equiv \frac{C_p}{C_v} = \frac{C_p/R}{C_v/R} \quad (2.6)$$

where C_p and C_v are the specific heats in molar units at constant pressure and volume, respectively, and R is the universal gas constant, used to produce non-dimensional specific heats. Letting a hat denote the non-dimensional specific heats, the difference between the non-dimensional specific heats is one, $\hat{C}_v = \hat{C}_p - 1$. Then, it follows that

$$\frac{\gamma}{\gamma - 1} = \frac{\frac{\hat{C}_p}{\hat{C}_v}}{\frac{\hat{C}_p}{\hat{C}_v} - 1} = \frac{\frac{\hat{C}_p}{\hat{C}_p - 1}}{\frac{\hat{C}_p}{\hat{C}_p - 1} - 1} = \frac{\frac{\hat{C}_p}{\hat{C}_p - 1}}{\frac{1}{\hat{C}_p - 1}} = \hat{C}_p \quad (2.7)$$

In Eq. (2.3), the total specific heat ratio for the mixture should be used; thus, the simplification as shown in Eq. (2.7) requires that the specific heat \hat{C}_p also be the total specific heat. In the following, we assume that there is negligible change of the total specific heat due to changes in reactant mole fractions, as for Eqs. (??) and (??). The total specific heat is simply the sum of the product of the species mole fractions and their specific heats

$$C_{p,\text{total}} = \sum_i X_i C_{p,i} \quad (2.8a)$$

$$\hat{C}_{p,\text{total}} = \frac{\sum_i X_i C_{p,i}}{R} \quad (2.8b)$$

where i indicates the species and X_i is the species mole fraction. In the NASA polynomial formulation used by CHEMKIN, the non-dimensional specific heat at constant pressure as a function of temperature is represented by a fourth-order polynomial fit

$$\hat{C}_{p,i} = c_{1,i} + c_{2,i}T + c_{3,i}T^2 + c_{4,i}T^3 + c_{5,i}T^4 \quad (2.9)$$

In general, this means that the specific heat can be non-linear. However, since the mixtures prepared in this study are composed primarily of O₂, N₂ and Ar (i.e. no more than 7% of any mixture is the fuel), and since the specific heats of O₂, N₂ and Ar are only weakly temperature dependent over the range of temperatures experienced during compression, we will approximate the total specific heat as a linear function of temperature.

$$\begin{aligned} \hat{C}_{p,\text{total}} &= \sum_i X_i \hat{C}_{p,i} \\ &= \sum_i X_i \left(\sum_{j=1}^5 c_{j,i} T^{j-1} \right) \\ &\approx a + bT \end{aligned} \quad (2.10)$$

a and b are found by fitting the total non-dimensional specific heat over the temperature range from 300–1100 K, as discussed below in Sec. 2.1.8.4.

With this approximation of the specific heat, we can integrate Eq. (2.3) to find the compressed temperature

$$\ln \frac{P_C}{P_0} = \int_{T_0}^{T_C} \frac{\gamma}{T(\gamma - 1)} dT = \int_{T_0}^{T_C} \frac{\hat{C}_p}{T} dT \quad (2.11a)$$

$$= \int_{T_0}^{T_C} \frac{a + bT}{T} dT \quad (2.11b)$$

$$= \left[a \ln T + bT \right]_{T_0}^{T_C} \quad (2.11c)$$

$$\ln \frac{P_C}{P_0} = a \ln T_C + bT_C - (a \ln T_0 + bT_0) \quad (2.11d)$$

Solving Eq. (2.11d) for T_C

$$T_C = \frac{aW\left(\frac{b}{a} \exp\left[\frac{bT_0}{a}\right] T_0 \left[\frac{P_C}{P_0}\right]^{\frac{1}{a}}\right)}{b} \quad (2.12)$$

where $W(\dots)$ is Lambert's W function [112]. With an explicit function for T_C , we can estimate the uncertainty in T_C by the root square sum of the uncertainty in the parameters in Eq. (2.12) multiplied by the partial derivative of Eq. (2.12) with respect to each of the parameters [113]. The parameters are P_C , P_0 , T_0 , a , and b .

$$U_{T_C} = \sqrt{\left(\frac{\partial T_C}{\partial P_C} U_{P_C}\right)^2 + \left(\frac{\partial T_C}{\partial P_0} U_{P_0}\right)^2 + \left(\frac{\partial T_C}{\partial T_0} U_{T_0}\right)^2 + \left(\frac{\partial T_C}{\partial a} U_a\right)^2 + \left(\frac{\partial T_C}{\partial b} U_b\right)^2} \quad (2.13)$$

Then, letting

$$D = W\left(\frac{b}{a} \exp\left[\frac{bT_0}{a}\right] T_0 \left[\frac{P_C}{P_0}\right]^{\frac{1}{a}}\right)$$

the partial derivatives of Eq. (2.12) with respect to the parameters are

$$\frac{\partial T_C}{\partial P_C} = \frac{D}{bP_C(D+1)} \quad (2.14a)$$

$$\frac{\partial T_C}{\partial P_0} = \frac{-D}{bP_0(D+1)} \quad (2.14b)$$

$$\frac{\partial T_C}{\partial T_0} = \frac{(a+bT_0)D}{bT_0(D+1)} \quad (2.14c)$$

$$\frac{\partial T_C}{\partial a} = \frac{-D[bT_0 + \ln(P_C/P_0) - aD]}{ab(D+1)} \quad (2.14d)$$

$$\frac{\partial T_C}{\partial b} = \frac{D(bT_0 - aD)}{b^2(D+1)} \quad (2.14e)$$

The uncertainties of the parameters, U_j in Eq. (2.13), are in general found by their own root

square sum procedure

$$U_j^2 = B_j^2 + R_j^2 \quad (2.15)$$

where the subscript j represents one of the parameters in Eq. (2.12). The total uncertainty of a particular parameter is composed of two parts, the systematic or bias uncertainty (B_j) and the precision or random uncertainty (R_j). In general, the bias uncertainty is contained in the measurement equipment and can be reduced, e.g. by using different equipment; the random uncertainty is inherent in any measured process and cannot be reduced by experimental techniques. The bias and precision uncertainties for each parameter will be discussed in the following.

2.1.8.1 Uncertainty in Initial Temperature

The bias uncertainty in the initial temperature is due to the standard limits of error of the K-type thermocouple used to measure the initial temperature. According to the Omega Engineering specifications, this is "the greater of 2.2 °C or 0.75%". The largest initial temperature used in this work, 413 K, leads to an uncertainty of ± 3 K; thus, $B_{T_0} = 3$ K. Bias uncertainty due to the A/D converter in the process meter is negligible compared to this uncertainty. The precision uncertainty is due to the limit of precision of the display on the Omega Engineering CNi3254 process meter used to control the process temperature. This is ± 0.05 K. The total uncertainty of the initial temperature is

$$U_{T_0} = \sqrt{(B_{T_0})^2 + (R_{T_0})^2} = \sqrt{(3 \text{ K})^2 + (0.05 \text{ K})^2} = 3 \text{ K} \quad (2.16)$$

2.1.8.2 Uncertainty in Initial Pressure

The bias uncertainty in the initial pressure is due to the standard error in the pressure transducer used to measure the initial pressure. Two different pressure transducers have been used in this study; the first, an Omega Engineering PX-303 (range: 0–50 psia), has a full scale uncertainty of 1.25%, or ± 0.625 psi (4309.2 Pa). The second transducer is an Omega Engineering MMA100V10T2D0T4A6

type (range: 0–5200 Torr) and was purchased because preliminary results of this uncertainty analysis indicated that the largest contributor to the uncertainty of T_C was the initial pressure measurement. The full scale uncertainty of the MMA type transducers is 0.05%, resulting in an uncertainty of ± 2.6 Torr (346.6 Pa), an order of magnitude lower than the PX-303 while also providing more than double the operating range. Total uncertainties using the appropriate pressure transducer are reported in each experimental section of this work; both transducers will be analyzed in this section. Bias uncertainty due to the signal acquisition equipment is negligible compared to the standard error in the pressure transducers.

The precision uncertainty is due to the limit of precision of the display on the Omega Engineering DP41-B process meter used to monitor the initial pressure. This is ± 0.005 Torr (0.666 Pa). The total uncertainty of the initial pressure is

$$U_{P_0} = \sqrt{(B_{P_0})^2 + (R_{P_0})^2} = \sqrt{(4309.2 \text{ Pa})^2 + (0.666 \text{ Pa})^2} = 4309.2 \text{ Pa} \quad (2.17\text{a})$$

$$U_{P_0} = \sqrt{(B_{P_0})^2 + (R_{P_0})^2} = \sqrt{(346.6 \text{ Pa})^2 + (0.666 \text{ Pa})^2} = 346.6 \text{ Pa} \quad (2.17\text{b})$$

2.1.8.3 Uncertainty in Compressed Pressure

The bias uncertainty in the compressed pressure is due to the standard error in the piezoelectric pressure transducer. According to the manufacturer's calibration, the deviation of the full scale output from linearity is less than 0.2%, indicating that $B_{T_C} = 0.5$ bar. The uncertainties in the signal acquisition equipment are negligible compared to this uncertainty. The precision uncertainty is due to the limit of precision of the output of the pressure, and is 5×10^{-7} bar. This is negligible compared to the bias uncertainty, so the total uncertainty of the compressed pressure is

$$U_{P_C} = B_{T_C} = 0.5 \text{ bar} \quad (2.18)$$

2.1.8.4 Uncertainty in the Specific Heat

The uncertainty in the specific heat comes from two sources. First is the uncertainty in the mixture composition and second is the uncertainty in the linear fit to the total specific heat. The uncertainty in the mixture composition can be estimated by the same method as is used for T_C . The specific heat is given by Eq. (2.8), so we can take partial derivatives of that equation with respect to the mole fractions of the species to find the total uncertainty

$$\begin{aligned} \left(U_{\hat{C}_p,\text{total}}\right)^2 &= \left(\frac{\partial \hat{C}_p}{\partial X_1} U_{X_1}\right)^2 + \dots + \left(\frac{\partial \hat{C}_p}{\partial X_n} U_{X_n}\right)^2 \\ &= (\hat{C}_{p,1} U_{X_1})^2 + \dots + (\hat{C}_{p,n} U_{X_n})^2 \end{aligned} \quad (2.19)$$

where n is the total number of species. In Eq. (2.19), it is assumed that the uncertainty in the specific heats of each species is negligible. This is considered an acceptable assumption for stable species such as the fuel molecules, oxygen, nitrogen, and argon. Experience with several kinetic mechanisms has shown that the typical variation in individual \hat{C}_p fits causes approximately 1 K changes in T_C .

The uncertainty of the mole fraction of the species is estimated differently depending on how the species was introduced to the mixing tank. For liquid fuel species, experiments with GC/MS have shown that there is approximately 5% variation in mole fraction from the expected value [64]; this value is adopted for the total uncertainty of all liquid fuels. The mole fraction of the gaseous species is determined by their partial pressures when filling; the mole fraction is related to the pressure by Dalton's Law of Partial Pressure [114, 115]

$$X_i = \frac{P_i}{P} \quad (2.20)$$

Table 2.1: Mixtures studied in the uncertainty analysis.

Fuel	Mole Fraction			
	Fuel	Oxygen	Nitrogen	Ar
Methylcyclohexane	0.0107	0.2240	0.0000	0.7653
<i>n</i> -Butanol	0.0676	0.2030	0.7294	0.0000
<i>i</i> -Pentanol	0.0531	0.1989	0.7480	0.0000
Propene	0.0854	0.1921	0.7225	0.0000

where P_i is the partial pressure of a species and P is the total pressure. It follows that

$$\begin{aligned}(U_{X_i})^2 &= \left(\frac{\partial X_i}{\partial P_i} U_{P_i} \right)^2 + \left(\frac{\partial X_i}{\partial P} U_P \right)^2 \\ &= \left(\frac{U_{P_i}}{P} \right)^2 + \left(\frac{-P_i}{P^2} U_P \right)^2\end{aligned}\tag{2.21}$$

The uncertainties of the pressures P_i and P are equal and can be estimated by the same procedure as in Sec. 2.1.8.2 since the same pressure transducer is used to measure the pressure. The total pressure P will be different for each species as it is filled. The order followed in these experiments is liquid fuel injection, followed by oxygen, then nitrogen, then argon.

A typical total pressure after filling is approximately 1300 Torr ($\approx 173,319$ Pa). The mixtures in Table 2.1 are the mixtures that will be analyzed in the following because they represent a worst case scenario in that the mole fraction of the fuel or oxygen is maximized in them.

Once the total specific heat has been calculated, a linear fit as a function of temperature is applied by least-squares estimation. Since there is an uncertainty in the specific heat, there is a corresponding uncertainty in the fit coefficients a and b . Following the methodology outlined by York et al. [116], the values and uncertainties of a and b are calculated iteratively. This procedure gives identical values of the slope, intercept, and standard errors as maximum likelihood estimation [116]. Equation (2.22) is reproduced from York et al. [116], and is presented as Eq. (13) in that

Table 2.2: Symbols in Eq. (2.22). Reproduced from the work of York et al. [116].

Symbol	Meaning
a, b	y intercept and slope of best line, $y = a + bx$
σ_a, σ_b	Standard errors of a and b
X_i, Y_i	“Observed” data points
r_i	Correlation coefficient between uncertainty in X_i and Y_i
$\omega(X_i), \omega(Y_i)$	Weights of X_i and Y_i
x_i, y_i	Least squares adjusted points: $\bar{X} + \beta_i, \bar{Y} + b\beta_i$
α_i	$\sqrt{\omega(X_i)\omega(Y_i)}$
W_i	$\frac{\omega(X_i)\omega(Y_i)}{\omega(X_i) + b^2\omega(Y_i) - 2r_i\alpha_i b}$
\bar{X}, \bar{Y}	$\frac{\sum W_i X_i}{\sum W_i}, \frac{\sum W_i Y_i}{\sum W_i}$
U_i, V_i	$X_i - \bar{X}, Y_i - \bar{Y}$
\bar{x}	$\frac{\sum W_i x_i}{\sum W_i}$
β_i	$W_i \left[\frac{U_i}{\omega(Y_i)} + \frac{bV_i}{\omega(X_i)} - (bU_i + V_i) \frac{r_i}{\alpha_i} \right]$
u_i	$x_i - \bar{x}$

work.

$$a = \bar{Y} - b\bar{X} \quad (2.22a)$$

$$b = \frac{\sum W_i \beta_i V_i}{\sum W_i \beta_i U_i} \quad (2.22b)$$

$$\sigma_a^2 = \frac{1}{\sum W_i} + \bar{x}^2 \sigma_b^2 \quad (2.22c)$$

$$\sigma_b^2 = \frac{1}{\sum W_i u_i^2} \quad (2.22d)$$

where the symbols in Eq. (2.22) are defined in Table 2.2. The general formulation is given here because it will be reused in ??; application to this section will be given below.

In this section, X_i are the temperatures at which Eq. (2.10) is evaluated and Y_i are the total specific heats evaluated from Eq. (2.10). The weighting of the specific heats— $\omega(Y_i)$ —is taken to

be the reciprocal of the uncertainty as calculated by Eq. (2.19). Furthermore, there is no uncertainty in the abscissa (i.e. the temperature) and $\omega(X_i) = 1$. Finally, since there is no uncertainty in the temperature, there is no correlation between the uncertainties, i.e. $r_i = 0$.

First, the slope b is estimated by simple least-squares regression of the total specific heat on the temperature. Then, this slope is used to estimate the adjusted weighting of each point, W_i . Next, U_i and V_i are calculated based on the adjusted weighting. Using U_i , V_i , and β_i , a new value of the slope is calculated from Eq. (2.22b), and the process is repeated until the slope converges. Convergence is determined when the slope changes by less than 0.001 on successive iterations. Then, using Eq. (2.22a), the intercept a is calculated. Finally, the standard error of each parameter is calculated using the final values of the slope and intercept with Eqs. (2.22d) and (2.22c).

For the mixtures considered in this study, the correlation coefficient for the linear fits are greater than 0.99 (i.e. $r^2 > 0.99$), indicating a good fit.

2.2 Fast Sampling System

The fast sampling system (FSS) used in this work is a commercial system supplied by SME-Tec GmbH. from Germany. The FSS is composed of two parts, the gas sampling valve (GSV) and the Controller. A schematic of the GSV is shown in ???. Gases are admitted from the reaction chamber into the heated carrying tubes through the poppet-style valve on the left of the GSV. The sampled gases are then conducted through the GSV outlet into the 150 mL sampling bottle.

A schematic of the GSV assembly is shown in ???. The GSV is mounted to the RCM by a custom-made end plug. The reaction chamber is sealed by an O-ring on the small- and large-diameter portions of the GSV. The depth that the GSV is inserted into the reaction chamber is adjustable by adding or removing shims in the end plug assembly. The insertion depth is chosen so that the tip of the GSV is outside the boundary layer on the end wall.

The portion of the GSV protruding into the reaction chamber has minimal effect on the homogeneity of the reaction chamber. Moreover, the removal of samples also has minimal effect on the

measured ignition delay. This has been verified experimentally by measuring the ignition delay with and without the GSV present, and with and without sampling occurring. In both cases, the difference in ignition delay was statistically insignificant for $\alpha = 0.05$.

The close-open-close (COC) cycle of the GSV is controlled by a mass-spring system. The poppet face is connected to a rod running the length of the GSV and connected to the mass at the rear of the valve. To open the poppet, the mass is accelerated forward by passing current through the coil around the mass. The rod is also connected to a spring that is used to restore the poppet to its original position after being extended.

The GSV has an adjustable COC time, by adjusting the distance the plate is allowed to move. Furthermore, the GSV has the ability measure the displacement of the mass, allowing the direct measurement of the COC time and the absolute time of opening.

The GSV controller is triggered by a 5 V signal from the cDAQ. The timing of the trigger signal is controlled by the LabView VI. The pressure signal from the reaction chamber is read from the cDAQ in 1 ms chunks in a loop. On each loop iteration, the maximum pressure is checked against a desired trigger pressure; when the reaction chamber pressure exceeds the trigger pressure, the cDAQ sends the trigger to the GSV controller. The GSV controller has an adjustable delay (4.5–50 ms) that is used to control the timing of the opening of the GSV during the induction period.

The absolute opening time of the GSV is thus dependent on three parameters:

1. The cable delays from the PC to the cDAQ; from the cDAQ to the GSV controller; and from the GSV controller to the GSV itself
2. The processing time of the LabView VI
3. The delay set in the GSV controller.

However, since the absolute opening time of the GSV can be measured by the signal sent from the GSV to the controller (and thence to the cDAQ), the uncertainty in the opening time is actually quite small, and is related to the cable delay in sending the COC signal from the GSV to the cDAQ

Check
this
range

and the precision of the A/D conversion in the cDAQ. The uncertainty of the absolute opening time is thus estimated as $\pm 1 \mu\text{s}$.

Verify
this
number

Furthermore, the correspondence of the COC signal from the valve with the physical valve movements has been experimentally verified by high speed video. Frames from these videos are shown in ???. The frames show that the opening and closing times of the valve face correspond closely with repeatable points in the peak of the voltage.



2.2.1 Experimental Procedure

Prior to an experiment, the GSV and sampling bottle are vacuumed to less than 1 Torr. The reaction chamber is vacuumed and filled in the same procedure as described previously, and the compression is triggered. For a given trigger pressure and controller delay, the GSV opens at some time after the EOC and removes a gas sample from the reaction chamber. The sample is diluted by high purity helium. Then the sample bottle is disconnected from the GSV and transported to the Gas Chromatograph/Mass Spectrometer, where the sample undergoes analysis.

2.3 Gas Chromatograph/Mass Spectrometer

2.3.1 Theory of Gas Chromatography/Mass Spectrometry

2.3.1.1 Gas Chromatography

A gas chromatograph (GC) is a device that physically separates components of a gas sample by means of a tube—known as a *column*—lined or filled with a substance that interacts with the components in the sample. The sample is transported the length of the column by a flow of carrier gas, usually helium or hydrogen, also known as the *mobile phase*. A detector is placed at the outlet of the column to measure the amount and type of components eluted from the column.

The separation of the gaseous components in the sample is effected by the interaction of the sample with the lining of the column, known as the *stationary phase*. Gaseous species that have little interaction with the stationary phase and spend most of their time in the mobile phase are eluted from the column before species that interact strongly with the stationary phase and spend little time in the mobile phase [117].

The column is placed in an insulated oven so that its temperature may be controlled. The column temperature in a given analysis may be constant or may be controlled as a function of time. Since the time that a given component takes to move through the column is a function of temperature, this facility allows optimization of the elution time of the various components in the sample.

The injector of the GC is also temperature controlled; the temperature of the injector is set high enough so that all components (including the solvent, if any) are vaporized but not so high that the sample starts to degrade. On the present GC, a split/splitless injector is installed. This allows for operation in the split mode, where a percentage of the injected sample is removed from the injector prior to injection onto the column, or in the splitless mode, where nearly all of the sample is injected into the column. The split mode is used in this work. The amount of sample removed is controlled

by a valve in the injector. The split ratio is calculated according to Eq. (2.23)

$$\text{Split Ratio} = \frac{\text{Column Flow} + \text{Vent Flow}}{\text{Column Flow}} \quad (2.23)$$

where the column flow is the carrier gas flow rate at the head of the column and the vent flow is the flow out of the splitter vent [117].

A GC may also be equipped with a gas sample injection valve, in addition to the split/splitless injector. This valve is connected serially prior to the split/splitless injector. The present GC is equipped with a 10-port Valco sample injection valve, shown schematically in Fig. 2.5. Each port is numbered, and curved lines indicate connections between ports. The sample injection valve is used to inject a consistent mass of sample into the column with each injection. This permits reliable quantification of the components in the sample. First, the sample is loaded into the sample loop when the valve is in the “load” position, as in Fig. 2.5a. Then, the valve is electrically actuated at the start of the GC run to rotate the connections into the “inject” position. This allows carrier gas to flow through the sample loop and push the sample from the sample loop into the column via the split/splitless injector (Fig. 2.5b). The valve is then actuated again to remove the sample loop from the carrier gas path and restore the “load” position (Fig. 2.5a).

The sample injection valve is equipped with a heater to maintain the valve body at a constant temperature and the entire assembly is installed in an insulated box. However, this heater is insufficient to heat the tubes attached to the valve, so an additional heater rope is installed in the insulated box. To measure the temperature of the sample loop directly, a thermocouple is fixed to the sample loop by ceramic cement. The temperature of the sample loop is used to control the power provided to the rope heater, while a built-in thermocouple is used to control the power provided to the valve body heater, so that the sample loop remains at a constant temperature.

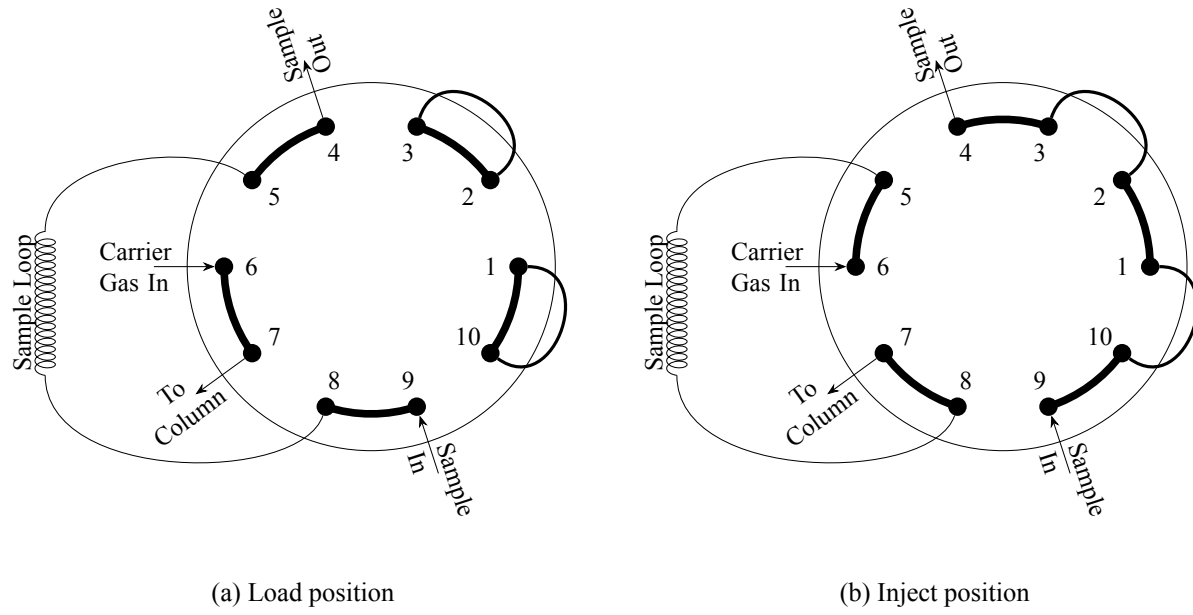


Figure 2.5: GC/MS sample injection valve.

2.3.1.2 Mass Spectrometry

Many types of detectors are available for GC analyses. These commonly include flame ionization detectors, thermal conductivity detectors, and mass spectrometers. In this work, a mass spectrometer is used to identify and quantify the species eluted from the column.

The fundamental operation of a mass spectrometer (MS) is to detect the spectrum of ions in a given sample. The MS generates this spectrum by detecting the mass-to-charge (m/z) ratios of the ions. Ions are generated from the effluent of the column—which includes sample components, mobile phase, and column bleed, collectively called *analytes*—by an ionization source, typically either electronic or chemical in nature. Nearly all of the ions generated will have a single charge, $z = 1$ [118]; thus, the m/z value of the ions is also equal to the mass of the ion.

In this work, electron ionization (EI) is used to generate the ions for analysis. The effluent from the column is passed in front of an electron source so that the electrons impact the analyte molecules and remove an electron, generating a positive ion. EI is a *hard ionization* technique, in that the electron impact transfers a significant amount of energy to the analyte molecule [118]. The additional energy causes the ion to fragment into two or more pieces; the spectrum of these

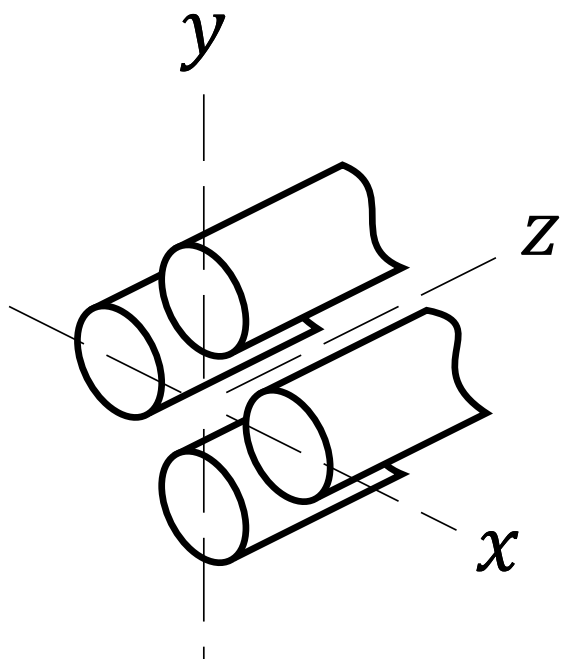


Figure 2.6: Schematic of the transmission quadrupole in an MS.

fragments is characteristic for a given molecule and can be used as a “fingerprint” to identify the source molecule for a given spectrum.

After ionization, the fragments are formed into a beam and accelerated out of the ionization chamber towards the detector. Several detectors are available, including time-of-flight and transmission quadrupole. All of these detectors require high vacuum to avoid impact of the ion beam with extraneous species prior to reaching the detector. The vacuum is achieved in the present MS by a two-stage design, using a rotary vane pump in series with a turbomolecular pump to achieve ultimate pressures of approximately 2 Pa.

The MS used in this study is a transmission quadrupole type, shown schematically in Fig. 2.6. The transmission quadrupole separates specific ions from the ion beam by means of a time-varying electric field. Conceptually, the quadrupole can be imagined as four round rods, arranged in a cross pattern, with their long axes aligned parallel to the ion beam (i.e. the z axis). The ions are admitted to the rods at one end (e.g. at the origin in Fig. 2.6) and the detector is placed parallel to the $x - y$ plane in Fig. 2.6 at the other end of the rods(not shown in Fig. 2.6). A positive DC voltage is applied to one pair of the rods, while a negative DC voltage is applied to the other pair of rods;

in addition, an AC voltage is applied simultaneously to all four rods. Assuming a specific ratio of AC amplitude to DC amplitude, ions of a certain m/z will remain in the ion beam and reach the detector. Then, holding the AD:DC amplitude ratio fixed, the amplitudes are ramped with a known function of time. This varies the particular m/z that will remain in the ion beam and reach the detector to be recorded [118], generating a mass spectrum.

The voltage amplitudes are ramped many times per second—typical ramp times range from 0.05–0.5 s, depending on the range of m/z values to be acquired—so that many spectra are acquired during the elution of a given chemical compound from the column, which typically occurs on the order of a few seconds. For a given scan from the lowest to the highest amplitude, the number of ions of each m/z is measured at the detector. This information is typically presented in the form of a relative intensity plot. The abscissa is the (integer) m/z while the ordinate is the intensity of a particular m/z scaled by the maximum intensity of all the m/z in a given scan. It is not required that the m/z be integers, although they are usually presented as such for simplicity. An example of a mass spectrum for a given time in a GC/MS analysis is shown in Fig. 2.7.

In addition to the mass spectrum, the MS reports the total ion current (TIC), also known as the total ion chromatogram. This is the sum of all of the mass intensities for a given scan. A sample TIC is plotted in Fig. 2.8 where the abscissa is time in min and the ordinate is an arbitrary unit. Finally, the MS can also report the mass chromatogram (MC), which is the chromatogram for a specific m/z as a function of time.

2.3.2 Identification and Quantification of Species using GC/MS

Species are identified using a GC/MS system by their unique mass spectra. Each peak in the TIC typically represents one compound eluting from the column, although in theory each peak can represent more than one compound if the compounds are retained similarly by the column. The peak is caused by an increase in the number of ions reaching the detector on each scan relative to the baseline as the compound elutes and is ionized. As mentioned previously, many scans of the desired m/z range are conducted over the time that a compound is eluting from the column. To

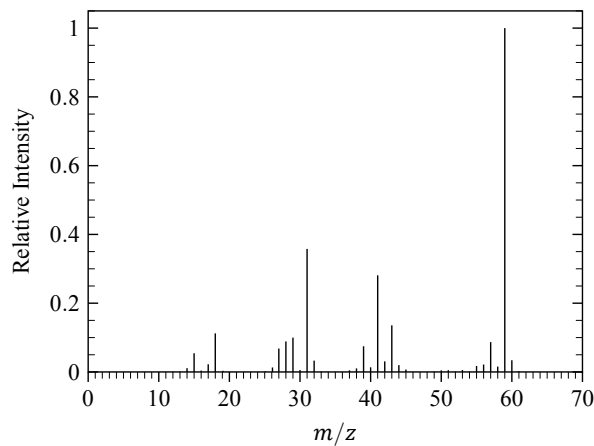


Figure 2.7: Example mass spectrum for a given scan during a GC/MS analysis

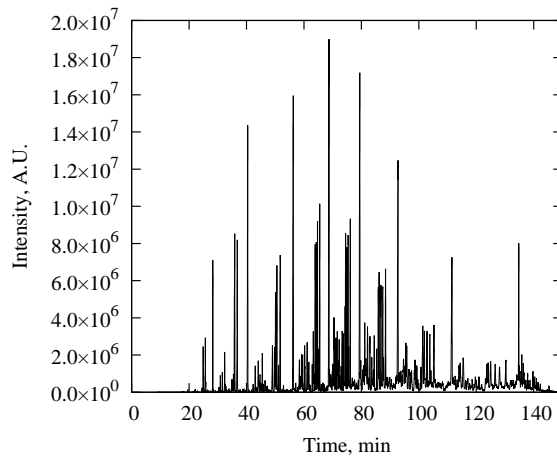


Figure 2.8: Example TIC for a GC/MS analysis

determine the identity of a compound in a given peak, the set of mass intensities over the peak are averaged and the background spectrum is subtracted; this average spectrum is compared to a database supplied by the National Institute of Standards and Technologies (NIST). The database returns several suggested species with a degree of matching parameter indicating how well the supplied spectrum matches the spectrum in the database.

In this work, the external standard method of quantification is used. This requires that calibration curves for each of the species of interest be created, relating the area of the peak in the TIC to the number of moles of analyte reaching the detector. The number of moles of analyte can in turn be related to the number of moles of sample in the gas sample injection valve sample loop. Once the calibration curve is generated, it is used to relate the measured area of the peak of particular component to its mole fraction. Detailed methods for the construction of calibration curves will be given in Sec. 2.3.3.

2.3.3 Experimental Procedure

The GC/MS used in this study is a Shimadzu model QP-2010S, equipped with a 10-port Valco sample injection valve and split/splitless injector, as mentioned previously. The column used is a Phenomenex model ZB-5MS capillary column with length 30 m, inner diameter 0.25 μm , and film

thickness of 0.25 μm . The operating parameters of the GC/MS (known as the “method”) are shown in ??.

The pressure in the gas injection valve sample loop is monitored by an MMA type pressure transducer, the same model as used in Sec. 2.1.8.2. The sample outlet in Fig. 2.5 is open to the atmosphere so that a consistent pressure is maintained in the sample loop. The volume of the sample loop is 10 μL . With the temperature, pressure, and volume of the sample loop known, the number of moles of sample can be calculated by the ideal gas law.

A calibration curve is built for the major species by the following procedure. First, the sample bottle is vacuumed to less than 1 Torr. Mixtures of the species of interest in the liquid state are prepared by massing each component on a high-accuracy AND-201 scale. A small mass of this mixture is drawn into a syringe and massed on the same scale. The mixture is injected through a septum into the sample bottle. Then the sample bottle is filled with high-purity nitrogen so that the largest mole fraction of a species of interest is approximately 0.001. The sample bottle is connected to the sample injection valve on the GC/MS and the valve on the sample bottle is opened and quickly closed. The pressure is allowed to equalize and the GC/MS is started.

After the completion of the GC/MS method, the total ion chromatogram (TIC) is analyzed by the Shimadzu GCMS Post-run Analysis software (version XXXX). Each peak is automatically integrated by the software so that its area can be found. The peak area is then related to the number of moles of sample sent to the detector by linear least-squares regression. This calibration curve is used to compute the mole fraction of any given peak area for that species.

Chapter 3

The Butanol Isomers

Table 3.1: HHV of Ethanol, Butanol Isomers, and Gasoline

Compound	Ethanol [21]	Butanol Isomers [21]	Gasoline [22]
HHV [MJ/kg]	29.67	≈ 36	48.46

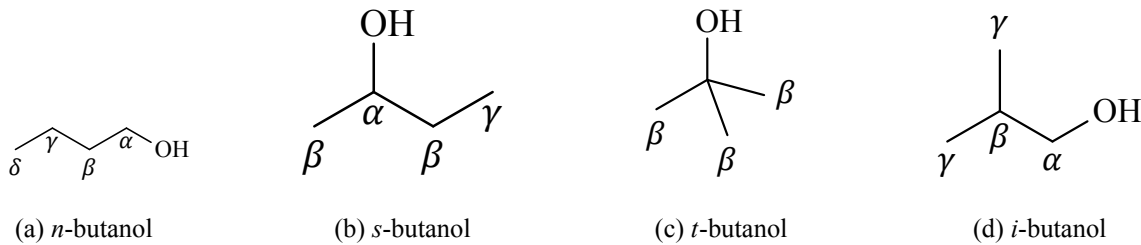


Figure 3.1: Skeletal structures of the butanol isomers

3.1 Structure of the Butanol Isomers

Butanol is the four carbon alcohol, and has four isomers: *n*-butanol (1-butanol); *s*-butanol (2-butanol); *t*-butanol (2-methyl-2-propanol); and *i*-butanol (2-methyl-1-propanol). The skeletal structures of the four isomers are shown in Fig. 3.1. The carbon atoms in the skeleton are labeled according to their distance from the hydroxyl moiety; the α carbon is the closest to the hydroxyl, followed by β , γ , and δ carbons. Not all of the butanols have all of the types of carbons listed here, due to varying

chain lengths. For instance, *t*-butanol has one α carbon (not labeled), three β carbons, and no γ or δ carbons.

Three of the butanol isomers can be produced by biological pathways (*n*-, *s*-, and *i*-butanol) [26, 27], making them candidates for the “second-generation” of biofuels [25, 26]. Although *t*-butanol does not have an identified biological production pathway, it has commercial significance as an octane enhancer. In addition, the four isomers of butanol represent the smallest alcohol system with all four types of branching in the skeleton. This makes them an excellent candidate to build kinetic models that can be extended to larger alcohols with similar structures.

Table 3.1 shows a comparison of the higher heating value of the butanol isomers with ethanol and gasoline. The higher energy density of the butanol isomers allows them to be blended in gasoline in higher proportions and reduces the volumetric fuel economy (e.g. mpg) impact of replacing gasoline with biofuels.

3.2 Experimental Procedure

The reactants used in this study, along with their purities, are shown in Table 3.2. To determine the relative proportions of each reactant in the mixture, the absolute mass of fuel, the equivalence ratio (ϕ), and the oxidizer ratio ($X_{O_2} : X_{inert}$, where X indicates mole fraction) are specified. *s*- and *i*-Butanol are liquid at room temperature and have relatively low vapor pressure; therefore, each is massed in a syringe to within 0.01 g of the specified value. *t*-Butanol is solid at room temperature (melting point: 25 °C), and is melted before being handled in the same procedure as the other fuels. The 17 L mixing tank is vacuumed to an ultimate pressure less than 5 Torr prior to the injection of the liquid fuel through a septum. Proportions of O₂ and N₂ are added manometrically at room temperature. The preheat temperature of the RCM is set above the saturation point for each fuel to ensure complete vaporization. A magnetic stirrer mixes the reactants. The temperature inside the mixing tank is allowed to equilibrate for approximately 1.5 h.

This approach to mixture preparation has been validated in several previous studies by with-

drawing gas samples from the mixing tank and analyzing the contents by GC/MS [64], GC-FID [94], and GC-TCD [90]. These studies have verified the concentration of *n*-butanol, *n*-decane, and water, respectively. In addition, both the work by Kumar et al. [94] on *n*-decane and the study of Weber et al. [64] on *n*-butanol confirmed that there was no fuel decomposition over the course of a typical set of experiments. Furthermore, within this study, each new mixture preparation is checked against previously tested conditions to ensure reproducibility.

Table 3.2 shows the experimental conditions considered in this study. The compressed pressure conditions have been chosen to match the previous *n*-butanol study [64], but also to provide data in regions not covered extensively in previous work. In addition, the fuel loading conditions have been chosen to complement previous work; the studies by Stranic et al. [59] and Moss et al. [55] used relatively dilute mixtures, so we have included higher fuel loading conditions. Furthermore, the compressed temperature conditions we have studied ($T_C = 715\text{--}910\text{ K}$) have not been examined in any other study, to our knowledge.

Each compressed pressure and temperature condition is repeated at least six times to ensure repeatability. The mean and standard deviation of the ignition delay for all runs at each condition are calculated. As an indication of repeatability, the standard deviation is less than 10% of the mean in every case. Representative experimental pressure traces for simulations and presentation are then chosen as the closest to the mean.

3.3 Experimental Results

Figure 3.2 shows the ignition delays of the four isomers of butanol measured in the RCM, at compressed pressure of $P_C = 15\text{ bar}$ for stoichiometric mixture in air. The dashed line for each isomer is a least squares fit to the data. The vertical error bars are two standard deviations of the measurements of the ignition delay. The standard deviation is computed based on all the runs at a particular compressed temperature and pressure condition. A conservative estimate of the uncertainty in T_C was calculated in our previous work to be approximately 0.7–1.7 %. Due to the similar nature of

Table 3.2: Experimental Conditions and Reactant Purities

Reactant (Purity)					Equivalence Ratio ϕ	Compressed Pressure P_C (bar)
s-butanol (99.99%)	i-butanol (99.99%)	t-butanol (99.99%)	O ₂ (99.999%)	N ₂ (99.995%)		
Mole Percentage						
3.38			20.30	76.32	1.0	15
3.38			20.30	76.32	1.0	30
	3.38		20.30	76.32	1.0	15
	3.38		20.30	76.32	1.0	30
		3.38	20.30	76.32	1.0	15
		3.38	20.30	76.32	1.0	30
		1.72	20.65	77.63	0.5	30
		6.54	19.63	73.83	2.0	30

these experiments, and the similar properties of the fuels, this estimate is considered to be valid for this study as well.

Figure 3.2 demonstrates the differences in reactivity between the isomers for stoichiometric fuel/air mixtures at compressed pressure $P_C = 15$ bar. *n*-Butanol is clearly the most reactive, followed by *s*- and *i*-butanol, which have very similar reactivities in this temperature and pressure range. *t*-Butanol is the least reactive.

The order of reactivity found in the RCM at 15 bar agrees with the shock tube study at higher temperatures (approximately 1275–1667 K) and lower pressure (1.5 atm) by Stranic et al. [59] but differs slightly from the studies of Moss et al. [55] who measured ignition delays in a shock tube near 1.5 atm and between 1275–1400 K, and Veloo and Egolfopoulos [31] who measured atmospheric-pressure laminar flame speeds. In particular, Moss et al. [55] and Veloo and Egolfopoulos [31] found distinct differences in reactivity between *s*- and *i*-butanol, but the present study and the study by Stranic et al. [59] found that they were nearly indistinguishable in terms of reactivity under the conditions investigated. In addition, Stranic et al. [59] noted some disagreement between their shock tube ignition data and the data of Moss et al. [55] but their attempts to isolate the cause could not discern what the difference might be caused by.

Further, the order of the reactivity of the butanol isomers also shows complex temperature and

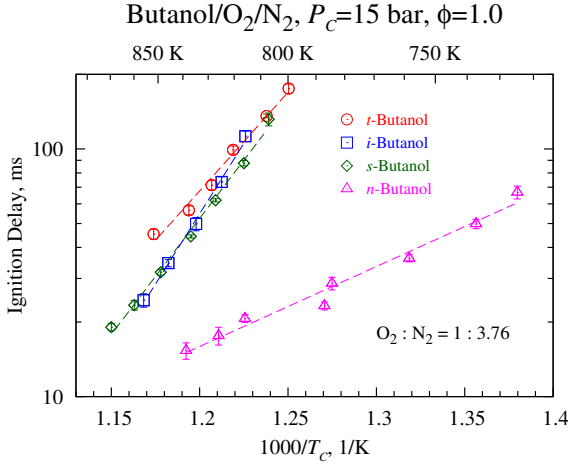


Figure 3.2: Ignition delays of the four isomers of butanol at compressed pressure $P_C = 15$ bar. Dashed lines are least squares fits to the data.

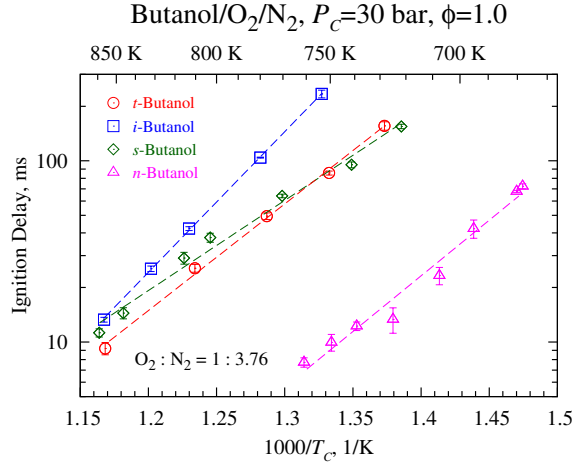


Figure 3.3: Ignition delays of the four isomers of butanol at compressed pressure $P_C = 30$ bar. Dashed lines are least squares fits to the data.

pressure dependence. This is demonstrated by the results shown in Fig. 3.3. In Fig. 3.3, the order of reactivity is different than in Fig. 3.2, where the only variation between the plots is the compressed pressure; in Fig. 3.3 the compressed pressure is $P_C = 30$ bar. Fig. 3.3 shows *i*-butanol to be the least reactive, *s*-butanol to be less reactive than *t*-butanol (but similar), and *n*-butanol to be the most reactive. Interestingly, the results of the shock tube study by Stranic et al. [59] differ from those in the current study at higher pressure (despite the agreement at lower pressure). In their study, Stranic et al. [59] found *i*- and *n*-butanol to have similar reactivity near 43 atm in the temperature range of 1020–1280 K, whereas in the present study we find *i*-butanol to be the least reactive of all four isomers at a pressure of 30 bar and over the temperature range (715–910 K) investigated.

The fact that *t*-butanol becomes relatively more reactive than *i*- and *s*-butanol as pressure increases is surprising at first glance, and the reasons are not immediately apparent. Closer examination of the pressure traces for each experiment gives one clue as to the cause of the increased reactivity. Figure 3.4 shows the pressure traces for the *t*-butanol experiments at 15 bar for stoichiometric mixtures in air. It is evident that there is some pre-ignition heat release, because the reactive pressure trace diverges from the non-reactive case prior to the ignition event. Of the other isomers of butanol, only *n*-butanol shows any visible heat release prior to the main ignition event at 15 bar.

Figure 3.5 shows the pressure traces for *t*-butanol experiments at 30 bar for stoichiometric mix-

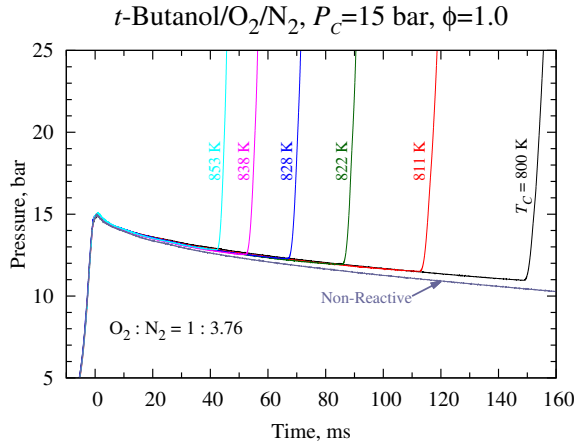


Figure 3.4: Pressure traces of the 15 bar *t*-butanol experiments, in stoichiometric air.

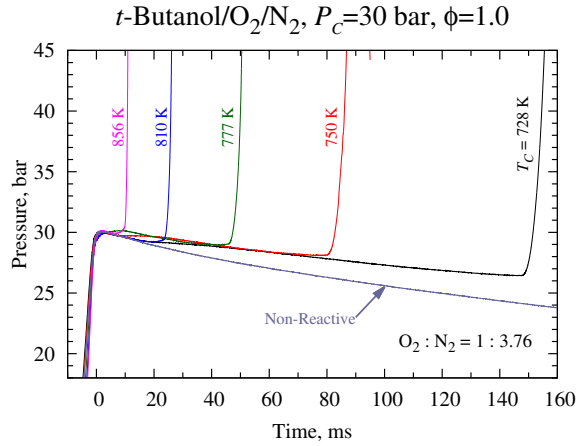


Figure 3.5: Pressure traces of the 30 bar *t*-butanol experiments, in stoichiometric air.

tures in air. The effect of pre-ignition heat release is even more striking in this figure, with substantial changes in the slope of the pressure trace during the reactive runs. Comparing to the pressure traces of the other isomers once again shows that the magnitude of the pre-ignition heat release for *t*-butanol is much greater. Despite the appearance of early pressure rise, which is typically indicative of two-stage ignition and low temperature chain branching, we do not find a negative temperature coefficient region in terms of the ignition delay response for any *t*-butanol experiments. Therefore, we adopt the phrase “pre-ignition heat release” rather than “two-stage ignition” in this work.

In an effort to understand the reactions causing the pre-ignition heat release, further experiments are conducted for *t*-butanol at $P_c = 30$ bar, for equivalence ratios of 0.5 and 2.0 in air. Figure 3.6 shows Arrhenius plots of the ignition delays for the three equivalence ratios. As with the previous *n*-butanol experiments at 15 bar [64] $\phi = 0.5$ is the least reactive and $\phi = 2.0$ is the most reactive. The slopes are similar, indicating that the overall activation energies are similar for the conditions investigated.

A more interesting comparison is of the pressure traces of the three equivalence ratios. It is clear from Figs. 3.5, 3.7, and 3.8 that there are qualitative differences in the pre-ignition heat release between the three equivalence ratios. This is most likely due to the effect of the increased (reduced)

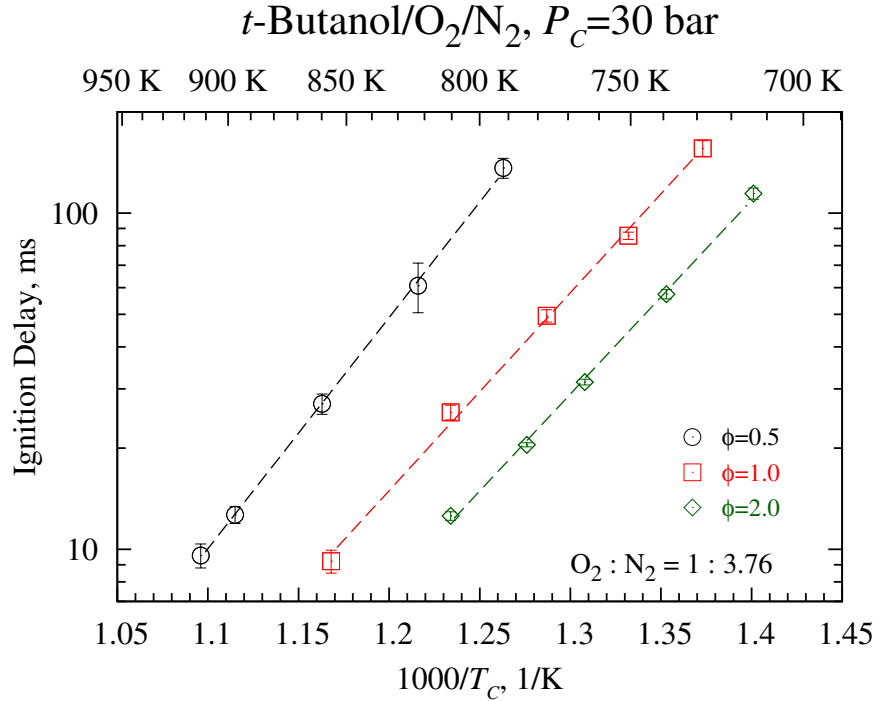


Figure 3.6: Ignition delays of three equivalence ratios of *t*-butanol in air, for $P_C = 30$ bar. Lines represent least squares fits to the data.

fuel mole fraction in the $\phi = 2.0$ ($\phi = 0.5$) case, since the mole fraction of fuel is changed by +93% (-49%) compared to the $\phi = 1.0$ case, while the mole fraction of oxygen changes by only -3% (+2%) compared to the $\phi = 1.0$ case, as shown in Table 3.2. Therefore, it appears that the qualitative change in pre-ignition behavior is due to the change of fuel mole fraction, where higher fuel loading promotes pre-ignition heat release.

3.4 Simulation Results

Simulations are performed with the kinetic mechanism from Sarathy et al. [119] and a recent mechanism discussed in Hansen et al. [34] and Merchant et al. [120] that is denoted as the MIT mechanism hereafter. Other recent mechanisms, such as the mechanism from Frassoldati et al. [121] do not include low temperature chemistry and are therefore unable to reproduce the low-temperature ignition delays measured in this study. The study by Sarathy et al. [119] validated their model for a wide set of the existing experimental data. In terms of ignition delays, this included the data from

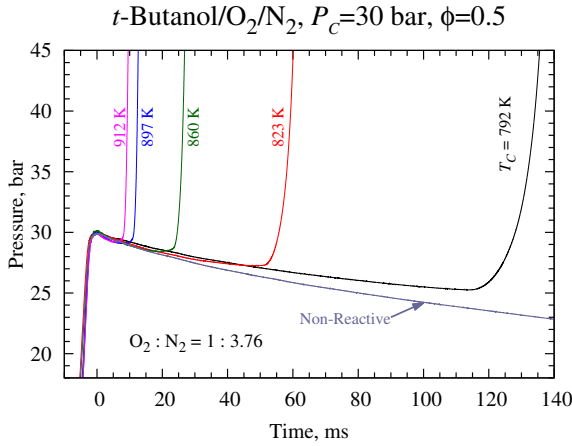


Figure 3.7: Pressure traces of the 30 bar *t*-butanol experiments, $\phi = 0.5$ in air.

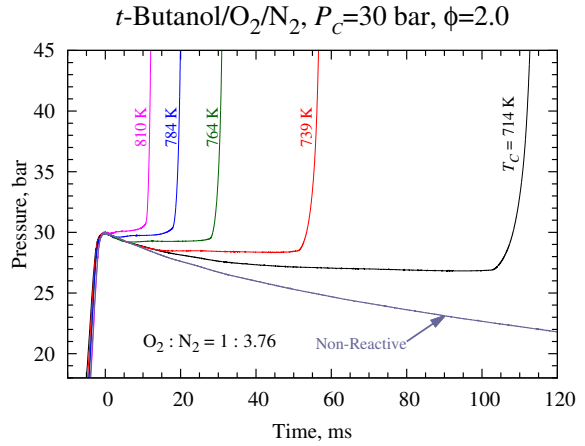


Figure 3.8: Pressure traces of the 30 bar *t*-butanol experiments, $\phi = 2.0$ in air.

the study of Stranic et al. [59] up to 48 atm, our previous study on *n*-butanol [64], and the data being published in this study at 15 bar. Importantly, the mechanism of Sarathy et al. [119] was validated only for the 15 bar RCM data for all four isomers, but not the 30 bar data also being published here. The MIT mechanism [34, 120] was validated for *i*-butanol experiments, including pyrolysis and low pressure premixed flames; although the model includes all four isomers of butanol as reactants, it has not been optimized for any of the isomers except *i*-butanol.

Figures 3.9 and 3.10 show comparison of the VPRO simulations with the experimental data using the mechanism of Sarathy et al. [119]. As Sarathy et al. [119] showed in their work (and as we show here in Fig. 3.9), they found good agreement of the model predictions with the present RCM data at 15 bar. At $P_C = 30$ bar (Fig. 3.10), similar degree of agreement is found for *t*-butanol and *s*-butanol compared to $P_C = 15$ bar, although the *s*-butanol results are under-predicted at high temperature and over-predicted at low temperature. While the model of Sarathy et al. [119] is able to well capture the overall activation energy of *i*-butanol, it under-predicts the experimental data by about a factor of 2–3. The *n*-butanol data are over-predicted by about a factor of 1.5. Nevertheless, this agreement is quite good, especially considering that the model is not validated for these conditions.

VPRO simulations for *n*- and *s*-butanol (and also some conditions for *t*-butanol) using the MIT

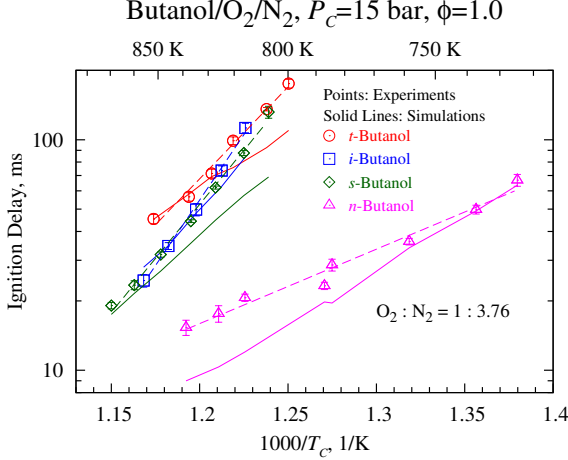


Figure 3.9: $P_c = 15$ bar, stoichiometric mixtures in air. Comparison of VPRO simulations using the kinetic mechanism of Sarathy et al. [119] with experimental ignition delays.

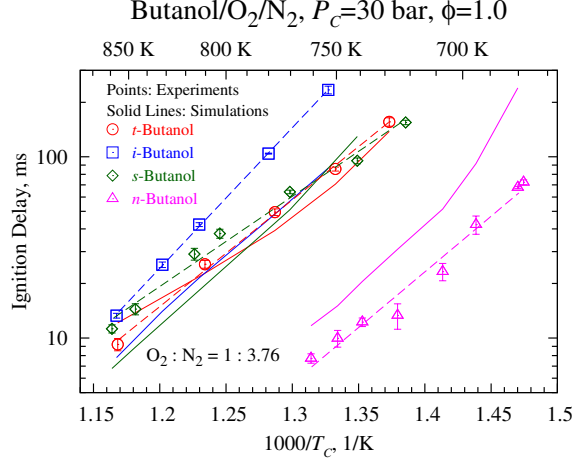


Figure 3.10: $P_c = 30$ bar, stoichiometric mixtures in air. Comparison of VPRO simulations using the kinetic mechanism of Sarathy et al. [119] with experimental ignition delays.

mechanism [34, 120] do not ignite during the duration of the simulations (the same as the experimental duration), and therefore no simulations are shown for these fuels. In Fig. 3.11, VPRO simulations at 15 and 30 bar using both mechanisms are shown for *i*-butanol. It is seen that the mechanism from Sarathy et al. [119] is in better agreement at 15 bar. However, at 30 bar the MIT mechanism [34, 120] over-predicts the ignition delay (as at 15 bar), while the Sarathy et al. [119] mechanism under-predicts the ignition delay. The reason for these diverging predictions will be explored and discussed below.

The agreement of the mechanism by Sarathy et al. [119] with the off-stoichiometric mixtures of *t*-butanol is also quite good, as shown in Fig. 3.12. Figures 3.13a, 3.13b, and 3.13c show more detailed comparisons of the simulated pressure traces and the experimental results, for similar temperatures at the three equivalence ratios, respectively. Clearly, the simulations also exhibit some pre-ignition heat release. In general, the simulations qualitatively predict the pre-ignition heat release behavior at all three equivalence ratios. The $\phi = 0.5$ case has the least heat release and the $\phi = 2.0$ case has the most. Although the simulations are unable to match the heat release behavior quantitatively, they match the experimental ignition delays quite well. Considering the model is not validated for this temperature, pressure, and equivalence ratio regime, the mismatch of the

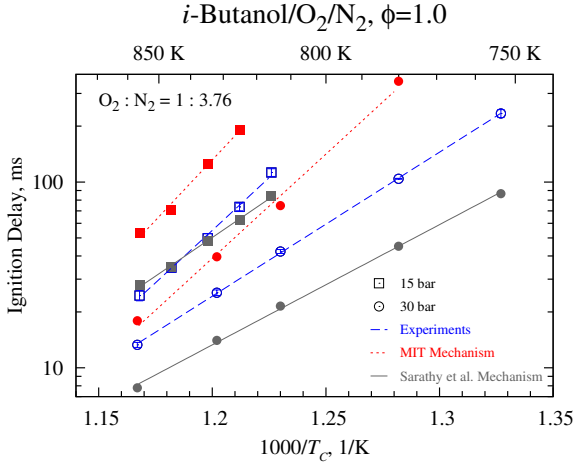


Figure 3.11: Comparison of VPRO simulations using the kinetic mechanism of Sarathy et al. [119] (solid lines) and the MIT mechanism [34, 120] (dotted lines) with the experimental ignition delay results (dashed lines) for stoichiometric mixtures of *i*-butanol in air at $P_C = 15$ bar (squares) and $P_C = 30$ bar (circles).

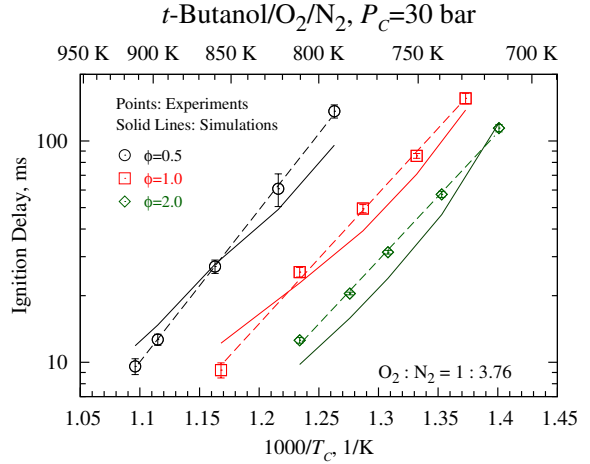


Figure 3.12: Comparison of the simulations using the kinetic mechanism of Sarathy et al. [119] for three equivalence ratio mixtures of *t*-butanol in air at $P_C = 30$ bar.

pre-ignition behavior may not be of critical importance, depending on the application.

3.5 Discussion

The relatively good agreement of the mechanism of Sarathy et al. [119] with the experimental data, even for conditions at which the mechanism has not been validated, suggests that using the mechanism to further interpret our experimental data is not a facile exercise. In particular, Figs. 3.14–3.17 show the initial steps of the fuel breakdown process for each isomer. The percentages listed are the percent of the reactant that is consumed to produce the product shown, by all the reactions that can produce that product from the reactant, except where one particular reaction is noted. These numbers are determined by integrating the rate of production or consumption of each species by each reaction up to the point of 20% fuel consumption, and normalizing each reaction by the total produced or consumed of each species up to that point. The 20% fuel consumption point is chosen because it is before small molecule chemistry takes over to drive the ignition, and it has been used previously [64, 119]. The rates of production are taken from a CONV simulation, with initial con-

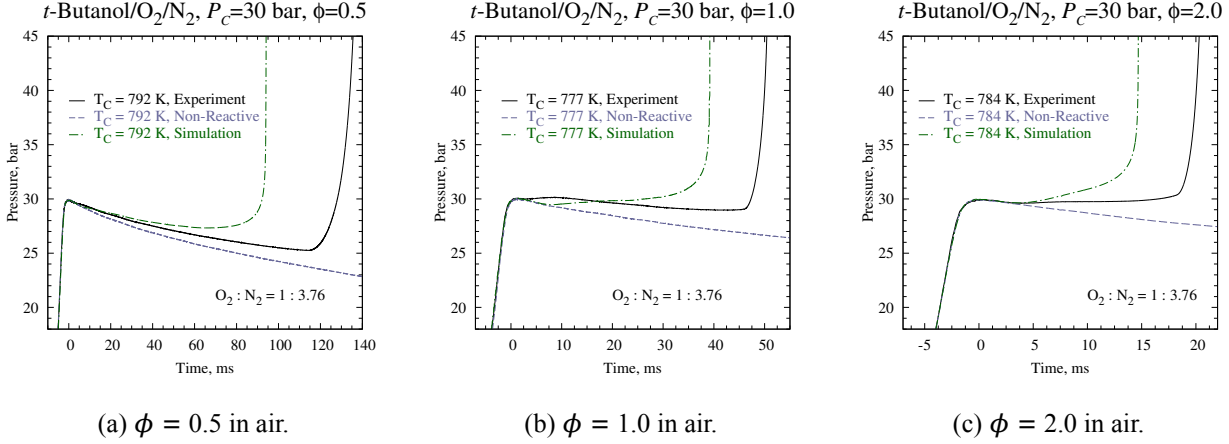


Figure 3.13: Pressure traces of selected *t*-butanol experiments compared with the corresponding non-reactive and simulated traces, using the mechanism of Sarathy et al. [119].

ditions 750 K and 15 bar as well as 750 K and 30 bar. These conditions are representative of typical conditions after compression in the present RCM experiments. The plain text percentages on top of the arrows are the 15 bar case and the bold numbers underneath are for the 30 bar case.

In the following discussion, carbon-centered radicals are labeled according to their distance from the hydroxyl moiety in the fuel molecule, as shown in Fig. 3.1. As expected at the relatively low temperature of this analysis, H-abstraction reactions dominate over unimolecular decomposition for all four isomers. It is also expected that *n*-, *s*-, and *i*-butanol react primarily to their respective α -hydroxybutyl radicals, since the α C-H bond has the lowest energy [119]. Due to its unique structure, *t*-butanol does not have an α -hydroxybutyl radical that can be formed by H-abstraction, so *t*-butanol is primarily consumed to form the β -hydroxybutyl radical, because the O-H bond energy is much higher than β C-H bond energies.

The unique structure of *t*-butanol continues to affect the second level of reactions as well. In the temperature and pressure regime investigated, *t*-butanol tends to add to molecular oxygen at the carbon radical site, forming a hydroxybutylperoxy (RO_2) species. That this pathway is dominant is due to the fact that *t*-butanol has no α -hydroxybutyl radical. For the other three butanol isomers that do have an α -hydroxybutyl radical, the second level of reactions primarily produces an aldehyde + HO_2 by direct reaction—no hydroxybutylperoxy adduct is formed in this reaction, and there is no possibility for typical hydrocarbon low-temperature chain branching. Therefore, it is hypothesized

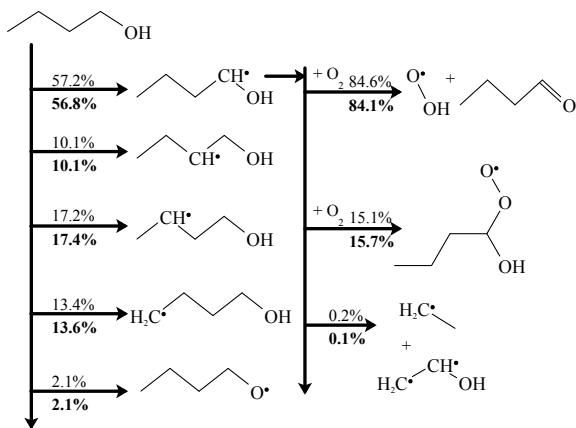


Figure 3.14: Pathway analysis for simulations of *n*-butanol at temperature of 750 K, in stoichiometric air, using the mechanism of Sarathy et al. [119]. Percentages in normal text represent an initial condition of 15 bar; bold text is for 30 bar.

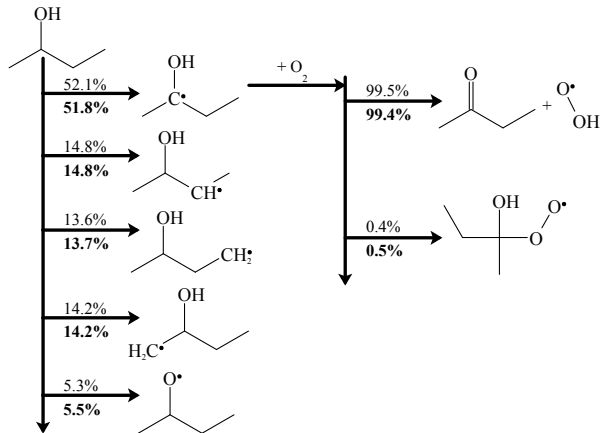


Figure 3.15: Pathway analysis for simulations of *s*-butanol at temperature of 750 K, in stoichiometric air, using the mechanism of Sarathy et al. [119]. Percentages in normal text represent an initial condition of 15 bar; bold text is for 30 bar.

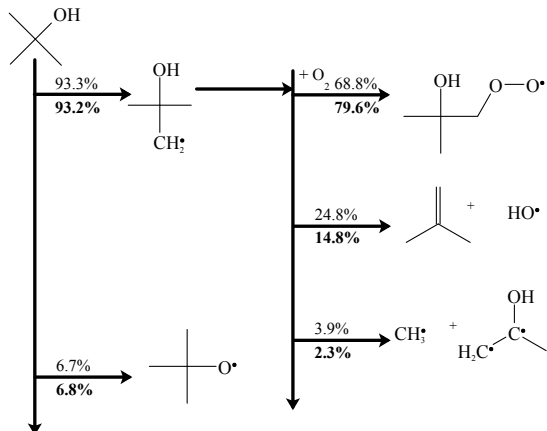


Figure 3.16: Pathway analysis for simulations of *t*-butanol at temperature of 750 K, in stoichiometric air, using the mechanism of Sarathy et al. [119]. Percentages in normal text represent an initial condition of 15 bar; bold text is for 30 bar.

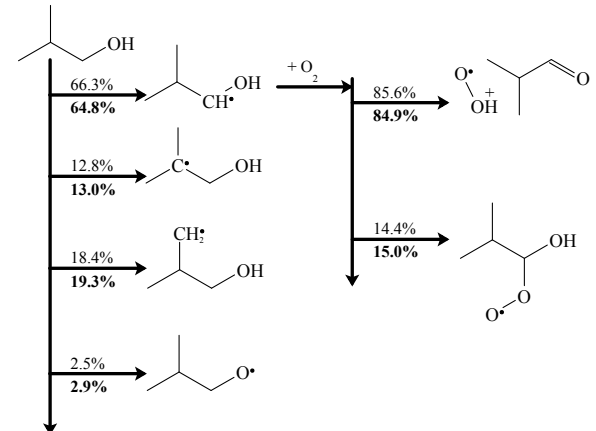


Figure 3.17: Pathway analysis for simulations of *i*-butanol at temperature of 750 K, in stoichiometric air, using the mechanism of Sarathy et al. [119]. Percentages in normal text represent an initial condition of 15 bar; bold text is for 30 bar.

that the pre-ignition heat release seen in *t*-butanol is caused by the oxygen addition to the fuel radical to form β -hydroxybutylperoxy, which is an exothermic reaction.

Figure 3.18 shows the total cumulative heat release of each isomer and the cumulative heat release of an important reaction for each of the isomers (inset), from a CONV simulation with initial conditions of 750 K and 30 bar; analysis of 15 bar results is substantially similar. The cumulative heat release in the inset is found by integrating the heat release by each reaction with respect to time, while the reactions shown are the respective reactions that have released the most heat up to the 20% fuel consumption point for each isomer. The abscissa of the plot is the fuel conversion, in percent. This choice of x-axis allows a fair comparison of the heat release, because the ignition delays of each isomer are markedly different, so comparing the heat release with a time axis is more difficult. In Fig. 3.18, exothermicity is represented by positive quantities.

In Fig. 3.18, it is clear that *t*-butanol has higher heat release at low fuel consumption (during the induction period) than the other three isomers. In addition, the primary heat release reaction for *t*-butanol has created much more heat than the primary reactions of the other three isomers. As the reactions proceed, and the temperature increases, the reverse reaction in the *t*-butanol case becomes more important, and the heat release contribution of this oxygen-addition reaction levels off. The dominance of this reaction at early times is unique to *t*-butanol ignition, and appears to be driving the pre-ignition heat release.

Other researchers have also undertaken studies of the low to intermediate temperature combustion of *t*-butanol. Lefkowitz et al. [39] performed a study in the Variable Pressure Flow Reactor (VPFR) at Princeton University on the oxidation of *t*-butanol over the temperature range from 680–950 K, at 12.5 atm and stoichiometric mixture conditions. It is interesting to note that they found no evidence of traditional hydrocarbon low temperature chemistry. They did, however, find significant quantities of acetone, peaking at approximately 800 K. Lefkowitz et al. [39] concluded that the primary pathways of acetone formation are tautomerization of propen-2-ol and β -scission of the alkoxy radical, based on an analysis of the mechanism from Grana et al. [35]. Both of these pathways are dependent on unimolecular decomposition of the hydroxybutyl radicals. However,

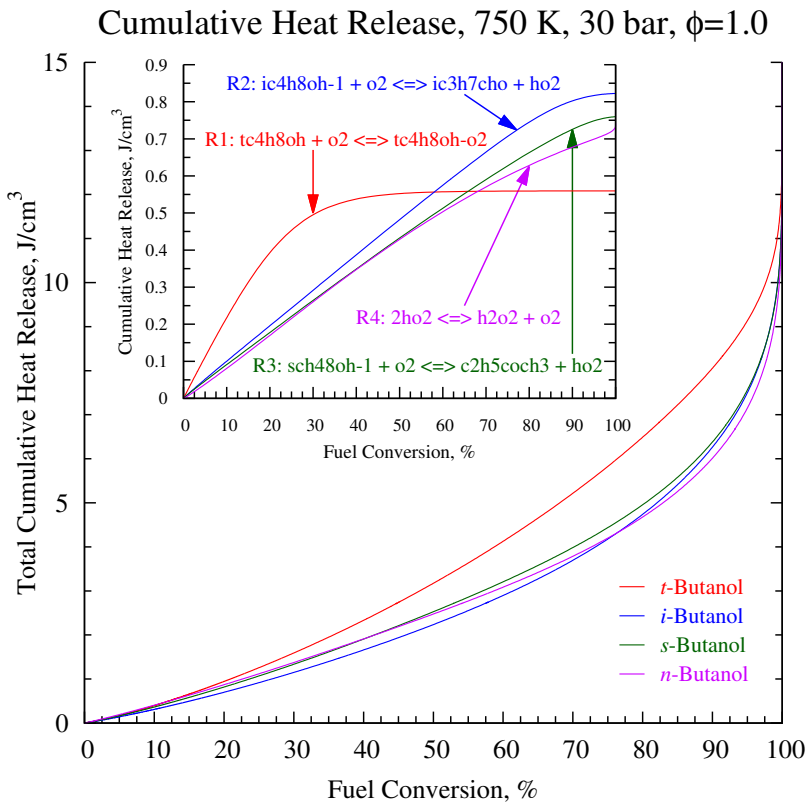


Figure 3.18: Total cumulative heat release and cumulative heat release by important reactions (inset) as a function of fuel consumption from a simulation using the mechanism of Sarathy et al. [119] with initial conditions of 750 K and 30 bar, in stoichiometric air. See Fig. 3.19 for definitions of reactions in the inset.

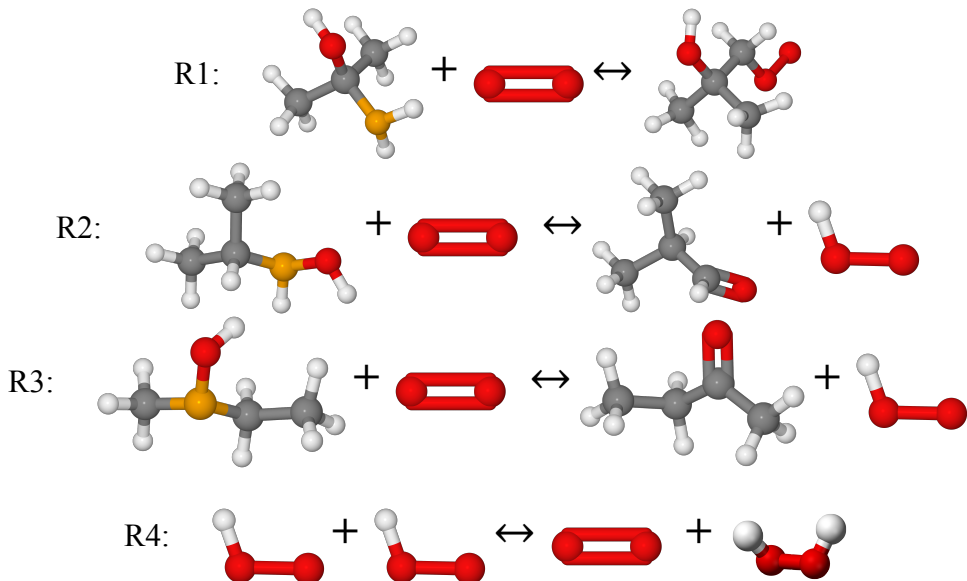


Figure 3.19: Reactions causing the most heat release in the ignition of the butanol isomers. The reaction number refers to Fig. 3.18.

this mechanism has only been validated for flame studies; indeed, an updated version of this model (by Frassoldati et al. [121]) is unable to predict the low-temperature ignition delays measured in this study and hence is not considered for analysis.

In contrast to the study of Lefkowitz et al. [39] path analysis of the mechanism by Sarathy et al. [119] shows that unimolecular decomposition of the hydroxybutyl radicals is not the most important pathway; as mentioned earlier, the most important pathway is the formation of β -hydroxybutylperoxy. Further analysis shows that the primary pathway of reaction of the *t*-butanol β -hydroxybutylperoxy species is through the Waddington mechanism. The Waddington mechanism has been shown experimentally to be an important pathway for β -hydroxypentylperoxy radicals in the low temperature combustion of *i*-pentanol [76], as well as the β -hydroxybutylperoxy radicals of *i*- and *t*-butanol [122]. *t*-Butanol only produces β -hydroxybutyl radicals, and one of the products of the Waddington pathway in *t*-butanol is acetone (the others are formaldehyde and hydroxyl radical); over 88% of the acetone produced up to the 20% fuel consumption point is produced by the Waddington reaction. The study in the VPFR thus provides further evidence of the importance of low-temperature hydroxybutylperoxy chemistry in *t*-butanol, although it is not traditional hydrocarbon low-temperature chemistry.

Up to this point, the discussion has focused mainly on the importance of hydroxybutylperoxy chemistry in *t*-butanol. Nevertheless, the chemistry of the hydroxybutylperoxy species is important in the combustion of the other isomers of butanol as well. Using the high pressure shock tube at RWTH Aachen University, Vranckx et al. [62] showed the importance of peroxy chemistry pathways in the autoignition of *n*-butanol. By adding a lumped peroxy model to an existing kinetic model for *n*-butanol combustion, they were able to substantially improve agreement of the model with their experiments at high pressure and low temperature. In their mechanism, Sarathy et al. [119] included a semi-detailed peroxy chemistry model for all the isomers of butanol. In fact, one of the main differences between the mechanism from Sarathy et al. [119] and the MIT mechanism [34, 120] is their respective treatment of the peroxy mechanism. Specifically, oxygen-addition chemistry is not included in the MIT mechanism for *i*-butanol [34, 120]. In addition, the radical

that primarily controls *i*-butanol decomposition is hydroxyl (OH) in the mechanism of Sarathy et al. [119] (generated by the peroxy chemistry sub-mechanism), but is hydroperoxyl (HO₂) in the MIT mechanism [34, 120] (generated from the direct α -hydroxybutyl + O₂=HO₂ + aldehyde formation pathway).

In their work, Sarathy et al. [119] used the reaction rates computed by Silva et al. [123] for the hydroxyethyl system (i.e. ethanol as the parent fuel) to determine the rate of direct reaction of α -hydroxybutyl and oxygen to form aldehyde and HO₂, and then set the rate of oxygen addition to the α -hydroxybutyl radical (to form α -hydroxybutylperoxy) so that the total rate was less than the collisional limit. The rates of oxygen addition for the other radicals were prescribed depending on the type of carbon (primary, secondary, or tertiary) based on studies of butane and *i*-octane [119]. Based on the well-known importance of hydroxyl in driving the reactivity of combustion systems, and the sources of the estimates for the reaction rates of oxygen addition to hydroxybutyl (i.e. the entry to the pathway that controls the rate of hydroxyl formation), it can be hypothesized that the rates of hydroxybutylperoxy formation are overestimated in the mechanism of Sarathy et al. [119], as the simulated results under-predict the experimental data of *i*-butanol.

This hypothesis is supported by the results shown in Fig. 3.20, which shows the linear brute force sensitivity of the ignition delay (τ) of *i*-butanol to changes in the A-factor of the rate coefficient, using the mechanism from Sarathy et al. [119]. The percent sensitivity is defined as the difference between the ignition delay when the A-factor of each reaction is halved and the nominal ignition delay, normalized by the nominal ignition delay, as shown below:

$$S_i = \frac{\tau(0.5A_i) - \tau(A_i)}{\tau(A_i)} \times 100\% \quad (3.1)$$

Therefore, negative sensitivity means that halving the A-factor of a reaction decreases the ignition delay, and positive sensitivity indicates the ignition delay increases. These results are for CONV simulations with initial conditions of 750 K and 30 bar as well as 1200 K and 30 bar.

The most sensitive reaction at the lower temperature is the initiation reaction of the fuel with hydroperoxyl radical to form the primary fuel radical and the second most sensitive reaction is the

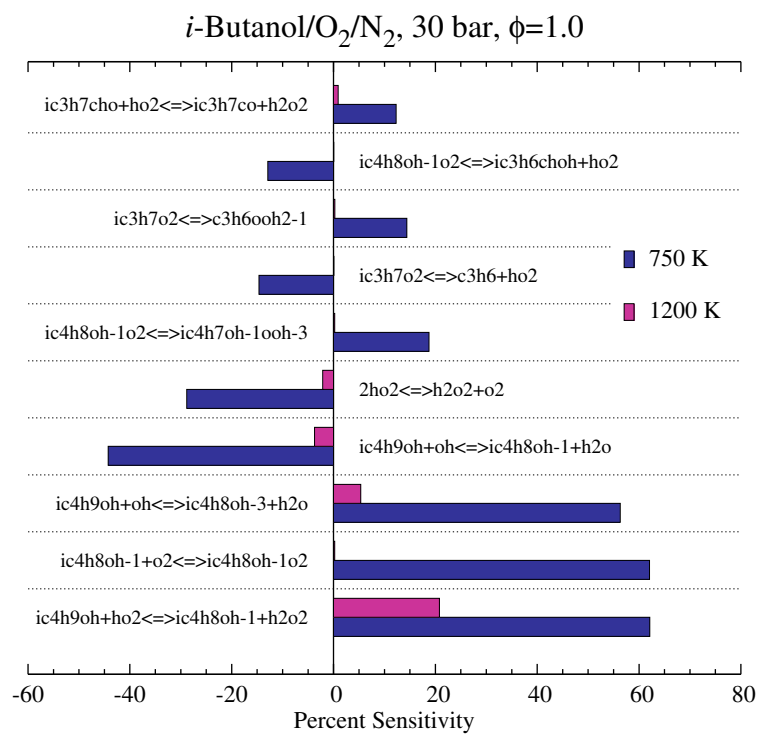


Figure 3.20: Linear brute force sensitivity analysis of the ignition delay with respect to the A-factors of the listed reactions in the mechanism from Sarathy et al. [119]. Positive quantities indicate the ignition delay is increased when the A-factor is halved.

addition of oxygen to the primary radical. Both of these reactions have positive sensitivities, indicating that reducing the rate of these reactions would increase the ignition delay (increasing the computed ignition delay will improve the agreement of the simulations relative to the experiments in this case). It is apparent, then, that reducing the amount of fuel propagating into the low temperature chain branching pathway of oxygen addition to the primary α -radical improves the simulated results. Interestingly, the *i*-butanol system is not sensitive to the rates of oxygen addition to the hydroxybutyl radicals other than the α -radical. At the higher temperature of 1200 K, there is little sensitivity on the ignition delay by changing the rate of the oxygen-addition reaction, demonstrating its lack of influence at higher temperatures.

As a final comparison, we have modified this pathway in the mechanism from Sarathy et al. [119] so that the rate of oxygen addition to the primary fuel radical is arbitrarily set to zero; that is, the rate of the reaction $\text{ic4h8oh-1} + \text{o}_2 = \text{ic4h8oh-1o}_2$ is set to zero by zeroing the A-factor, while the rates of the other oxygen addition reactions were unchanged. This unphysical situation substantially changes the results of simulations for *i*-butanol — removing this pathway in the mechanism from Sarathy et al. [119] brings the simulations into close agreement with the ignition delay results from the MIT mechanism [34, 120], which does not consider this reaction for *i*-butanol. Since the other oxygen addition reactions were unchanged, it is apparent that the addition of oxygen to α -hydroxybutyl is one of the controlling reactions for the high-pressure, low-temperature ignition of *i*-butanol using the mechanism of Sarathy et al. [119]. It is therefore concluded that a detailed examination of the rates of direct formation of aldehyde+ HO_2 and oxygen addition to the α -hydroxybutyl radical are required to better predict the low-temperature ignition behavior of *i*-butanol. Furthermore, based on the other results of this study, a detailed analysis of the oxygen addition reactions to all the isomers of butanol is probably warranted.

3.6 Conclusions

In this work, ignition delays for all four isomers of butanol in stoichiometric mixture with air have been presented over the low to intermediate temperature range, and at two compressed pressures of 15 and 30 bar. The order of reactivity of the isomers goes *n*-butanol>*s*-butanol≈*i*-butanol>*t*-butanol at the lower pressure, but changes to *n*-butanol>*t*-butanol>*s*-butanol>*i*-butanol at the higher pressure. This unexpected result is partially explained by the fact that there is substantial pre-ignition heat release present for *t*-butanol. To help understand the nature of the pre-ignition heat release of *t*-butanol, studies at off-stoichiometric conditions, $\phi = 0.5$ and $\phi = 2.0$ in air, are also conducted.

Comparisons of the experimentally measured ignition delays with two kinetic mechanisms show good agreement for certain isomers, but relatively poorer agreement for others. The kinetic mechanism of Sarathy et al. [119] is used to further elucidate the chemical processes controlling the autoignition of these butanol isomers. Pathway analysis of the fuel decomposition shows that *n*-, *s*-, and *i*-butanol primarily form α -hydroxybutyl radicals, because the proximity of the α carbon to the hydroxyl group reduces the C-H bond energy. The α -hydroxybutyl radicals tend to form an aldehyde plus HO₂ directly, without forming a hydroxybutylperoxy complex. However, due to its unique structure, *t*-butanol can only form β -radicals; these radicals do not have the tendency to react with oxygen to directly form HO₂ and an aldehyde. Rather, *t*-butanol preferentially adds oxygen to the fuel radical site. It is hypothesized that this reaction, O₂ addition to form hydroxybutylperoxy, causes the pre-ignition heat release in *t*-butanol and leads to a chain propagation pathway through the Waddington mechanism. The fact that this oxygen-addition reaction is preferred is unique to *t*-butanol, although a detailed understanding of the peroxy chemistry of alcohols is still of vital importance to the other butanol isomers. This is further demonstrated in this work for the case of *i*-butanol, where the ignition delay is shown to be quite sensitive to both the rate of primary fuel radical formation and to the rate of oxygen addition to the primary fuel radical. It is also noted that *n*-butanol autoignition was shown to be quite sensitive to peroxy chemistry in the study of Vranckx et al. [62].

All together, these analyses show the importance of the peroxy chemistry pathways in the autoignition of the butanols. Further experimental studies, such as species profiles from the low temperature ignition of the butanol isomers, could help reduce uncertainty in the pathways of fuel breakdown. Finally, further understanding of the rates of the peroxy pathways is important and therefore further theoretical and quantum chemical studies are warranted.

Chapter 4

i-Pentanol

Table 4.1: HHV of Ethanol, *i*-Pentanol, and Gasoline

Compound	Ethanol [21]	<i>i</i> -Pentanol [21]	Gasoline [22]
HHV [MJ/kg]	29.67	37.73	48.46

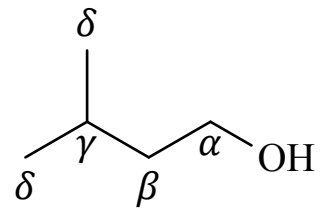


Figure 4.1: Skeletal structure of *i*-pentanol

4.1 Structure of *i*-Pentanol

i-Pentanol (3-methyl-1-butanol) is a five-carbon alcohol whose skeletal structure is shown in Fig. 4.1. The carbon atoms in Fig. 4.1 are labeled according to their distance from the hydroxyl moiety, with α being the closest and δ being the farthest. The Greek letter notation will be used to refer to the carbon-centered radicals in Sec. 4.5. *i*-Pentanol can be produced biologically [20], and offers several similar advantages as the butanol isomers as compared to ethanol. Table 4.1 compares the HHV of ethanol, *i*-pentanol, and gasoline.

Table 4.2: *i*-pentanol Experimental Conditions

Reactant (Purity)			Equivalence Ratio ϕ	Compressed Pressure P_C (bar)
<i>i</i> -pentanol (99.6%)	O ₂ (99.994%)	N ₂ (99.999%)		
Mole Percentage				
2.41	20.50	77.09	1.0	40
1.22	20.75	78.03	0.5	40
4.71	20.01	75.27	2.0	40

4.2 Procedures

Experiments for *i*-pentanol in the RCM have been performed at the conditions listed in Table 4.2. Homogeneous fuel and air pre-mixtures are prepared in an approximately 17 L mixing tank. The mixing tank and all tubes and manifolds connecting the tank with the RCM are heated, allowing the study of relatively low vapor pressure fuels. The initial temperature is set above the saturation temperature of *i*-pentanol for each mixture studied. The mixing tank is equipped with a magnetic stirrer to ensure complete homogeneity of the mixture.

Prior to mixture preparation, the mixing tank is vacuumed to less than 1 Torr, whereupon liquid fuel (*i*-pentanol, Sigma-Aldrich, 99.6% purity) is injected by a syringe through a septum. The syringe is massed before and after the injection, with the difference being the amount of fuel in the mixing tank. Based on this mass, required proportions of the gaseous oxidizer (O₂, 99.994% purity, N₂, 99.999% purity) are calculated. The gases are added to the mixing tank sequentially at room temperature and the total pressure is monitored to ensure the proper mixture concentrations are attained. Finally, the heaters and stirring vane are switched on and the system is allowed approximately 1.5 h to reach steady state.

4.3 Model Improvements

Through collaboration with researchers at Lawrence Livermore National Laboratory, many improvements to the chemical kinetic model for *i*-pentanol were made relative to the work of Tsujimura et al. [77]. Some of the major improvements are highlighted below; see the article for more detail [75].

1. The model was restructured based on work with C₄ and C₅ alcohols [119, 124]
2. The most stable conformers of *i*-pentanol were calculated using quantum chemistry software
3. The BDEs of the C-C, C-H, C-O, and O-H bonds were calculated using quantum chemistry software
4. The model includes the Waddington pathway shown to be important in low-temperature decomposition of *i*-pentanol by Welz et al. [76]
5. New reaction pathways were added based on the work of Welz et al. [76, 125], including the unconventional water-elimination pathway discussed in Welz et al. [125]

Moreover, the following data sets from the literature and presented in [75] were used to validate the newly updated model, in addition to the new data at $P_C = 40$ bar presented here.

1. Ignition delays measured in a shock tube and RCM[77, 78]
2. JSR species data [73]
3. New ignition delays measured in shock tubes [75]
4. New JSR species data [75]
5. New flame speed and flame extinction measurements [75]

4.4 Experimental & Modeling Results

The experimental ignition delays measured in the RCM are shown in Figs. 4.2, 4.3, and 4.4, along with ignition delays measured in the shock tube and comparison with the model simulations. There is no $\phi = 2.0$ data set for 7 atm because no conditions at which ignition occurred could be found. In Figs. 4.2–4.4, solid lines represent adiabatic, constant volume simulations, and dashed lines represent volume-profile simulations.

At 7 atm (Fig. 4.2), the high-temperature ignition delays measured in the shock tube are generally predicted to within a factor of 1.5. The RCM experiments are also well predicted at low temperature—within a factor of 2—but the disagreement grows to approximately a factor of 4 in the intermediate temperature regime. At 20 atm (Fig. 4.3), the high-temperature ignition delays are well predicted, including capturing the equivalence ratio sensitivity of the ignition delays. The ignition delays measured in the RCM are fairly well predicted at the lean and stoichiometric condition, but are over-predicted at the rich condition.

At 40 atm (Fig. 4.4), the model is able to reproduce the high-temperature ignition delays fairly well, including capturing the equivalence ratio dependence of the ignition delays. Ignition delay data near 40 atm and temperatures ranging from 651–776 K were also acquired using the RCM. The ignition data in the RCM and ST are in good qualitative agreement, displaying the expected decrease in ignition delay with increasing temperature. The model well predicts the observed trend of decreasing ignition delay time with increasing equivalence ratio, which occurs because a higher fuel concentration results in greater radical production at these conditions. Constant volume and volume history simulations at the 40 atm RCM conditions (Fig. 4.4) indicate the model can well predict ignition delay times at stoichiometric conditions, but cannot well predict RCM ignition delay data at lean and rich conditions. The difference (i.e., spread) in ignition delay times across various equivalence ratios is similar to that observed for other alcohols in the same facilities (e.g., *n*-butanol at 15 bar [64] and *t*-butanol at 30 bar [65]). The primary issue with the model is its equivalence ratio sensitivity; predicted ignition delay times need to be increased at lean conditions yet

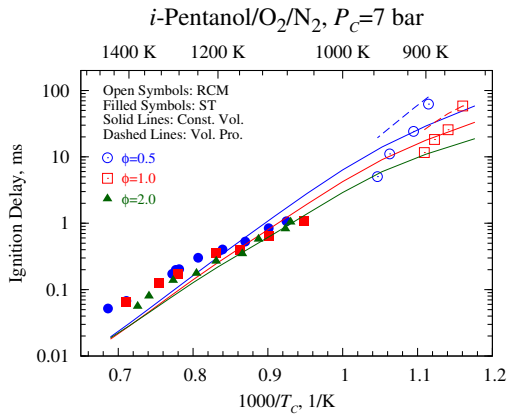


Figure 4.2: Shock tube and RCM ignition delay times from Tsujimura et al. [77] at 7 atm compared with model predictions by the model from Sarathy et al. [75].

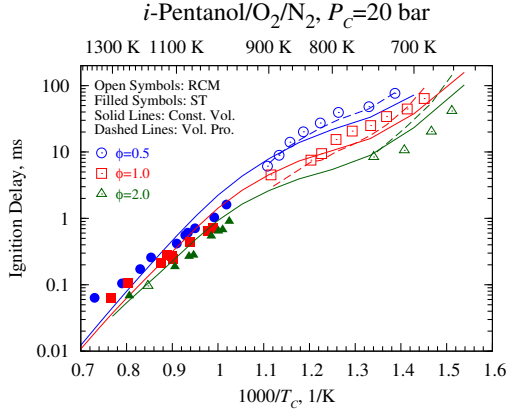


Figure 4.3: Shock tube and RCM ignition delay times from Tsujimura et al. [77] at 20 atm compared with model predictions by the model from Sarathy et al. [75].

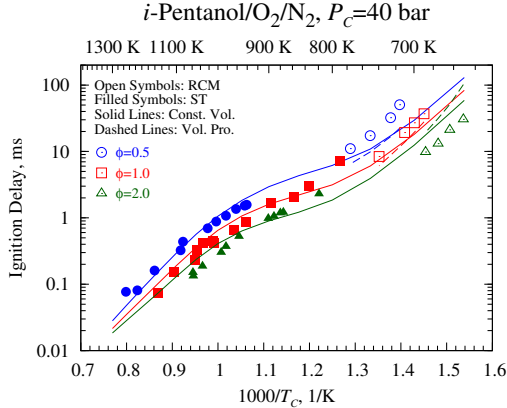


Figure 4.4: Shock tube and RCM ignition delay times from Sarathy et al. [75] at 40 atm compared with model predictions by the model from Sarathy et al. [75].

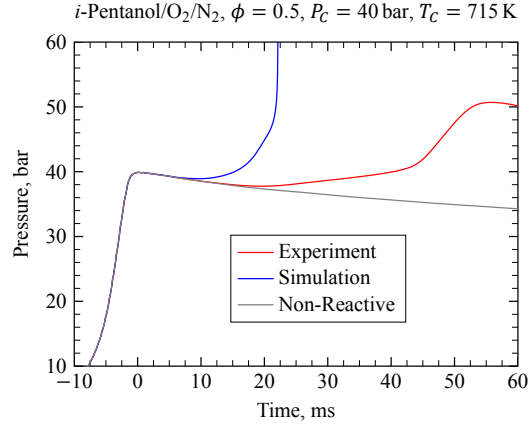


Figure 4.5: Experimental reactive (red), simulated reactive (blue), and experimental non-reactive (gray) pressure profiles at 40 atm for lean *i*-pentanol/air mixtures.

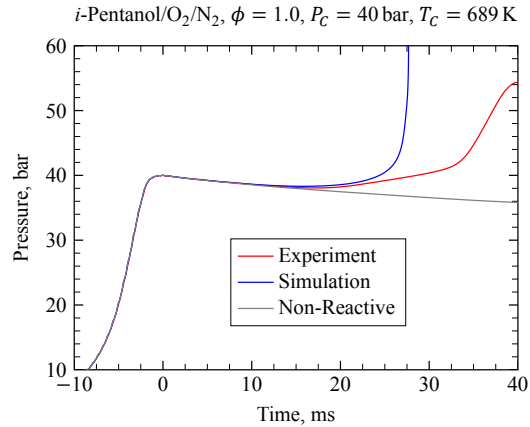


Figure 4.6: Experimental reactive (red), simulated reactive (blue), and experimental non-reactive (gray) pressure profiles at 40 atm for stoichiometric *i*-pentanol/air mixtures.

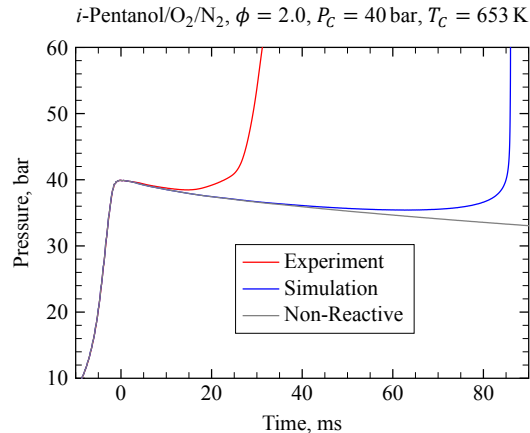


Figure 4.7: Experimental reactive (red), simulated reactive (blue), and experimental non-reactive (gray) pressure profiles at 40 atm for rich *i*-pentanol/air mixtures.

decreased at rich conditions, implying that the system's reactivity is controlled by different phenomenon at different equivalence ratios. At these low temperatures the model's reactivity is driven by the overall peroxy reaction sequence, $R+O_2=ROO=QOOH(+O_2)=OOQOOH=2OH+products$, including the inhibitive direct (i.e., concerted) HO_2 elimination and $QOOH$ decomposition routes. An increase (or decrease) in any reaction rate constant along this reaction sequence will move the reactivity of the system in the same direction at all equivalence ratios. Therefore, we were unable to identify a single reaction rate constant modification that would decrease overall reactivity at lean conditions while increase it at rich conditions.

Representative experimental and simulated pressure profiles for the lean, stoichiometric, and rich conditions are shown in Figs. 4.5, 4.6, and 4.7 respectively, with the profiles shifted so TDC occurs at 0 s. Interestingly, the experimental pressure traces after the induction period do not show a sharp increase in pressure (i.e., heat release is more gradual, similar to two-stage ignition). For the lean case, there is a moderate heat release 25 ms after TDC followed by a larger heat release event, and similar behavior is observed at other equivalence ratios. It is noted that similar heat release prior to the main ignition event was found in an HCCI engine experiment using *i*-pentanol by Yang et al. [81] and was termed Intermediate Temperature Heat Release (ITHR) in their work.

The pressure profile of the present simulations qualitatively agrees with the experimental data, in that the simulated pressure traces deviate from the non-reactive trace prior to the main ignition event, although the ignition delay itself does not necessarily agree very well. For lean and stoichiometric cases the simulated ignition delay times are fast compared to the data, whereas at rich conditions they are too slow.

4.5 Discussion

The sensitivity of the ignition delay to changes in the reaction rate coefficients is shown in Fig. 4.8 for a constant volume, adiabatic simulation at 20 atm, 800 K, and for equivalence ratios varying

from $\phi = 0.5\text{--}2.0$. The percent sensitivity is computed by the formula

$$S = \frac{\tau(2k_i) - \tau(k_i)}{\tau(k_i)} \times 100 \% \quad (4.1)$$

where $\tau(2k_i)$ is the ignition delay when the rate coefficient of reaction i is doubled, and $\tau(k_i)$ is the nominal ignition delay. Positive sensitivities therefore represent an increase in the ignition delay when the rate coefficient of reaction i is increased. Both the forward and reverse rates of each reaction are increased simultaneously. Since the reaction $2\text{ho}_2 \rightleftharpoons \text{h}_2\text{o}_2 + \text{o}_2$ is represented by two sets of A , b , and E_a in the reaction mechanism, both Arrhenius coefficients were simultaneously doubled to give the sensitivity value shown in Fig. 4.8.

It is seen from Fig. 4.8 that the most sensitive reaction under these conditions is H-abstraction by OH to form the α -hydroxypentyl radical (ic5h10oh-1). Increasing the rate of abstraction by OH from the α site increases the ignition delay because subsequent reaction of the fuel radical with O_2 leads to the formation of HO_2 and *i*-pentanal, which is an OH terminating pathway. The next most sensitive reaction is H-abstraction by OH to form the γ -hydroxypentyl radical (ic5h10oh-3). The ignition delay is also sensitive to the rates of isomerization of the ROO radicals formed by the other hydroxypentyl radicals. This indicates that, except for the α radical, the other hydroxypentyl radicals undergo typical low-temperature chain branching reactions. This observation is further corroborated by a reaction path analysis, discussed below. Furthermore, Fig. 4.8 shows that the ignition delay is also sensitive to some low temperature chain terminating pathways, such as formation of an enol + HO_2 from ROO or QOOH radicals.

A sensitivity analysis of the ignition delay to changes in the reaction rate coefficients for initial conditions of 40 atm and 689 K, for three equivalence ratios, is shown in Fig. 4.9. As before, positive sensitivity indicates that increasing the rate coefficient of that reaction increases the ignition delay. Similar to the 20 atm sensitivity analysis, the most sensitive reactions are the H-abstractions from the fuel and the subsequent reactions of these initial fuel radicals. However, stronger equivalence ratio dependence of the sensitivity results is seen in Fig. 4.9 as compared to Fig. 4.8. It

is interesting to note that the most sensitive reaction, formation of the α -hydroxypentyl radical through H-abstraction by OH, is nearly twice as sensitive at $\phi = 0.5$ than at $\phi = 2.0$, while most of the other reactions have nearly the same sensitivity for the three equivalence ratios.

In addition, the reaction of formaldehyde and hydroxyl radical to form formyl radical and water shows up as somewhat sensitive, especially for the lean case. The importance of this reaction is demonstrated by the path analysis shown in Fig. 4.10 (similar results are obtained for a path analysis at 40 atm as at 20 atm). Formaldehyde is a significant product in the decomposition of the β - and γ -hydroxypentyl radicals, as well as the pentoxy radical. Furthermore, the reaction of two hydroperoxyl molecules to form hydrogen peroxide and oxygen molecule is the seventh most sensitive reaction. This reaction is important as it releases the most heat during the ITHR period prior to the main ignition for all three equivalence ratios and because the rapid reaction of the α -hydroxypentyl radical to form *i*-pentanal and hydroperoxyl is important in alcohol combustion. In view of the equivalence ratio dependence shown in Fig. 4.9, these sensitivity analysis results suggest that it may be possible to adjust multiple reaction rates in the low temperature chain branching pathways to decrease reactivity at lean conditions but increase reactivity at rich conditions, which warrants further investigation.

The main *i*-pentanol reaction pathways after 20% fuel consumption at 800 K, 20 atm, and for three equivalence ratios are shown in Fig. 4.10, describing the key low temperature reaction pathways. The percent flux of each reaction path is the contribution of that path to destroying the reactant, integrated up to 20% fuel consumption. It is seen that fuel is mainly consumed by the H atom abstraction at the α site because *i*-pentanol has a weak C-H bond at the α site. As discussed previously, subsequent reactions of α -hydroxypentyl with O₂ generate *i*-pentanal + HO₂, an OH terminating pathway. The other hydroxypentyl radicals tend to add to molecular oxygen and form hydroxyalkylperoxy (ROO) radicals. These radicals are mainly isomerized to hydroxyalkylhydroperoxide (QOOH) or decomposed to enol species by the concerted elimination of HO₂. Around 18% of β -hydroxyalkylperoxy radicals are decomposed to produce *i*-butanal (2-methylpropanal), formaldehyde, and OH radical via ROO isomerization and β -scission reactions by the Waddington

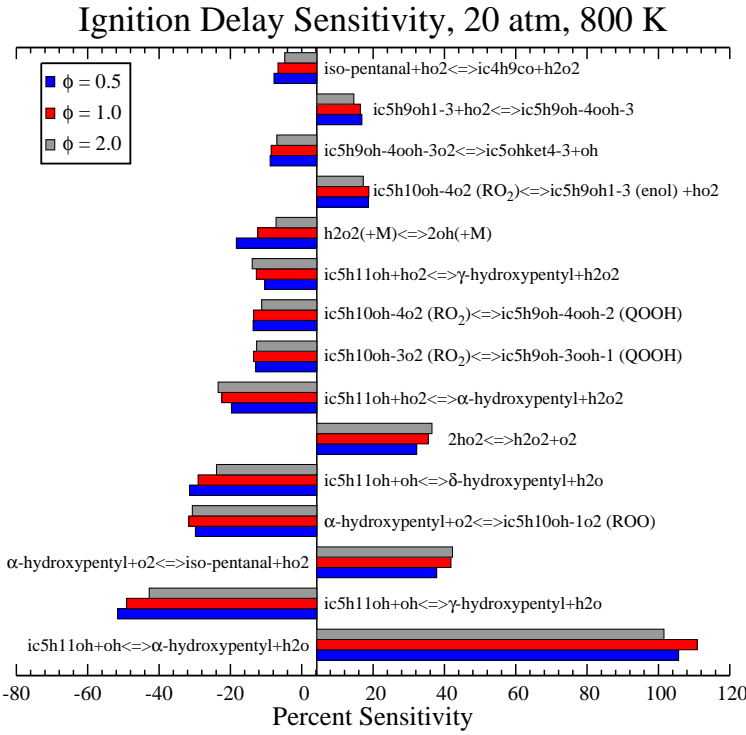


Figure 4.8: Sensitivity of the ignition delay to changes in the reaction rate coefficients for three equivalence ratios. Initial conditions for constant-volume adiabatic simulations are 800 K and 20 atm.

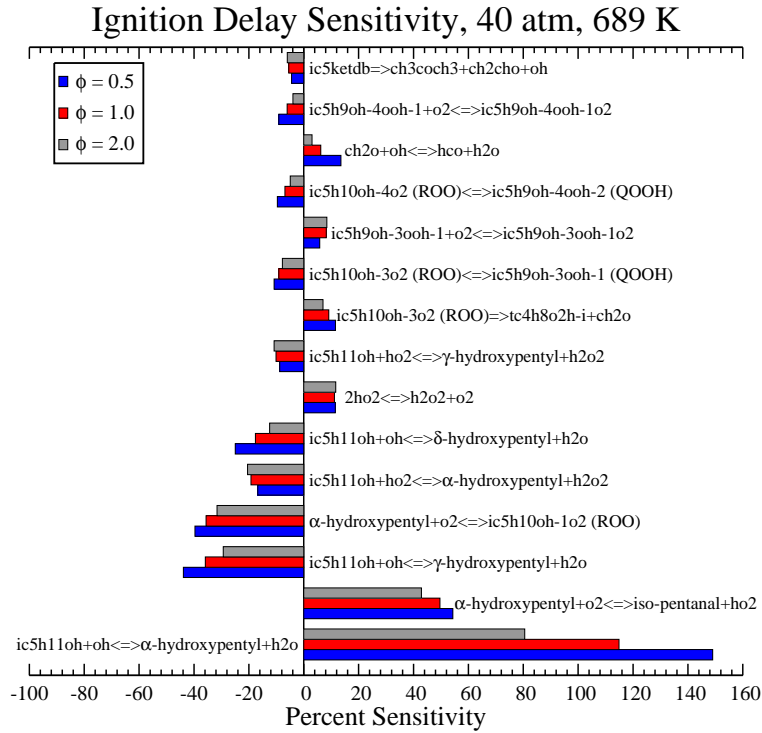


Figure 4.9: Sensitivity of the ignition delay to changes in the reaction rate coefficients for three equivalence ratios. Initial conditions for constant-volume adiabatic simulations are 689 K and 40 atm.

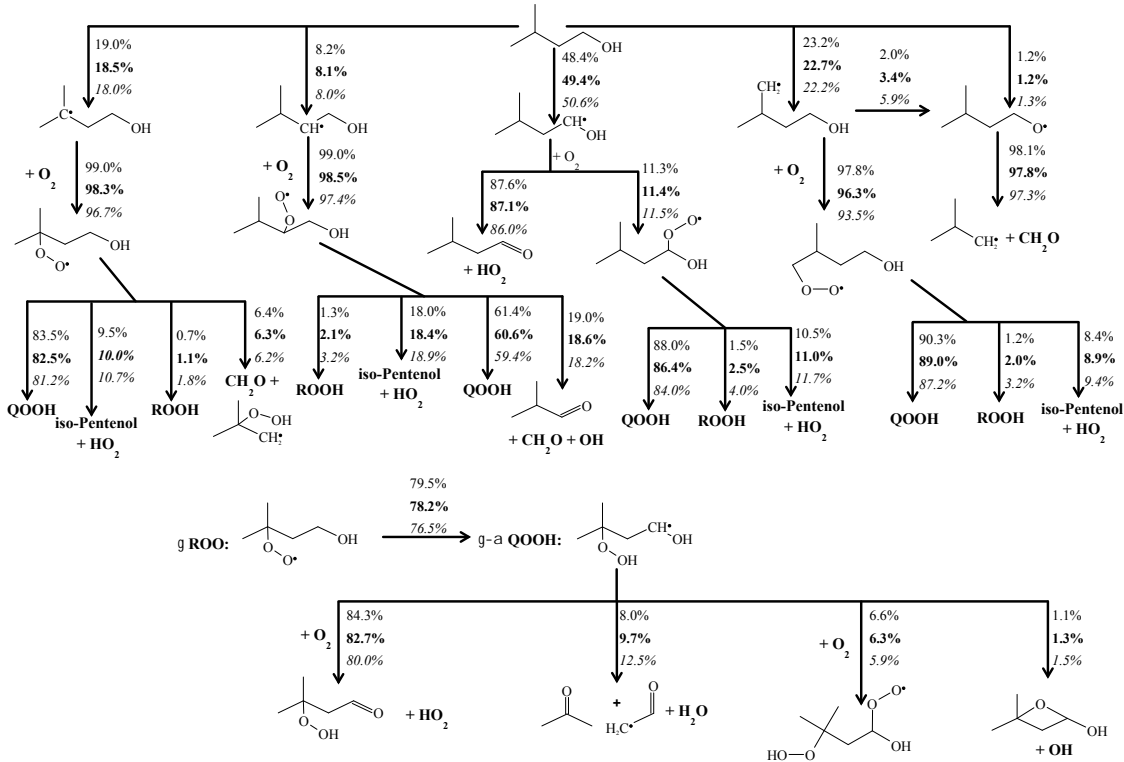


Figure 4.10: Reaction path analysis for *i*-pentanol at 800 K, 20 atm, and three equivalence ratios, based on constant-volume adiabatic simulations. Plain text: $\phi = 0.5$. Bold text: $\phi = 1.0$. Italic text: $\phi = 2.0$. The flux is integrated up to 20% fuel consumption.

mechanism [126, 127]. It is also interesting to note that a similar pathway involving hydrogen transfer from the OH group is shown to be important for the γ -ROO (6%) via a 7-membered transition state ring, which is a reaction sequence we included based on the work of Welz et al. [76].

4.6 Conclusions

New experimental ignition delay data has been collected in an RCM at conditions of 40 atm, $\phi = 0.5\text{--}2.0$, and temperatures below 800 K. The measured pressure histories showed interesting behavior of slow initial pressure rise prior to a sharp pressure rise indicating overall ignition. This pressure rise may be attributed to the role of the Waddington mechanism in consuming the fuel via the production and recycling of OH radicals during the pre-ignition phase.

An existing model [77] for *i*-pentanol combustion has been updated with newly calculated re-

action rate coefficients and newly discovered reaction pathways. The updated model was able to predict the ignition delays measured in the RCM and shock tubes fairly well, although it was unable to reproduce the equivalence ratio sensitivity of the low-temperature RCM ignition delay measurements. The model was also able to qualitatively capture the slow initial pressure rise measured during the RCM experiments, although the model was unable to reproduce the quantitative timing of the pressure rise.

Pathway and sensitivity analyses were conducted to understand the important reactions in the decomposition of *i*-pentanol. The most important path for consumption of fuel radicals at low and intermediate temperatures was the reaction of the α -hydroxypentyl radical with O₂ to form *i*-pentanal and HO₂, a path that does not contribute to the low temperature branching. However, sufficient low temperature chain branching involving the γ and δ fuel radicals occurred in the model that it was able to reasonably reproduce low-temperature ignition and reactivity observed in the experiments. Sensitivity analysis showed that no single reaction can be modified to improve agreement of the model with all of the conditions, and further experimental or computational study is required to identify the cause of the discrepancy in predictions of ignition delay at off-stoichiometric, low-temperature conditions.

Chapter 5

Methylcyclohexane

Table 5.1: Molar Proportions of Reactants in MCH Experiments

Mix #	ϕ	MCH	O ₂	N ₂	Ar
1	1.0	1	10.5	12.25	71.75
2	0.5	1	21.0	0.00	73.50
3	1.5	1	7.0	16.35	71.15

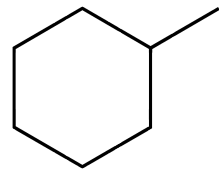


Figure 5.1: Skeletal structure of methylcyclohexane

5.1 Structure of Methylcyclohexane

Methylcyclohexane (MCH) is the simplest branched cycloalkane, and as such, represents an excellent target to use as the base for models of larger branched cycloalkanes. MCH has the elemental composition C₇H₁₄, and its skeletal structure is shown in Fig. 5.1.

5.2 Procedures

The liquid fuel (methyl-cyclohexane, 99.0% purity) is massed to a precision of 0.01 g in a syringe before being injected into the mixing tank through a septum. The proportions of oxygen (99.9999% purity), nitrogen (99.9995% purity), and argon (99.9999% purity) are determined by specifying the

oxidizer composition, the equivalence ratio, and the total mass of fuel. The gases are added to the mixing tank manometrically at room temperature.

Three different mixtures of MCH/O₂/N₂/Ar are prepared in this study, as outlined in Table 5.1. These mixtures (denoted as Mix #1–3) match the mixtures prepared in our previous work with MCH in the RCM [89]. The equivalence ratios corresponding to Mix #1–3 are $\phi = 1.0, 0.5$, and 1.5 , respectively. As in the previous RCM experiments, the mole fraction of MCH is held constant and the mole fraction of O₂ is varied to adjust the equivalence ratio. This experimental design allows these data to be used to validate chemical kinetic models for changes in O₂ concentration, which is an important variable in internal combustion engines where exhaust gas recirculation is used to reduce the oxygen concentrations to avoid NOx formation. Few validation data for ignition are available for changing oxygen concentrations. In addition, the relative proportions of O₂, N₂, and Ar are adjusted so that the same specific heat ratio is maintained in the three mixtures. The utility of this experimental design will be discussed in due course.

5.3 Model Improvements

Through collaboration with researchers at Lawrence Livermore National Laboratory, many improvements to the chemical kinetic model for MCH were made. Some of the major improvements are highlighted below; see the article for more detail [128]. It should be noted that the improvement relative to the model from 2007 by Pitz et al. [14] is substantial.

1. The base C₁–C₄ chemistry has been updated with the AramcoMech version 1.3 [9]
2. The aromatics base chemistry was updated with the latest LLNL-NUIG model [129]
3. The cyclohexane sub-model was updated with a new version from Silke et al. [130]
4. Rates of abstraction reactions from MCH have been updated with recently measured experimental values [131] and standardized according to the LLNL reaction rate rules [132]

5. Products of MCH breakdown with unsaturated rings such as methylcyclohexene were previously lumped into one species for simplicity. In the new model, they have been unlumped and provide improved fidelity in modeling these species. [133]
6. The reaction rates of some low-temperature specific reactions were updated using new quantum chemical calculations to compute the rate. Other reaction rates were updated from similar calculations performed by Fernandes et al. [134]
7. The activation energy of the ketohydroperoxide decomposition reactions was increased to bring it into closer agreement with the activation energy used by Metcalfe et al. [9]. This change has a dramatic effect on the low-temperature ignition delays, as shown in Sec. 5.5.

5.4 Experimental Results

The experimental ignition delays measured at the three equivalence ratios and compressed pressure of 50 bar are shown in Fig. 5.2. The open symbols are the overall ignition delays and the filled symbols are the first stage ignition delays. The vertical error bars on the experimental data represent twice the standard deviation of all of the experiments at that condition. Detailed uncertainty analysis of the deduced compressed temperature was conducted in Sec. 2.1.8 where the maximum uncertainty of the compressed temperature was found to be approximately $\pm 1\%$.

The negative temperature coefficient (NTC) region is an important feature of low temperature ignition where the ignition delay time increases with increasing temperature. The NTC region of the overall ignition delay is evident in Fig. 5.2 for the $\phi = 1.5$ case (Mix #3) and approximately includes the temperature range of $T_C = 775\text{--}840\text{ K}$. For $\phi = 1.5$, first stage ignition is evident for conditions in the range of $T_C = 740\text{--}800\text{ K}$.

For $\phi = 1.0$ (Mix #1), the NTC region of the overall ignition delay could not be completely resolved. Only three conditions in the low temperature region and three conditions in the high temperature region are shown in Fig. 5.2. The experimental pressure traces during the compres-

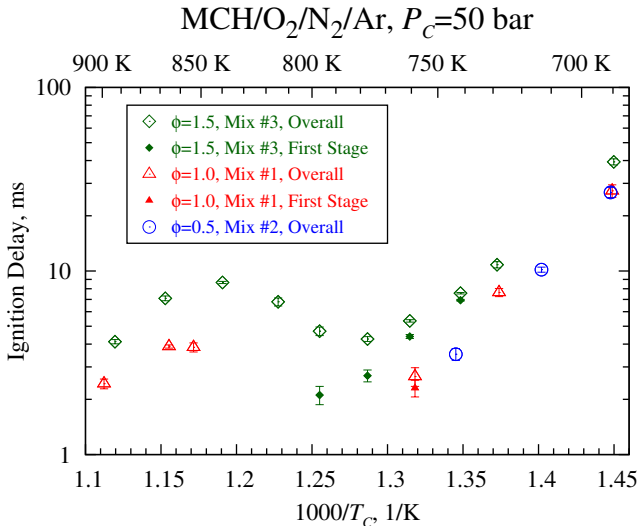


Figure 5.2: Experimentally measured ignition delays at $P_c = 50$ bar for the mixture conditions in Table 5.1

sion stroke for intermediate temperature conditions were seen to deviate from their non-reactive counterparts, demonstrating appreciable reactivity therein. Hence, those data are not included in Fig. 5.2.

For the experiments at $\phi = 0.5$ (Mix #2), only three data points in the low temperature region are reported and none of them exhibits two-stage ignition response. As the temperature is increased further, noticeable reactivity during the compression stroke is evident.

As stated earlier, the mole fraction of MCH is held constant in this study, while the mole fraction of the oxidizer is changed to modify the equivalence ratio. Figure 5.2 demonstrates that the $\phi = 0.5$ case is the most reactive (as judged by the inverse of the ignition delay) and the $\phi = 1.5$ case is the least reactive. As has been shown for other fuels, including *n*-butanol [64] and Jet-A [101], decreasing the equivalence ratio by increasing the oxygen mole fraction but holding the fuel mole fraction constant increases the reactivity.

5.5 Comparison to Model

A comparison of the experimentally measured first stage ignition delays (open symbols) and the first stage ignition delays computed using the updated model (lines) is shown in Figs. 5.3a, 5.4a,

and 5.5a for Mix #1, #2, and #3, respectively. In addition, a comparison of the experimentally measured overall ignition delays (open symbols) and the overall ignition delay computed by the updated model (lines) is shown in Figs. 5.3b, 5.4b, and 5.5b. The experiments include the new work being presented here at $P_C = 50$ bar in addition to the previous RCM experiments at $P_C = 15.1$ and 25.5 bar [89]. The simulations are the VPRO type of simulations. For some computational cases, substantial heat release during the compression stroke caused the computed pressure to depart from the non-reactive profile prior to EOC. Therefore, these cases are not shown in Figs. 5.3–5.5. For these conditions, the experimental pressure trace did not exhibit significant heat release during the compression stroke and the experimental pressure at EOC for the reactive case matched that of the non-reactive counterpart.

At 15.1 and 25.5 bar for Mix #1 and #2, the overall ignition delay is very well predicted for temperatures above approximately 715 K. For lower temperatures at these two equivalence ratios, the experimental ignition delays are under-predicted by the model, but the predictions are nevertheless within a factor of two of the data. For the rich case (Mix #3), the simulations under-predict the ignition delay over a wider temperature range but the results improve as temperature increases. Again, the experimental ignition delays are predicted to within approximately a factor of two. At 50 bar, the ignition delays are under-predicted for all of the equivalence ratios studied here, but the agreement is within a factor of two.

The first stage ignition delays for all of the pressure and equivalence ratios are under-predicted, but are within a factor of three of the experimental values. Furthermore, for all of the equivalence ratios tested at $P_C = 50$ bar, it is of interest to note that there are several cases where simulated ignition delays show two-stage response where the experiment shows only a single stage ignition. Nevertheless, the present mechanism is a marked improvement from the comparison performed by Mittal and Sung [89] who found that the ignition delays were strongly and uniformly over-predicted by the previous LLNL mechanism by Pitz et al. [14].

Figure 5.6 shows a comparison of selected simulated and experimentally measured pressure traces for Mix #1, #2, and #3, respectively, at $P_C = 50$ bar. Also shown in Fig. 5.6 is the simulated

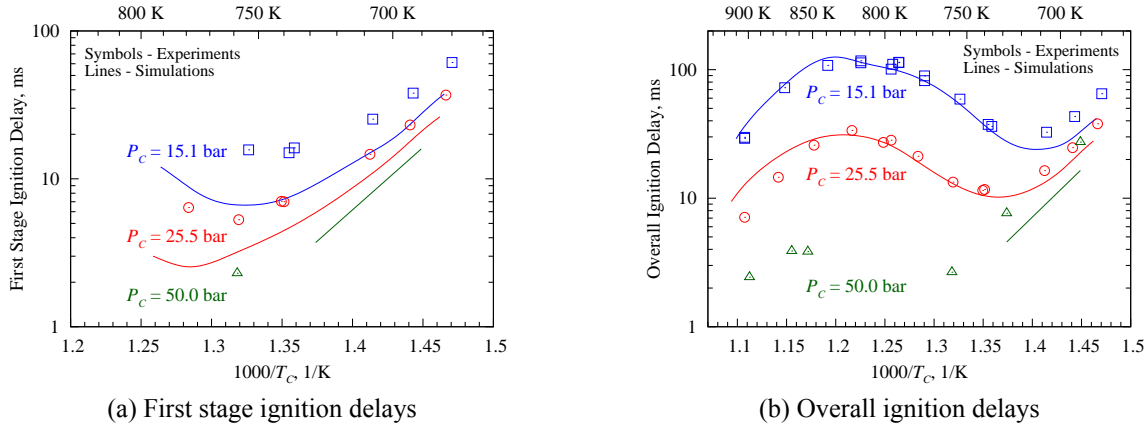


Figure 5.3: Comparison of experimental and simulated ignition delays for three pressures for Mix #1. The data at 15.1 and 25.5 bar are from the study of Mittal and Sung [89].

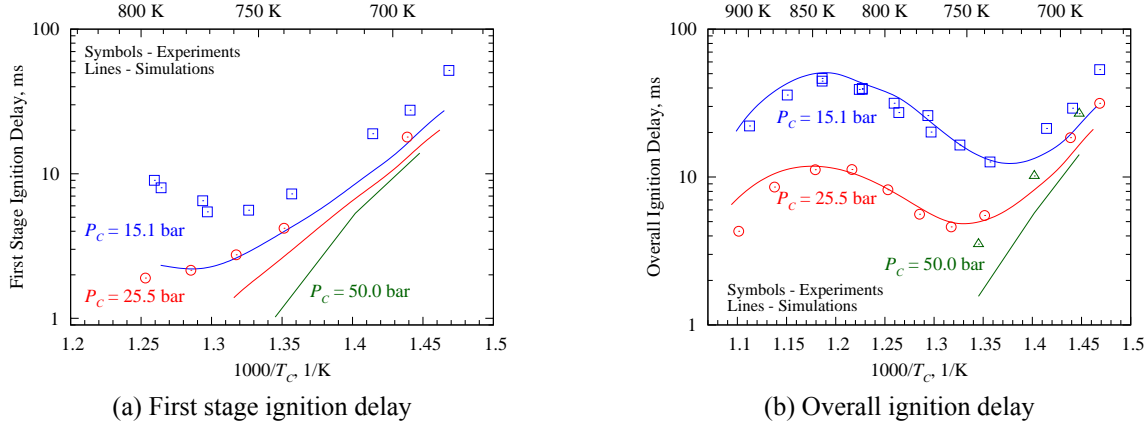


Figure 5.4: Comparison of experimental and simulated ignition delays for three pressures for Mix #2. The data at 15.1 and 25.5 bar are from the study of Mittal and Sung [89].

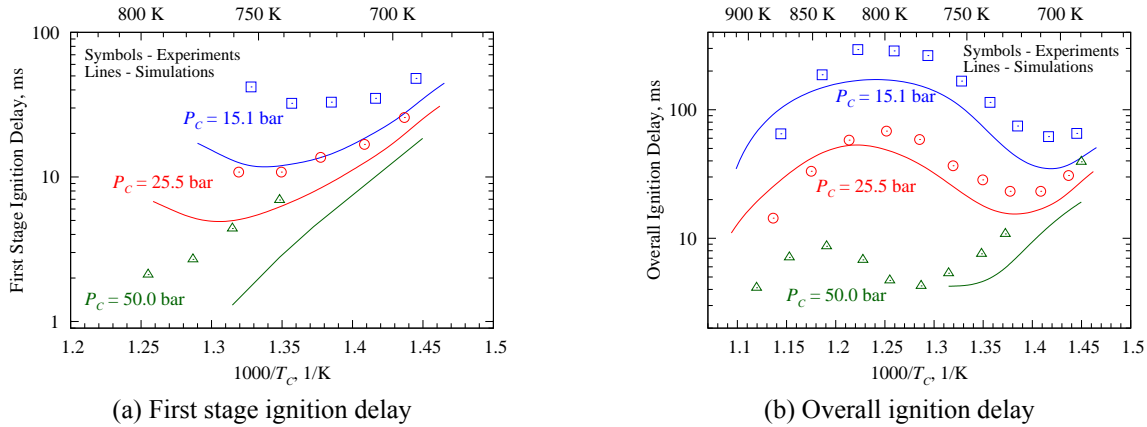


Figure 5.5: Comparison of experimental and simulated ignition delays for three pressures for Mix #3. The data at 15.1 and 25.5 bar are from the study of Mittal and Sung [89].

non-reactive pressure trace corresponding to each experimental condition. Small differences in the heat loss profile for different temperatures are apparent in the non-reactive pressure traces. These differences arise from the changing surface area to volume ratio of the reaction chamber at the end of compression as the compression ratio is changed to vary the compressed temperature. This highlights the importance of using VPRO simulations to compare predictions of ignition delay with the experimental data.

For Mix #1, it is clear that the simulated reactive pressure trace in Fig. 5.6a at $T_C = 866$ K (red dashed line) deviates from the non-reactive pressure trace (red dot-dot-dashed line) prior to the end of compression. The same is also true of the 797 K case shown for Mix #3 in Fig. 5.6c. Remarkably, the simulated case for Mix #1 at $T_C = 866$ K predicts the overall ignition delay quite well. However, due to the heat release prior to EOC, this simulated result is not plotted in Fig. 5.3. The simulated case for Mix #3 at $T_C = 797$ K is also not plotted on Fig. 5.5 due to the heat release prior to EOC; interestingly, this case under-predicts the first stage ignition delay but over-predicts the overall ignition delay. For the other simulated cases (black lines), the reactive pressure traces closely follow their non-reactive counterparts until the ignition event begins. The experimental ignition delays of these cases are under-predicted by the model. It is also seen in Fig. 5.6c for $T_C = 729$ K that the model predicts two-stage ignition, although two-stage ignition is not observed experimentally.

The current mechanism is also compared to shock tube ignition delays from the studies of Vasu et al. [83] and Vanderover and Oehlschlaeger [84]. Those studies considered the autoignition of stoichiometric mixtures of MCH with O₂/N₂ air. The comparison is shown in Fig. 5.7 for the near 50 atm data from those studies. Note that the experimental data shown are the raw data and are not scaled to a constant pressure, whereas the simulated ignition delays are at a constant initial pressure of 50 atm. It can be seen that the ignition delays are over-predicted over the nearly entire temperature range of 795–1160 K studied. Nevertheless, the predicted ignition delays are within approximately a factor of 1.5 of the experiments, indicating good agreement overall and a substantial improvement from the previous version of the model. Furthermore, the simulations shown here are

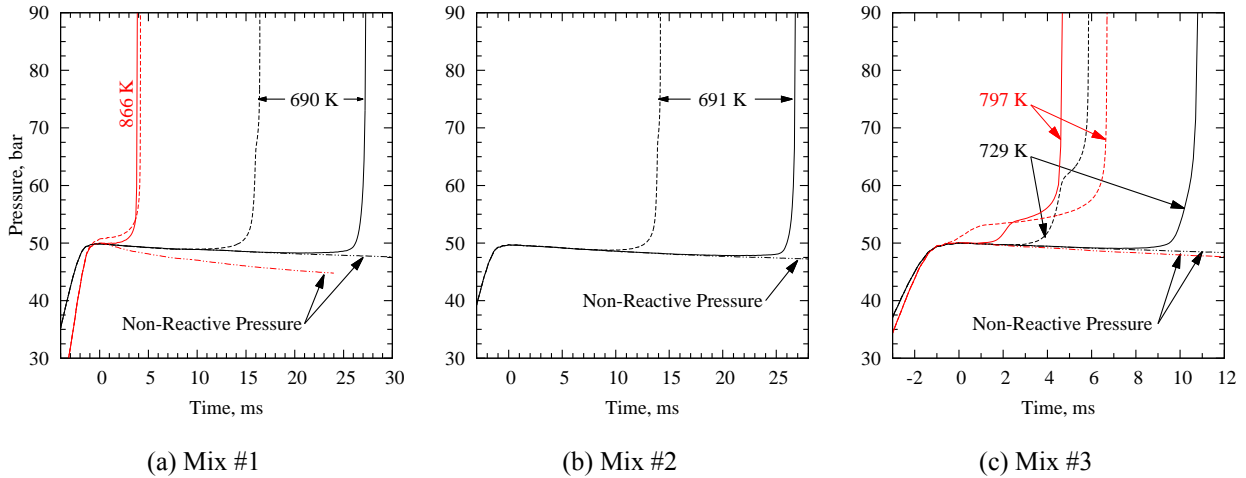


Figure 5.6: Comparison of selected simulated and experimental pressure traces at $P_C = 50$ bar. Red lines indicate that the pressure profile of the reactive simulation deviates from the non-reactive case prior to EOC. Solid lines: experiment; dashed lines: reactive simulation; dot-dot-dashed lines: non-reactive simulation.

of the CONV type and do not account for any facility dependent effects present in the experiments. Although the experimentalists noted in [83, 84] that the effect of such considerations is minimal in their studies, including facility dependent effects will tend to make the simulations ignite sooner and improve the agreement, especially for cases with ignition delays longer than approximately 1000 μ s.

As discussed in ??, one of the updates to the model was to increase the activation energy of ketohydroperoxide decomposition, from $E_a = 39 \text{ kcal mol}^{-1}$ ($163.2 \text{ kJ mol}^{-1}$) to $41.6 \text{ kcal mol}^{-1}$ ($174.1 \text{ kJ mol}^{-1}$). This update substantially improved the prediction of the low-temperature ignition delays, including the first stage and overall ignition delays. As mentioned by Curran et al. [135], “the high activation energy [of ketohydroperoxide decomposition] ensures an induction period during which the ketohydroperoxide concentration builds up.” Furthermore, updating this activation energy does not affect the high-temperature ignition delays. A comparison of calculated ignition delays demonstrating the effect of this update is shown in Fig. 5.8.

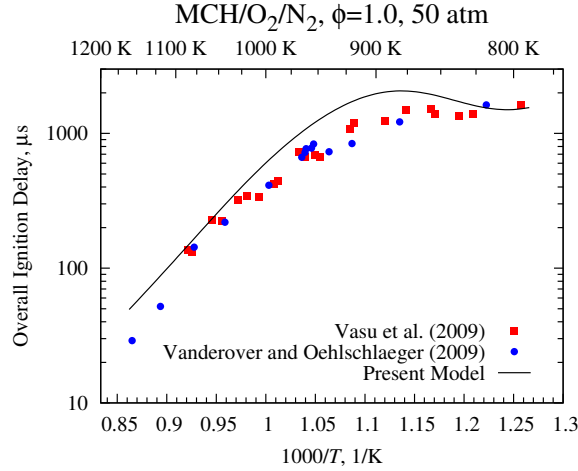


Figure 5.7: Comparison of the present model with the experiments from Vasu et al. [83] and Vanderover and Oehlschlaeger [84] near 50 atm and for stoichiometric mixtures in O_2/N_2 air.

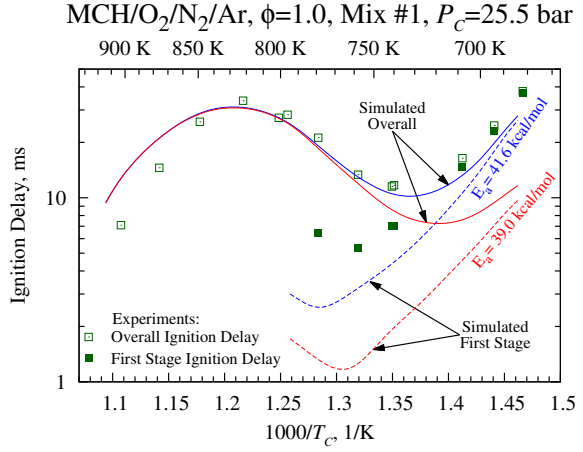


Figure 5.8: Comparison of mechanism performance with the activation energy of ketohydroperoxide decomposition set at $41.6 \text{ kcal mol}^{-1}$ (blue) and $39.0 \text{ kcal mol}^{-1}$ (red). Experimental ignition delays are shown in green symbols.

5.6 Discussion

5.6.1 Path Analysis

The relatively good agreement of the updated model with the experimental data suggests that a more detailed analysis of the mechanism is a worthwhile exercise and such analysis may point the way to further improvements to the mechanism. We begin with a reaction path analysis. The present reaction path analysis is conducted using a CONV (adiabatic, constant-volume) type simulation for three initial temperatures (700, 800, and 900 K), at 25.5 bar and for Mix #1 (the stoichiometric case). For the other mixture conditions and pressures considered in this work, the absolute percentages for each channel change slightly. However, the analysis of the reaction pathways is the same for all of the equivalence ratios and pressures considered in the experiments presented previously. The three temperatures considered in this analysis correspond to the low-temperature, peak of the NTC, and high-temperature portions of the ignition delay curve illustrated in Fig. 5.8; their results are shown in Fig. 5.9 with plain text, bold text, and italic text, respectively.

The path analysis presented in Fig. 5.9 is an integrated analysis where the rate of production (ROP) of each species by each reaction has been integrated with respect to time up to 20% fuel consumption. The integrated ROPs from each reaction are normalized by the total production or destruction of that species up to 20% fuel decomposition, such that reactions that produce a species are normalized by the total production of the species and reactions that consume a species are normalized by the total consumption of that species. The percentages in Fig. 5.9 therefore represent the percent of the given reactant that is consumed to form the given product by all reactions that can form a particular product. Species such as hydroperoxyalkyl radicals (QOOH), alkyl hydroperoxides (ROOH), and methylcyclohexenes (MCH-ene) are shown as lumped on the path diagram; however, these species are unlumped in the mechanism and presented as a lumped sum for simplicity in this diagram. Note that not all of the pathways present in the mechanism for each species are presented in Fig. 5.9, again for simplicity; the pathways that are shown in Fig. 5.9 typically account for more than 95% of the consumption of each species.

The first step of fuel breakdown occurs by H-atom abstraction at these pressure and temperature conditions. None of the fuel is directly decomposed by unimolecular reactions. Each of the seven possible radicals are formed in comparable quantities; however, due to the symmetry of MCH, sites 2 and 3 are equivalent to sites 6 and 5, respectively, so mchr2 and mchr3 have close to double the production rate compared to the other radicals. It is interesting to note that the production of mchr2, mchr3, and mchr4 increase as the initial temperature increases and the production of mchr1 and cyclohexch2 decrease to compensate. However, the change is small, no more than 2 percentage points for each radical.

The most important second step is oxygen addition (i.e. formation of ROO) at all of the initial temperatures in this analysis. The importance of this reaction diminishes for each radical as the initial temperature increases due to the increasing importance of β -scission reactions. At 700 K, less than 0.05% of each of the fuel radicals is consumed via β -scission. Between 800 and 900 K, the percentages of mchr1, mchr2, mchr3, and mchr4 that are decomposed via β -scission increase by several thousand percent each; nevertheless, the absolute change is small and the consumption

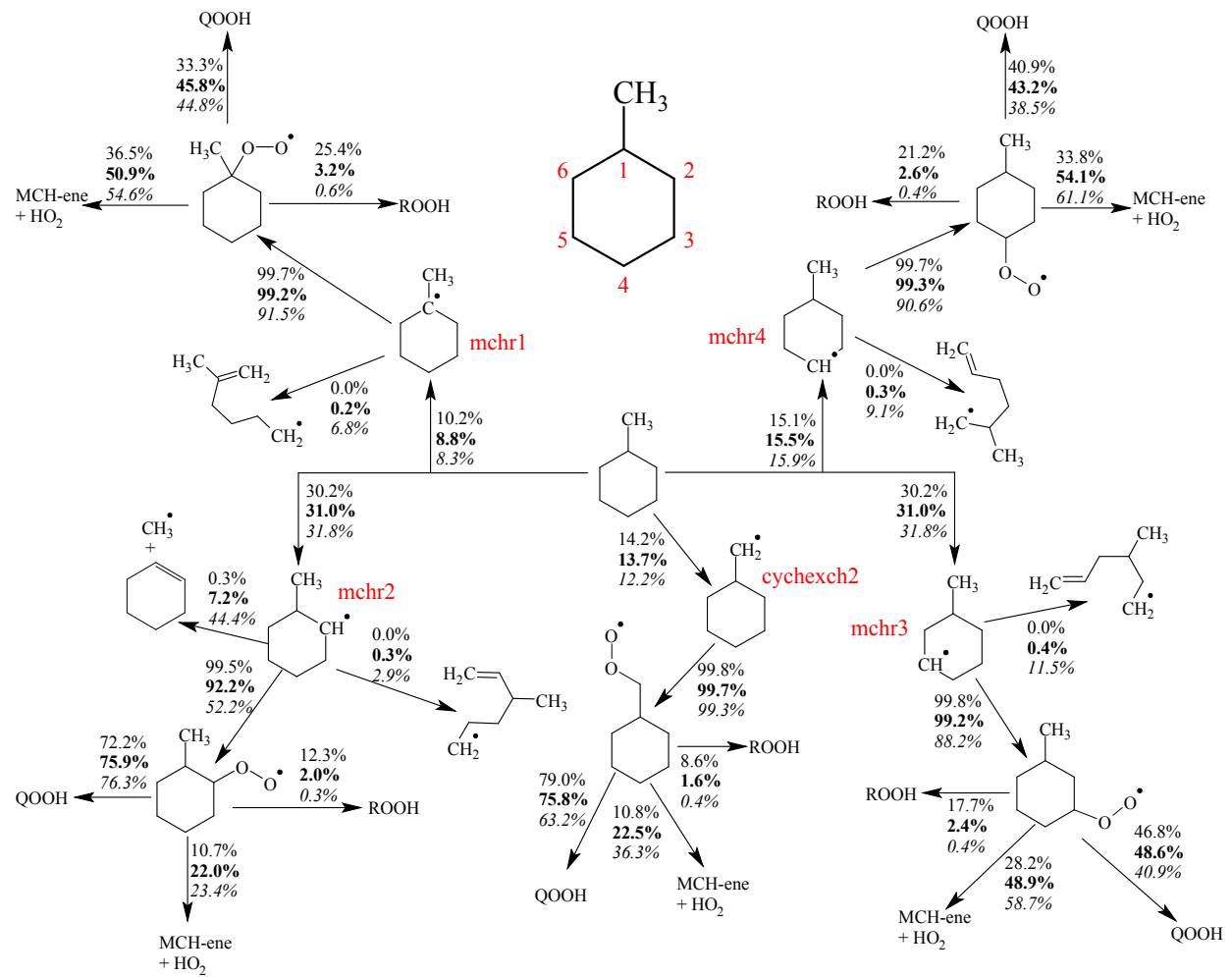


Figure 5.9: Path analysis of MCH combustion. Initial conditions are 25.5 bar and Mix #1 ($\phi = 1.0$) and 700 K (plain text), 800 K (bold text), 900 K (italic text). Note that not all possible reaction pathways are shown for each species.

of these radicals still occurs mostly by oxygen addition. The mchr1, mchr3, and mchr4 radicals undergo scission of the cyclohexyl ring, whereas mchr2 primarily scissions at the methyl-cyclohexyl bond. This beta scission of mchr2 competes significantly with its consumption by O₂ at 900 K. Furthermore, the increasing importance of the ring opening reactions from 800 K to 900 K means that chain propagation pathways (instead of effective chain termination pathways forming methylcyclohexene and hydroperoxyl) are available, increasing the reactivity. Finally, even at the elevated initial temperature of 900 K, cychexch2 does not undergo significant ring opening. Instead, it will scission an H atom from site 1 or steal an oxygen atom from hydroperoxyl to form an alkoxy radical (RO) when it does not undergo oxygen addition (these pathways each only consume about 0.3% of cychexch2 and hence are not shown in Fig. 5.9).

Returning to the low temperature pathways, there are four important classes of reactions that consume the ROO radicals in the current mechanism. These classes are: C1) internal H-atom transfer (isomerization) to form QOOH; C2) direct elimination of hydroperoxyl and methylcyclohexene; C3) H-abstraction by ROO from either the fuel or hydroperoxyl to form ROOH; and, C4) reactions among the ROO radicals. Class C4 consumes less than $\approx 5\%$ of each of the ROO radicals at 700 K and less than $\approx 0.1\%$ for the other temperatures and this class is therefore not shown on the path diagram in Fig. 5.9. Of the other three classes, C1 (formation of QOOH) is the predominant pathway in the low temperature ignition process. Nevertheless, the direct elimination of methylcyclohexene and hydroperoxyl and the formation of ROOH are important at low temperatures as well.

For all of the temperatures considered here, a majority of the ROOH is formed by reactions of ROO with hydroperoxyl to give ROOH and an oxygen molecule. At the initial temperature of 700 K, approximately 15% of the fuel reacts to form ROOH, indicating its importance in low-temperature MCH combustion. The primary route of ROOH formation in this mechanism (H-abstraction from hydroperoxyl by ROO) has not been well studied at combustion relevant temperatures [136] and is therefore a good candidate for further investigation given its importance in the model for MCH combustion.

As the temperature increases, the formation of ROOH becomes substantially less important

while the direct HO₂ elimination reaction becomes more important. The increase in production of methylcyclohexene and hydroperoxyl plays a role in the NTC region of ignition delay because this is effectively a chain terminating channel until the temperature increases enough that the sequence MCH+HO₂=R+H₂O₂; H₂O₂(+M)=2OH(+M) becomes important and drives the overall ignition.

Interestingly, for most of the ROO radicals, the change in the fraction of ROO consumed to form QOOH is non-monotonic as temperature increases. That is, for mch1oo, mch3oo, and mch4oo the production of QOOH increases in going from 700 K to 800 K, then decreases going from 800 K to 900 K due to the increasing importance of the HO₂ elimination channel (due to nuances in the various reaction paths, mch2oo and chxch2oo do not follow this trend). Furthermore, the branching ratios in the decomposition of the QOOH species change as the temperature is increased (not shown in Fig. 5.9). At the lowest temperature (700 K), the formation of hydroperoxyalkylperoxy radicals (OOQOOH) is favored, leading to low-temperature chain branching and the two-stage ignition phenomenon. However, at 800 K and 900 K, the QOOH tends to decompose into a heptenone and a hydroxyl radical, or one of two epoxide species. Due to the apparent importance of these species in the intermediate temperature decomposition of MCH, further investigation of their pathways is warranted.

5.6.2 Sensitivity Analysis

Our second type of analysis is a brute force, one-at-a-time sensitivity analysis. In this work, the sensitivity of the ignition delay to the reaction rates is considered. Due to the size of the mechanism, only the reactions of the fuel and the fuel radicals up to the OOQOOH species are considered. This approach is justified because many of the reactions of the C₀–C₄ base mechanism are known to be important to the ignition process (e.g., H₂O₂(+M)=2OH(+M)), but we are more interested in the effect of updates to the fuel specific sub-mechanism. The sensitivity index is defined in Eq. (5.1),

$$S_i = \frac{\ln(\tau_{i,2}/\tau_{i,1})}{\ln(k_{i,2}/k_{i,1})} \quad (5.1)$$

where τ is the ignition delay time, either first stage or overall, k is the reaction rate, and subscript i indicates the reaction number. The numbered subscripts in Eq. (5.1) indicate the type of modification that has been made to the rate of reaction i when computing the ignition delay, as discussed in the following.

The reaction rates are modified by multiplying and dividing the pre-exponential constant by a factor f . Thus, the forward and reverse rates are simultaneously modified. Special care is taken to properly modify reaction rates with pressure dependence and explicit reverse parameters. Each rate is modified sequentially and the ignition delay is computed; the pre-exponential constant is reset to its nominal value before modifying the next reaction. Finally, the nominal ignition delay with no rate modification is computed. Thus, each set of reactor input conditions requires $2N + 1$ model evaluations, where N is the number of reactions considered in the sensitivity analysis and N may be less than or equal to the total number of reactions.

The $2N + 1$ model evaluations result in $4N + 2$ ignition delays if two-stage ignition is present and $2N + 1$ ignition delays otherwise. These ignition delays are used to compute the sensitivity indices according to Eq. (5.1). In the case of bidirectional sensitivity indices, the subscript 2 in Eq. (5.1) is associated with multiplication by f and the subscript 1 is associated with division by f , resulting in $2N$ sensitivity indices if two-stage ignition is present and N indices otherwise. In the case of unidirectional sensitivity indices, the subscript 2 is associated with either multiplication or division by f and the subscript 1 is associated with the nominal ignition delay, $\tau_{i,1} = \tau_1$. For unidirectional sensitivity indices, $4N$ indices are obtained if two-stage ignition is present and $2N$ are obtained otherwise.

In this work, the bidirectional sensitivity is used with $f = 10$. For all of the reactions considered here, multiplying and dividing a given rate had opposite effects on the ignition delay. Thus, if the ignition delay increased (relative to the nominal case) when the rate of a certain reaction was multiplied, the ignition delay decreased (relative to the nominal case) when the rate of the same reaction was divided and vice versa. Since $k_{i,2}$ is greater than $k_{i,1}$ by definition, the sensitivity index S_i will be positive if $\tau_{i,2} > \tau_{i,1}$ (i.e. increasing the rate increases the ignition delay) and

negative if $\tau_{i,2} < \tau_{i,1}$ (i.e. increasing the rate decreases the ignition delay). The sensitivity analysis is run at the same conditions of the path analysis: CONV simulation, initial temperatures of 700, 800, and 900 K, initial pressure of 25.5 bar, and Mix #1. As with the path analysis, similar results are obtained for other pressures and mixtures.

Figure 5.10 shows the sensitivity indices for the five reactions (among all the reactions considered in the present sensitivity analysis) to which the overall ignition delay is most sensitive for each temperature studied (700, 800, and 900 K). For the results at 700 and 800 K, the bidirectional sensitivity of the first stage ignition delay to the same reactions is also shown, except for two reactions at 800 K for which the unidirectional sensitivity is plotted. The reasons for this will be discussed in due course. It should be noted that the sensitivity indices of the first stage ignition delay have a slightly different ranking than the indices of the overall ignition delay. Therefore, the rank of the first stage sensitivity index of the reactions shown is given in parentheses next to the bar. At 700 K, the sensitivity of the overall ignition delay is in red and the sensitivity of the first stage ignition delay is in blue; at 800 K, the sensitivity of the overall ignition delay is in grey and the sensitivity of the first stage ignition delay is in green. The most sensitive reaction affecting the first stage ignition delay at 800 K is found to be $\text{MCH}+\text{OH}=\text{mchr3}+\text{H}_2\text{O}$, although it is not listed in Fig. 5.10. At 900 K, there is no first stage ignition, and thus no sensitivity of the first stage ignition delay.

Under the pressure/stoichiometry conditions of the present simulations, 800 K is approximately the highest initial temperature at which distinct two-stage ignition (i.e. two inflection points in the temperature or pressure trace) is found for MCH with the current mechanism. As such, several reactions affect the ignition strongly enough to eliminate the first inflection point. These reactions are given in Table 5.2 for either multiplication or division of the rate by the factor $f = 10$. The naming convention of the species listed in Table 5.2 can be found in Figs. 5.9 and 5.11 and Appendix A. Two reactions shown in Table 5.2 also appear in Fig. 5.10, namely (R1) $\text{mch2oo}=\text{mch2ene}+\text{ho2}$ and (R2) $\text{mch2qx}+\text{o2}=\text{mch2qxqj}$. For these reactions at 800 K, the unidirectional sensitivity index is shown in Fig. 5.10, where $\tau_{i,2}$ in Eq. (5.1) is found by division of the rate for $i = R1$ and by multiplication of the rate for $i = R2$.

Table 5.2: Reactions that eliminate the first inflection point for a nominal case with two-stage ignition.

Multiplication	Division
$mch2oo = mch2ene + ho2$	$mch2qx + o2 = mch2qxqj$
$mch3oo = mch2ene + ho2$	
$mch3oo = mch3ene + ho2$	
$mch + oh = mchr1 + h2o$	
$mch + oh = mchr4 + h2o$	
$mch + oh = mchr3 + h2o$	

The role of the ROO=methylcyclohexene+HO₂ reactions in the left column of Table 5.2 in eliminating the first stage of ignition is clear—this set of reactions diverts ROO radicals from entering the low-temperature chain branching pathway via QOOH that leads to the two-stage ignition. Similarly, in the right column, decreasing the rate of the reaction of oxygen with QOOH to form OOQOOH reduces the rate of chain branching that leads to two-stage ignition. Concerning the reactions of the fuel with OH in the left column of Table 5.2, increasing these rates increases the formation of fuel radicals that are less reactive at low temperature than the cyclohexch₂ and mchr₂ radical. For example, the mchr₂ radical adds to O₂ and forms a peroxy radical (mch2oo) that has a fast RO₂ isomerization path to QOOH involving the abstraction of an H atom from the methyl group. This ROO isomerization is the path calculated and discussed in Section 4.1 of [128]. QOOH subsequently adds to O₂ and leads to chain branching. The high reactivity of cyclohexch₂ and mchr₂ at low temperature is reflected by the high percentages at 800 K (>70%) leading to QOOH from cyclohexch₂oo and mch2oo in Fig. 5.9.

In general, Fig. 5.10 shows that the ignition delay is sensitive to different sets of reactions at the three temperatures, although there is some overlap. The overlapping reactions confound simple recommendations for rate improvements. For instance, at 700 K, increasing the overall ignition delay will improve agreement with the experimental data, but at 800 K, the agreement is already quite good. Therefore, adjusting any of the rates to improve the agreement with the overall ignition delay at 700 K will probably make the agreement worse at 800 K. However, the first stage ignition delays at 700 K and 800 K are both under-predicted; furthermore, two-stage ignition is predicted

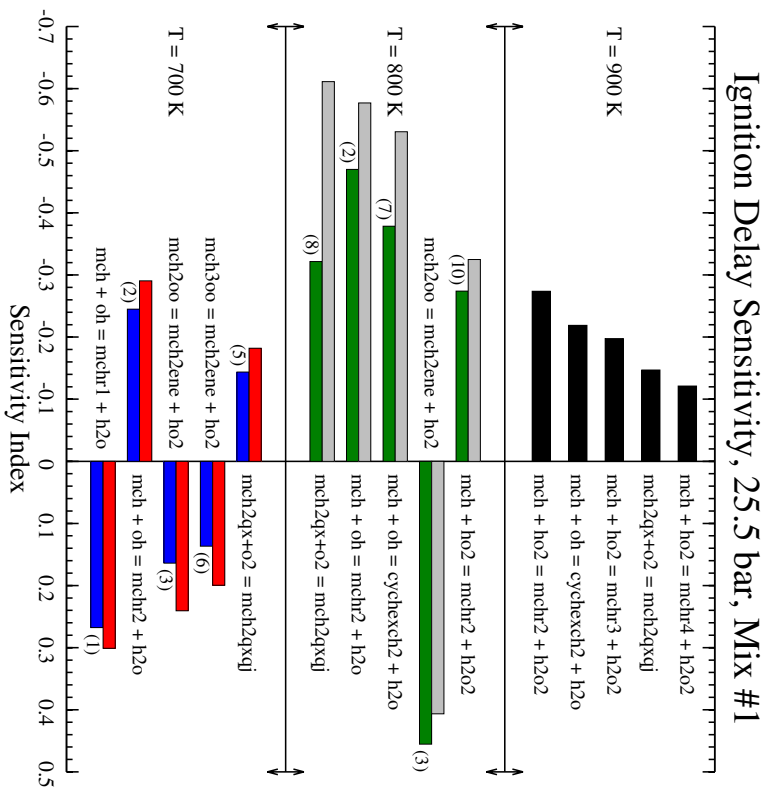


Figure 5.10: Sensitivity of the ignition delay to various reaction rates for Mix #1 ($\phi = 1.0$), 25.5 bar and three temperatures (700, 800, and 900 K). At 700 K, the sensitivity of the overall ignition delay is in red and the sensitivity of the first stage ignition delay is in blue. At 800 K, the sensitivity of the overall ignition delay is in grey and the sensitivity of the first stage ignition delay is in green. At 900 K, the sensitivity of the overall ignition delay is in black. Numbers in parentheses represent the ranking of the first stage sensitivity indices.

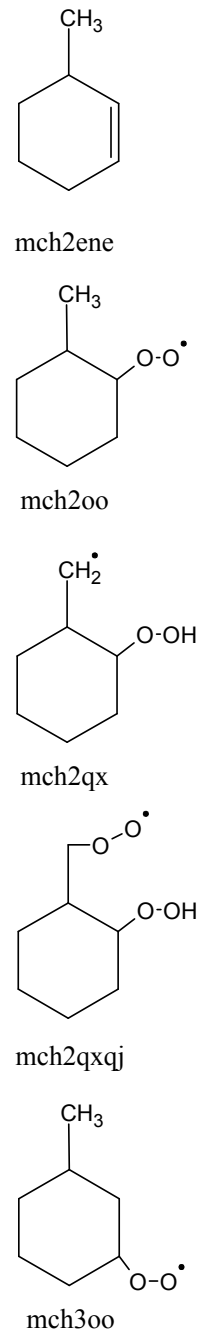


Figure 5.11: Species mentioned in Fig. 5.10 or Table 5.2 and not included in Fig. 5.9.

at temperatures for which the experimental ignition is single stage. It should therefore be possible to adjust several rate constants simultaneously to improve agreement with the first stage ignition delay and not deteriorate agreement with the overall ignition delay. To accomplish the simultaneous improvement of agreement of first stage and overall ignition delays, the rate constants of reactions that control the second stage ignition delay may also need to be adjusted (where second stage ignition delay is the difference between the overall ignition delay and the first stage ignition delay).

Interestingly, the formation and destruction reactions of ROOH species do not appear in Fig. 5.10, despite their importance in the destruction of ROO radicals, particularly at 700 K (see Fig. 5.9). This may be due to the fact that formation of ROOH by reaction with HO₂ followed by consumption of ROOH is a chain propagation path through the reactions ROO+HO₂=ROOH+O₂; ROOH=RO+OH. In this sequence two radicals are formed (RO, OH) and two radicals are consumed (ROO, HO₂). Thus, the formation of ROOH by reaction with HO₂ and its subsequent destruction has a somewhat neutral effect on the radical pool.

At 900 K, the overall ignition delay is particularly sensitive to reactions that form hydrogen peroxide, which decomposes to two hydroxyl radicals as the temperature increases during the induction period. Therefore, increasing the rate of formation of hydrogen peroxide will increase the formation of hydroxyl radical and decrease the overall ignition delay. At 900 K, the overall ignition delay is over-predicted, so to improve the results the overall ignition delay should be reduced (i.e. increasing the rates of reactions with negative sensitivity will improve the comparison). In addition, many of the reactions that are important at 900 K are not important at 700 and 800 K, implying that changes made to the rates to improve the high-temperature agreement will not significantly change the agreement at lower temperature. In particular, the MCH+HO₂ rate constants have not been measured or calculated to our knowledge and are based on acyclic alkane rate constants [137]. They have uncertainties of at least a factor of 2 and as much as a factor of 10 based on the work of Aguilera-Iparraguirre et al. [137]. Increasing these rate constants would improve the agreement with the experimental ignition data at 900 K in the RCM and shock tube. Experimental measurements and theoretical calculations are needed for the fuel+HO₂ reaction class to reduce

this uncertainty in the rate constants.

5.7 Conclusions

In this study, new experimental data are collected for methylcyclohexane autoignition in a heated rapid compression machine. Following the work of Mittal and Sung [89], three mixtures of MCH/O₂/N₂/Ar at equivalence ratios of $\phi = 0.5, 1.0$, and 1.5 are used and the ignition delays are measured at compressed pressure of 50 bar, for compressed temperatures in the range of 690–900 K. Two-stage ignition phenomena are reported for the stoichiometric and rich mixtures. However, substantial reactivity during the compression stroke limited the temperature range over which ignition delays could be reported, especially for the lean case. For these mixtures where the fuel concentration was kept constant, the order of reactivity, in terms of inverse overall ignition delay, is $\phi = 0.5 > \phi = 1.0 > \phi = 1.5$.

In addition, an existing model for the combustion of MCH developed by Pitz et al. [14] is updated with new reaction rates and pathways. The new model shows good agreement with the overall ignition delays measured in this study, as well as the overall ignition delays measured in the studies of Vasu et al. [83], Vanderover and Oehlschlaeger [84], and Mittal and Sung [89]. However, the first stage ignition delays are uniformly under-predicted and in several cases, first stage ignition is predicted by the model where experimental ignition response shows no two-stage character. To help understand the fuel decomposition pathways and the reactions controlling the ignition, further analysis of the present mechanism is conducted.

First, reaction path analysis is conducted for low-, intermediate-, and high-temperature ignition considered in this study. The results show that MCH primarily decomposes by H-abstraction reactions involving OH and HO₂ radicals, followed by oxygen addition reactions. At low temperatures, the oxygen addition is followed by isomerization to QOOH species and second oxygen addition, leading to the low-temperature chain branching characteristic of two-stage ignition. At intermediate temperatures, the elimination of methylcyclohexene and HO₂ becomes competitive with the

isomerization reaction, leading to the NTC region of the overall ignition delay. Finally, at high temperatures, MCH+HO₂ reactions form H₂O₂ and end the NTC region.

Second, a brute force sensitivity analysis is conducted to identify the reactions of the fuel and primary fuel radicals that control the ignition process. The overall and first stage ignition events at low and intermediate temperatures are primarily controlled by the initial reactions to form fuel radicals, especially H-abstraction by OH. At high temperatures, the controlling reactions are still the fuel radical formation reactions, but now the ignition process is controlled by H-abstraction by hydroperoxyl instead of hydroxyl. Combined, these analyses suggest that further investigation of several of the low-temperature fuel decomposition pathways is required and more accurate rate constants for fuel+HO₂ reactions are needed.

Chapter 6

Conclusions and Future Directions

References

- [1] Sims, R., Schock, R., Adegbulgbe, A., Fenhamm, J., Konstantinaviciute, I., Moomaw, W., et al. In: *Clim. Chang. 2007 Mitig.* Ed. by Metz, B., Davidson, O., Bosch, P., Dave, R., and Meyer, L. New York, NY, 2007. URL: <http://www.ipcc.ch/pdf/assessment-report/ar4/wg3/ar4-wg3-chapter4.pdf>.
- [2] US Energy Information Administration. *International Energy Outlook 2013*. Tech. rep. July 2013. URL: [http://www.eia.gov/forecasts/ieo/pdf/0484\(2013\).pdf](http://www.eia.gov/forecasts/ieo/pdf/0484(2013).pdf).
- [3] US Energy Information Administration. *EIA Monthly Energy Review*. Tech. rep. May 2013. URL: <http://www.eia.gov/totalenergy/data/monthly/archive/00351305.pdf>.
- [4] Avakian, M. D., Dellinger, B., Fiedler, H., Gullet, B., Koshland, C., Marklund, S., et al. *Environ. Health Perspect.*, vol. 110, no. 11 (Nov. 2002), pp. 1155–1162. URL: <http://www.ncbi.nlm.nih.gov/articlerender.fcgi?artid=1241073%5C&tool=pmcentrez%5C&rendertype=abstract>.
- [5] Owen, N. A., Inderwildi, O. R., and King, D. A. *Energy Policy*, vol. 38, no. 8 (Aug. 2010), pp. 4743–4749. DOI: [10.1016/j.enpol.2010.02.026](https://doi.org/10.1016/j.enpol.2010.02.026).
- [6] Westbrook, C. K. and Dryer, F. L. *Prog. Energy Combust. Sci.*, vol. 10, no. 1 (Jan. 1984), pp. 1–57. DOI: [10.1016/0360-1285\(84\)90118-7](https://doi.org/10.1016/0360-1285(84)90118-7).
- [7] Smith, G. P., Golden, D. M., Frenklach, M., Moriarty, N. W., Eiteneer, B., Goldenberg, M., et al. *GRI-Mech 3.0*. URL: <http://www.me.berkeley.edu/gri-mech/> (visited on 02/19/2010).

- [8] Wang, H., You, X., Joshi, A. V., Davis, S. G., Laskin, A., Egolfopoulos, F. N., et al. *USC-Mech Version II. High-Temperature Combustion Reaction Model of H₂/CO/C1-C4 Compounds*. 2007. URL: <http://ignis.usc.edu/Mechanisms/USC-Mech%20II/USC%5CMech%20II.htm> (visited on 04/08/2014).
- [9] Metcalfe, W. K., Burke, S. M., Ahmed, S. S., and Curran, H. J. *Int. J. Chem. Kinet.*, vol. 45, no. 10 (Oct. 2013), pp. 638–675. DOI: [10.1002/kin.20802](https://doi.org/10.1002/kin.20802).
- [10] Kohse-Höinghaus, K., Oßwald, P., Cool, T. A., Kasper, T., Hansen, N., Qi, F., et al. *Angew. Chemie*, vol. 49, no. 21 (May 2010), pp. 3572–3597. DOI: [10.1002/anie.200905335](https://doi.org/10.1002/anie.200905335).
- [11] Pitz, W. J. and Mueller, C. J. *Prog. Energy Combust. Sci.*, vol. 37, no. 3 (June 2011), pp. 330–350. DOI: [10.1016/j.pecs.2010.06.004](https://doi.org/10.1016/j.pecs.2010.06.004).
- [12] Dooley, S., Won, S. H., Heyne, J. S., Farouk, T. I., Ju, Y., Dryer, F. L., et al. *Combust. Flame*, vol. 159, no. 4 (Apr. 2012), pp. 1444–1466. DOI: [10.1016/j.combustflame.2011.11.002](https://doi.org/10.1016/j.combustflame.2011.11.002).
- [13] Anand, K., Ra, Y., Reitz, R. D., and Bunting, B. *Energy Fuel*, vol. 25, no. 4 (Apr. 2011), pp. 1474–1484. DOI: [10.1021/ef101719a](https://doi.org/10.1021/ef101719a).
- [14] Pitz, W. J., Naik, C. V., Mhaoldúin, T. N., Westbrook, C. K., Curran, H. J., Orme, J., et al. *Proc. Combust. Inst.*, vol. 31, no. 1 (Jan. 2007), pp. 267–275. DOI: [10.1016/j.proci.2006.08.041](https://doi.org/10.1016/j.proci.2006.08.041).
- [15] Briker, Y., Ring, Z., Iacchelli, A., McLean, N., Rahimi, P. M., Fairbridge, C., et al. *Energy Fuel*, vol. 15, no. 1 (Jan. 2001), pp. 23–37. DOI: [10.1021/ef000106f](https://doi.org/10.1021/ef000106f).
- [16] Farrell, J. T., Cernansky, N. P., Dryer, F. L., Friend, D. G., Hergart, C. A., Law, C. K., et al. *Development of an Experimental Database and Kinetic Models for Surrogate Diesel Fuels*. Tech. rep. SAE International, 2007. DOI: [10.4271/2007-01-0201](https://doi.org/10.4271/2007-01-0201).

- [17] Edwards, T., Colket, M. B., Cernansky, N., Dryer, F. L., Egolfopoulos, F. N., Friend, D., et al. “Development of an Experimental Database and Kinetic Models for Surrogate Jet Fuels”. In: *45th AIAA Aerosp. Sci. Meet. Exhib.* American Institute of Aeronautics and Astronautics. Reno, NV, Jan. 2007. DOI: [10.2514/6.2007-770](https://doi.org/10.2514/6.2007-770).
- [18] Bielefeld, T., Frassoldati, A., Cuoci, A., Faravelli, T., Ranzi, E., Niemann, U., et al. *Proc. Combust. Inst.*, vol. 32, no. 1 (Jan. 2009), pp. 493–500. DOI: [10.1016/j.proci.2008.06.214](https://doi.org/10.1016/j.proci.2008.06.214).
- [19] Naik, C. V., Pitz, W. J., Westbrook, C. K., Sjöberg, M., Dec, J. E., Orme, J., et al. *Detailed Chemical Kinetic Modeling of Surrogate Fuels for Gasoline and Application to an HCCI Engine*. Tech. rep. Warrendale, PA: SAE International, 2005. DOI: [10.4271/2005-01-3741](https://doi.org/10.4271/2005-01-3741).
- [20] Peralta-Yahya, P. P., Zhang, F., Cardayre, S. B. del, and Keasling, J. D. *Nature*, vol. 488, no. 7411 (Aug. 2012), pp. 320–328. DOI: [10.1038/nature11478](https://doi.org/10.1038/nature11478).
- [21] Afeefy, H., Liebman, J., and Stein, S. In: *NIST Chem. WebBook, NIST Stand. Ref. Database Number 69*. Ed. by Linstrom, P. and Mallard, W. Gaithersburg MD, 2014. URL: <http://webbook.nist.gov>.
- [22] Davis, S. C., Diegel, S. W., and Boundy, R. G. *Transportation Energy Data Book*. 32nd ed. Oak Ridge, Tennessee, 2013. URL: <http://cta.ornl.gov/data/index.shtml>.
- [23] Niven, R. *Renew. Sustain. Energy Rev.*, vol. 9, no. 6 (Dec. 2005), pp. 535–555. DOI: [10.1016/j.rser.2004.06.003](https://doi.org/10.1016/j.rser.2004.06.003).
- [24] Somma, D., Lobkowicz, H., and Deason, J. P. *Clean Technol. Environ. Policy*, vol. 12, no. 4 (June 2009), pp. 373–380. DOI: [10.1007/s10098-009-0234-3](https://doi.org/10.1007/s10098-009-0234-3).
- [25] Harvey, B. G. and Meylemans, H. A. *J. Chem. Technol. Biotechnol.*, vol. 86, no. 1 (Jan. 2011), pp. 2–9. DOI: [10.1002/jctb.2540](https://doi.org/10.1002/jctb.2540).
- [26] Nigam, P. S. and Singh, A. *Prog. Energy Combust. Sci.*, vol. 37, no. 1 (Feb. 2011), pp. 52–68. DOI: [10.1016/j.pecs.2010.01.003](https://doi.org/10.1016/j.pecs.2010.01.003).

- [27] Smith, K. M., Cho, K.-M., and Liao, J. C. *Appl. Microbiol. Biotechnol.*, vol. 87, no. 3 (July 2010), pp. 1045–1055. DOI: [10.1007/s00253-010-2522-6](https://doi.org/10.1007/s00253-010-2522-6).
- [28] Dernotte, J., Mounaim-Rousselle, C., Halter, F., and Seers, P. *Oil Gas Sci. Technol.*, vol. 65, no. 2 (Nov. 2009), pp. 345–351. DOI: [10.2516/ogst/2009034](https://doi.org/10.2516/ogst/2009034).
- [29] Szwaja, S. and Naber, J. *Fuel*, vol. 89, no. 7 (July 2010), pp. 1573–1582. DOI: [10.1016/j.fuel.2009.08.043](https://doi.org/10.1016/j.fuel.2009.08.043).
- [30] Kim, D. H., Lee, J. M., Park, E. H., Song, J. H., and Park, S. I. *Int. J. Automot. Technol.*, vol. 12, no. 3 (May 2011), pp. 409–416. DOI: [10.1007/s12239-011-0048-2](https://doi.org/10.1007/s12239-011-0048-2).
- [31] Veloo, P. S. and Egolfopoulos, F. N. *Proc. Combust. Inst.*, vol. 33, no. 1 (Sept. 2011), pp. 987–993. DOI: [10.1016/j.proci.2010.06.163](https://doi.org/10.1016/j.proci.2010.06.163).
- [32] Dagaut, P. and Togbé, C. *Energy Fuel*, vol. 23, no. 7 (July 2009), pp. 3527–3535. DOI: [10.1021/ef900261f](https://doi.org/10.1021/ef900261f).
- [33] Hansen, N., Harper, M. R., and Green, W. H. *Phys. Chem. Chem. Phys.*, vol. 13, no. 45 (Dec. 2011), pp. 20262–20274. DOI: [10.1039/c1cp21663e](https://doi.org/10.1039/c1cp21663e).
- [34] Hansen, N., Merchant, S. S., Harper, M. R., and Green, W. H. *Combust. Flame*, vol. 160, no. 11 (Nov. 2013), pp. 2343–2351. DOI: [10.1016/j.combustflame.2013.05.013](https://doi.org/10.1016/j.combustflame.2013.05.013).
- [35] Grana, R., Frassoldati, A., Faravelli, T., Niemann, U., Ranzi, E., Seiser, R., et al. *Combust. Flame*, vol. 157, no. 11 (June 2010), pp. 2137–2154. DOI: [10.1016/j.combustflame.2010.05.009](https://doi.org/10.1016/j.combustflame.2010.05.009).
- [36] Van Geem, K. M., Pyl, S. P., Marin, G. B., Harper, M. R., and Green, W. H. *Ind. Eng. Chem. Res.*, vol. 49, no. 21 (Nov. 2010), pp. 10399–10420. DOI: [10.1021/ie1005349](https://doi.org/10.1021/ie1005349).
- [37] Cai, J., Zhang, L., Zhang, F., Wang, Z., Cheng, Z., Yuan, W., et al. *Energy Fuel*, vol. 26, no. 9 (Sept. 2012), pp. 5550–5568. DOI: [10.1021/ef3011965](https://doi.org/10.1021/ef3011965).
- [38] Cai, J., Yuan, W., Ye, L., Cheng, Z., Wang, Y., Zhang, L., et al. *Combust. Flame*, vol. 160, no. 10 (Oct. 2013), pp. 1939–1957. DOI: [10.1016/j.combustflame.2013.04.010](https://doi.org/10.1016/j.combustflame.2013.04.010).

- [39] Lefkowitz, J. K., Heyne, J. S., Won, S. H., Dooley, S., Kim, H. H., Haas, F. M., et al. *Combust. Flame*, vol. 159, no. 3 (Mar. 2012), pp. 968–978. DOI: [10.1016/j.combustflame.2011.10.004](https://doi.org/10.1016/j.combustflame.2011.10.004).
- [40] Heyne, J. S., Dooley, S., and Dryer, F. L. *J. Phys. Chem. A*, vol. 117, no. 37 (Oct. 2013), pp. 8997–9004. DOI: [10.1021/jp404143f](https://doi.org/10.1021/jp404143f).
- [41] Stranic, I., Pang, G. A., Hanson, R. K., Golden, D. M., and Bowman, C. T. *J. Phys. Chem. A*, vol. 117, no. 23 (June 2013), pp. 4777–4784. DOI: [10.1021/jp402176e](https://doi.org/10.1021/jp402176e).
- [42] Pang, G. A., Hanson, R. K., Golden, D. M., and Bowman, C. T. *J. Phys. Chem. A*, vol. 116, no. 19 (May 2012), pp. 4720–4725. DOI: [10.1021/jp302719j](https://doi.org/10.1021/jp302719j).
- [43] Pang, G. A., Hanson, R. K., Golden, D. M., and Bowman, C. T. *J. Phys. Chem. A*, vol. 116, no. 10 (Mar. 2012), pp. 2475–2483. DOI: [10.1021/jp211885p](https://doi.org/10.1021/jp211885p).
- [44] Seal, P., Oyedepo, G. A., and Truhlar, D. G. *J. Phys. Chem. A*, vol. 117, no. 2 (Jan. 2013), pp. 275–282. DOI: [10.1021/jp310910f](https://doi.org/10.1021/jp310910f).
- [45] Pang, G. A., Hanson, R. K., Golden, D. M., and Bowman, C. T. *J. Phys. Chem. A*, vol. 116, no. 39 (Oct. 2012), pp. 9607–9613. DOI: [10.1021/jp306977e](https://doi.org/10.1021/jp306977e).
- [46] El-Nahas, A. M., Mangood, A. H., El-Shereafy, E.-S. E., and El-Meleigy, A. B. *Fuel* (Nov. 2012), pp. 29–33. DOI: [10.1016/j.fuel.2012.10.054](https://doi.org/10.1016/j.fuel.2012.10.054).
- [47] Zhou, C.-W., Simmie, J. M., and Curran, H. J. *Combust. Flame*, vol. 158, no. 4 (Apr. 2011), pp. 726–731. DOI: [10.1016/j.combustflame.2010.11.002](https://doi.org/10.1016/j.combustflame.2010.11.002).
- [48] Moc, J. and Simmie, J. M. *J. Phys. Chem. A*, vol. 114, no. 17 (May 2010), pp. 5558–5564. DOI: [10.1021/jp1009065](https://doi.org/10.1021/jp1009065).
- [49] Vasu, S. S., Davidson, D. F., Hanson, R. K., and Golden, D. M. *Chem. Phys. Lett.*, vol. 497, no. 1-3 (Aug. 2010), pp. 26–29. DOI: [10.1016/j.cplett.2010.08.001](https://doi.org/10.1016/j.cplett.2010.08.001).
- [50] Zhou, C.-W., Simmie, J. M., and Curran, H. J. *Int. J. Chem. Kinet.*, vol. 44, no. 3 (Jan. 2012), pp. 155–164. DOI: [10.1002/kin.20708](https://doi.org/10.1002/kin.20708).

- [51] Alecu, I. M., Zheng, J., Papajak, E., Yu, T., and Truhlar, D. G. *J. Phys. Chem. A*, vol. 116, no. 50 (Dec. 2012), pp. 12206–12213. DOI: [10.1021/jp308460y](https://doi.org/10.1021/jp308460y).
- [52] Black, G. and Simmie, J. M. *J. Comput. Chem.*, vol. 31, no. 6 (Apr. 2010), pp. 1236–1248. DOI: [10.1002/jcc.21410](https://doi.org/10.1002/jcc.21410).
- [53] Katsikadakos, D., Zhou, C.-W., Simmie, J. M., Curran, H. J., Hunt, P., Hardalupas, Y., et al. *Proc. Combust. Inst.*, vol. 34, no. 1 (Jan. 2013), pp. 483–491. DOI: [10.1016/j.proci.2012.06.015](https://doi.org/10.1016/j.proci.2012.06.015).
- [54] Katsikadakos, D., Hardalupas, Y., Taylor, A., and Hunt, P. *Phys. Chem. Chem. Phys.*, vol. 14, no. 27 (July 2012), pp. 9615–9629. DOI: [10.1039/c2cp24074b](https://doi.org/10.1039/c2cp24074b).
- [55] Moss, J. T., Berkowitz, A. M., Oehlschlaeger, M. A., Biet, J., Warth, V., Glaude, P.-A., et al. *J. Phys. Chem. A*, vol. 112, no. 43 (Oct. 2008), pp. 10843–10855. DOI: [10.1021/jp806464p](https://doi.org/10.1021/jp806464p).
- [56] Black, G., Curran, H. J., Pichon, S., Simmie, J. M., and Zhukov, V. P. *Combust. Flame*, vol. 157, no. 2 (Feb. 2010), pp. 363–373. DOI: [10.1016/j.combustflame.2009.07.007](https://doi.org/10.1016/j.combustflame.2009.07.007).
- [57] Noorani, K. E., Akhi-Kumgeh, B., and Bergthorson, J. M. *Energy Fuel*, vol. 24, no. 11 (Nov. 2010), pp. 5834–5843. DOI: [10.1021/ef1009692](https://doi.org/10.1021/ef1009692).
- [58] Zhang, J., Wei, L., Man, X., Jiang, X., Zhang, Y., Hu, E., et al. *Energy Fuel*, vol. 26, no. 6 (June 2012), pp. 3368–3380. DOI: [10.1021/ef3005042](https://doi.org/10.1021/ef3005042).
- [59] Stranic, I., Chase, D. P., Harmon, J. T., Yang, S., Davidson, D. F., and Hanson, R. K. *Combust. Flame*, vol. 159, no. 2 (Feb. 2012), pp. 516–527. DOI: [10.1016/j.combustflame.2011.08.014](https://doi.org/10.1016/j.combustflame.2011.08.014).
- [60] Yasunaga, K., Mikajiri, T., Sarathy, S. M., Koike, T., Gillespie, F., Nagy, T., et al. *Combust. Flame*, vol. 159, no. 6 (June 2012), pp. 2009–2027. DOI: [10.1016/j.combustflame.2012.02.008](https://doi.org/10.1016/j.combustflame.2012.02.008).

- [61] Heufer, K. A., Fernandes, R. X., Olivier, H., Beeckmann, J., Röhl, O., and Peters, N. *Proc. Combust. Inst.*, vol. 33, no. 1 (Aug. 2011), pp. 359–366. DOI: [10.1016/j.proci.2010.06.052](https://doi.org/10.1016/j.proci.2010.06.052).
- [62] Vranckx, S., Heufer, K. A., Lee, C., Olivier, H., Schill, L., Kopp, W., et al. *Combust. Flame*, vol. 158, no. 8 (Aug. 2011), pp. 1444–1455. DOI: [10.1016/j.combustflame.2010.12.028](https://doi.org/10.1016/j.combustflame.2010.12.028).
- [63] Zhu, Y., Davidson, D. F., and Hanson, R. K. *Combust. Flame*, vol. 161, no. 3 (Mar. 2014), pp. 634–643. DOI: [10.1016/j.combustflame.2013.06.028](https://doi.org/10.1016/j.combustflame.2013.06.028).
- [64] Weber, B. W., Kumar, K., Zhang, Y., and Sung, C.-J. *Combust. Flame*, vol. 158, no. 5 (Mar. 2011), pp. 809–819. DOI: [10.1016/j.combustflame.2011.02.005](https://doi.org/10.1016/j.combustflame.2011.02.005).
- [65] Weber, B. W. and Sung, C.-J. *Energy Fuel*, vol. 27, no. 3 (Mar. 2013), pp. 1688–1698. DOI: [10.1021/ef302195c](https://doi.org/10.1021/ef302195c).
- [66] Weber, B. W., Merchant, S. S., Sung, C.-J., and Green, W. H. “An Autoignition Study of iso-Butanol: Experiments and Modeling”. In: *8th US Natl. Tech. Meet. Combust. Inst.* University of Utah. Park City, UT, May 2013, Paper 3A01.
- [67] Karwat, D. M. A., Wagnon, S. W., Teini, P. D., and Wooldridge, M. S. *J. Phys. Chem. A*, vol. 115, no. 19 (May 2011), pp. 4909–4921. DOI: [10.1021/jp200905n](https://doi.org/10.1021/jp200905n).
- [68] Cook, R. D., Davidson, D. F., and Hanson, R. K. *Int. J. Chem. Kinet.*, vol. 44, no. 5 (May 2012), pp. 303–311. DOI: [10.1002/kin.20713](https://doi.org/10.1002/kin.20713).
- [69] Stranic, I., Pyun, S. H., Davidson, D. F., and Hanson, R. K. *Combust. Flame*, vol. 159, no. 11 (Nov. 2012), pp. 3242–3250. DOI: [10.1016/j.combustflame.2012.06.005](https://doi.org/10.1016/j.combustflame.2012.06.005).
- [70] Stranic, I., Pyun, S. H., Davidson, D. F., and Hanson, R. K. *Combust. Flame*, vol. 160, no. 6 (June 2013), pp. 1012–1019. DOI: [10.1016/j.combustflame.2013.01.015](https://doi.org/10.1016/j.combustflame.2013.01.015).
- [71] Rosado-Reyes, C. M. and Tsang, W. *J. Phys. Chem. A*, vol. 116, no. 40 (Oct. 2012), pp. 9825–9831. DOI: [10.1021/jp305120h](https://doi.org/10.1021/jp305120h).

- [72] Rosado-Reyes, C. M. and Tsang, W. *J. Phys. Chem. A*, vol. 116, no. 39 (Oct. 2012), pp. 9599–606. DOI: [10.1021/jp306975s](https://doi.org/10.1021/jp306975s).
- [73] Dayma, G., Togbé, C., and Dagaut, P. *Energy Fuel*, vol. 25, no. 11 (Nov. 2011), pp. 4986–4998. DOI: [10.1021/ef2012112](https://doi.org/10.1021/ef2012112).
- [74] Togbé, C., Halter, F., Foucher, F., Mounaim-Rousselle, C., and Dagaut, P. *Proc. Combust. Inst.*, vol. 33, no. 1 (2011), pp. 367–374. DOI: [10.1016/j.proci.2010.05.003](https://doi.org/10.1016/j.proci.2010.05.003).
- [75] Sarathy, S. M., Park, S., Weber, B. W., Wang, W., Veloo, P. S., Davis, A. C., et al. *Combust. Flame*, vol. 160, no. 12 (Dec. 2013), pp. 2712–2728. DOI: [10.1016/j.combustflame.2013.06.022](https://doi.org/10.1016/j.combustflame.2013.06.022).
- [76] Welz, O., Zádor, J., Savee, J. D., Ng, M. Y., Meloni, G., Fernandes, R. X., et al. *Phys. Chem. Chem. Phys.*, vol. 14, no. 9 (Mar. 2012), pp. 3112–3127. DOI: [10.1039/c2cp23248k](https://doi.org/10.1039/c2cp23248k).
- [77] Tsujimura, T., Pitz, W. J., Gillespie, F., Curran, H. J., Weber, B. W., Zhang, Y., et al. *Energy Fuel*, vol. 26, no. 8 (Aug. 2012), pp. 4871–4886. DOI: [10.1021/ef300879k](https://doi.org/10.1021/ef300879k).
- [78] Tang, C., Wei, L., Man, X., Zhang, J., Huang, Z., and Law, C. K. *Combust. Flame*, vol. 160, no. 3 (Mar. 2013), pp. 520–529. DOI: [10.1016/j.combustflame.2012.11.018](https://doi.org/10.1016/j.combustflame.2012.11.018).
- [79] Tsujimura, T., Pitz, W. J., Yang, Y., and Dec, J. E. *Int. J. Fuels Lubr.*, vol. 4, no. 2 (Dec. 2011), pp. 257–270. DOI: [10.4271/2011-24-0023](https://doi.org/10.4271/2011-24-0023).
- [80] Yacoub, Y., Bata, R. M., and Gautam, M. *Proc. Inst. Mech. Eng. Part A J. Power Energy*, vol. 212, no. 5 (Jan. 1998), pp. 363–379. DOI: [10.1243/0957650981536934](https://doi.org/10.1243/0957650981536934).
- [81] Yang, Y., Dec, J. E., Droniou, N., and Simmons, B. A. *Int. J. Fuels Lubr.*, vol. 3, no. 2 (2010), pp. 725–741. DOI: [10.4271/2010-01-2164](https://doi.org/10.4271/2010-01-2164).
- [82] Rotavera, B. and Petersen, E. L. *Proc. Combust. Inst.*, vol. 34, no. 1 (Jan. 2013), pp. 435–442. DOI: [10.1016/j.proci.2012.06.042](https://doi.org/10.1016/j.proci.2012.06.042).
- [83] Vasu, S. S., Davidson, D. F., and Hanson, R. K. *Combust. Flame*, vol. 156, no. 4 (Apr. 2009), pp. 736–749. DOI: [10.1016/j.combustflame.2008.09.006](https://doi.org/10.1016/j.combustflame.2008.09.006).

- [84] Vanderover, J. and Oehlschlaeger, M. A. *Int. J. Chem. Kinet.*, vol. 41, no. 2 (Feb. 2009), pp. 82–91. DOI: [10.1002/kin.20370](https://doi.org/10.1002/kin.20370).
- [85] Hawthorn, R. D. and Nixon, A. C. *AIAA J.*, vol. 4, no. 3 (Mar. 1966), pp. 513–520. DOI: [10.2514/3.3466](https://doi.org/10.2514/3.3466).
- [86] Orme, J., Curran, H. J., and Simmie, J. M. *J. Phys. Chem. A*, vol. 110, no. 1 (Jan. 2006), pp. 114–131. DOI: [10.1021/jp0543678](https://doi.org/10.1021/jp0543678).
- [87] Hong, Z., Lam, K.-Y., Davidson, D. F., and Hanson, R. K. *Combust. Flame*, vol. 158, no. 8 (Aug. 2011), pp. 1456–1468. DOI: [10.1016/j.combustflame.2010.12.019](https://doi.org/10.1016/j.combustflame.2010.12.019).
- [88] Tanaka, S., Ayala, F., Keck, J. C., and Heywood, J. B. *Combust. Flame*, vol. 132, no. 1-2 (Jan. 2003), pp. 219–239. DOI: [10.1016/S0010-2180\(02\)00457-1](https://doi.org/10.1016/S0010-2180(02)00457-1).
- [89] Mittal, G. and Sung, C.-J. *Combust. Flame*, vol. 156, no. 9 (Sept. 2009), pp. 1852–1855. DOI: [10.1016/j.combustflame.2009.05.009](https://doi.org/10.1016/j.combustflame.2009.05.009).
- [90] Das, A. K., Sung, C.-J., Zhang, Y., and Mittal, G. *Int. J. Hydrogen Energy*, vol. 37, no. 8 (Apr. 2012), pp. 6901–6911. DOI: [10.1016/j.ijhydene.2012.01.111](https://doi.org/10.1016/j.ijhydene.2012.01.111).
- [91] Uddi, M., Das, A. K., and Sung, C.-J. *Appl. Opt.*, vol. 51, no. 22 (Aug. 2012), pp. 5464–5476. URL: <http://www.ncbi.nlm.nih.gov/pubmed/22859037>.
- [92] Mittal, G. and Sung, C.-J. *Combust. Sci. Technol.*, vol. 179, no. 3 (2007), pp. 497–530. DOI: [10.1080/00102200600671898](https://doi.org/10.1080/00102200600671898).
- [93] Mittal, G. “A Rapid Compression Machine - Design, Characterization, and Autoignition Investigations”. Dissertation. Case Western Reserve University, 2006. URL: http://etd.ohiolink.edu/send-pdf.cgi/Mittal%20Gaurav.pdf?acc%5C_num=case1130184196.
- [94] Kumar, K., Mittal, G., and Sung, C.-J. *Combust. Flame*, vol. 156, no. 6 (June 2009), pp. 1278–1288. DOI: [10.1016/j.combustflame.2009.01.009](https://doi.org/10.1016/j.combustflame.2009.01.009).

- [95] Das, A. K., Uddi, M., and Sung, C.-J. *Combust. Flame*, vol. 159, no. 12 (Dec. 2012), pp. 3493–3501. DOI: [10.1016/j.combustflame.2012.06.020](https://doi.org/10.1016/j.combustflame.2012.06.020).
- [96] Mittal, G., Sung, C.-J., and Yetter, R. A. *Int. J. Chem. Kinet.*, vol. 38, no. 8 (2006), pp. 516–529. DOI: [10.1002/kin.20180](https://doi.org/10.1002/kin.20180).
- [97] Mittal, G., Chaos, M., Sung, C.-J., and Dryer, F. L. *Fuel Process. Technol.*, vol. 89, no. 12 (Dec. 2008), pp. 1244–1254. DOI: [10.1016/j.fuproc.2008.05.021](https://doi.org/10.1016/j.fuproc.2008.05.021).
- [98] Kumar, K. and Sung, C.-J. *Int. J. Chem. Kinet.*, vol. 43, no. 4 (Apr. 2011), pp. 175–184. DOI: [10.1002/kin.20546](https://doi.org/10.1002/kin.20546).
- [99] Mittal, G. and Sung, C.-J. *Combust. Flame*, vol. 150, no. 4 (2007), pp. 355–368. DOI: [10.1016/j.combustflame.2007.04.014](https://doi.org/10.1016/j.combustflame.2007.04.014).
- [100] Mittal, G. and Sung, C.-J. *Combust. Flame*, vol. 155, no. 3 (Nov. 2008), pp. 431–439. DOI: [10.1016/j.combustflame.2008.05.003](https://doi.org/10.1016/j.combustflame.2008.05.003).
- [101] Kumar, K. and Sung, C.-J. *Combust. Flame*, vol. 157, no. 4 (Apr. 2010), pp. 676–685. DOI: [10.1016/j.combustflame.2010.01.001](https://doi.org/10.1016/j.combustflame.2010.01.001).
- [102] Dooley, S., Won, S. H., Chaos, M., Heyne, J. S., Ju, Y., Dryer, F. L., et al. *Combust. Flame*, vol. 157, no. 12 (Dec. 2010), pp. 2333–2339. DOI: [10.1016/j.combustflame.2010.07.001](https://doi.org/10.1016/j.combustflame.2010.07.001).
- [103] Hui, X., Kumar, K., Sung, C.-J., Edwards, T., and Gardner, D. *Fuel*, vol. 98 (Aug. 2012), pp. 176–182. DOI: [10.1016/j.fuel.2012.03.040](https://doi.org/10.1016/j.fuel.2012.03.040).
- [104] Kéromnès, A., Metcalfe, W. K., Heufer, K. A., Donohoe, N., Das, A. K., Sung, C.-J., et al. *Combust. Flame*, vol. 160 (Mar. 2013), pp. 995–1011. DOI: [10.1016/j.combustflame.2013.01.001](https://doi.org/10.1016/j.combustflame.2013.01.001).
- [105] Kukkadapu, G., Kumar, K., Sung, C.-J., Mehl, M., and Pitz, W. J. *Proc. Combust. Inst.*, vol. 34, no. 1 (Jan. 2013), pp. 345–352. DOI: [10.1016/j.proci.2012.06.135](https://doi.org/10.1016/j.proci.2012.06.135).

- [106] Kukkadapu, G., Kumar, K., Sung, C.-J., Mehl, M., and Pitz, W. J. *Combust. Flame*, vol. 159, no. 10 (Oct. 2012), pp. 3066–3078. DOI: [10.1016/j.combustflame.2012.05.008](https://doi.org/10.1016/j.combustflame.2012.05.008).
- [107] Yaws, C. *Chemical Properties Handbook*. 1999. URL: http://knovel.com/web/portal/browse/display?%5C_EXT%5C_KNOVEL%5C_DISPLAY%5C_bookid=49%5C&VerticalID=0.
- [108] Lee, D. and Hochgreb, S. *Combust. Flame*, vol. 114, no. 3-4 (Aug. 1998), pp. 531–545. DOI: [10.1016/S0010-2180\(97\)00327-1](https://doi.org/10.1016/S0010-2180(97)00327-1).
- [109] Mittal, G. and Sung, C.-J. *Combust. Flame*, vol. 145, no. 1-2 (Apr. 2006), pp. 160–180. DOI: [10.1016/j.combustflame.2005.10.019](https://doi.org/10.1016/j.combustflame.2005.10.019).
- [110] Desgroux, P., Gasnot, L., and Sochet, L. R. *Appl. Phys. B Laser Opt.*, vol. 61, no. 1 (July 1995), pp. 69–72. DOI: [10.1007/BF01090974](https://doi.org/10.1007/BF01090974).
- [111] *CHEMKIN-PRO*. San Diego, 2013.
- [112] Corless, R. M., Gonnet, G. H., Hare, D. E. G., Jeffrey, D. J., and Knuth, D. E. *Adv. Comput. Math.*, vol. 5, no. 1 (Dec. 1996), pp. 329–359. DOI: [10.1007/BF02124750](https://doi.org/10.1007/BF02124750).
- [113] Taylor, J. R. *An Introduction to Error Analysis*. Mill Valley, CA, 1982.
- [114] Dalton, J. *A Journal of Natural Philosophy, Chemistry, and the Arts*, vol. 5 (Oct. 1801), pp. 241–244. URL: <https://archive.org/details/journalofnatural04lond>.
- [115] Gillespie, L. *Phys. Rev.*, vol. 36, no. 1 (July 1930), pp. 121–131. DOI: [10.1103/PhysRev.36.121](https://doi.org/10.1103/PhysRev.36.121).
- [116] York, D., Evensen, N. M., Martínez, M. L., and De Basabe Delgado, J. *Am. J. Phys.*, vol. 72, no. 3 (Mar. 2004), pp. 367–375. DOI: [10.1119/1.1632486](https://doi.org/10.1119/1.1632486).
- [117] Sparkman, O. D., Penton, Z. E., and Kitson, F. G. *Gas Chromatography and Mass Spectrometry: A Practical Guide* (2011), pp. 15–83. DOI: [10.1016/b978-0-12-373628-4.00002-2](https://doi.org/10.1016/b978-0-12-373628-4.00002-2).

- [118] Sparkman, O. D., Penton, Z. E., and Kitson, F. G. *Gas Chromatography and Mass Spectrometry: A Practical Guide* (2011), pp. 89–148. DOI: [10.1016/b978-0-12-373628-4.00004-6](https://doi.org/10.1016/b978-0-12-373628-4.00004-6).
- [119] Sarathy, S. M., Vranckx, S., Yasunaga, K., Mehl, M., Oßwald, P., Metcalfe, W. K., et al. *Combust. Flame*, vol. 159, no. 6 (June 2012), pp. 2028–2055. DOI: [10.1016/j.combustflame.2011.12.017](https://doi.org/10.1016/j.combustflame.2011.12.017).
- [120] Merchant, S. S., Zanoelo, E. F., Speth, R. L., Harper, M. R., Van Geem, K. M., and Green, W. H. *Combust. Flame*, vol. 160, no. 10 (Oct. 2013), pp. 1907–1929. DOI: [10.1016/j.combustflame.2013.04.023](https://doi.org/10.1016/j.combustflame.2013.04.023).
- [121] Frassoldati, A., Grana, R., Faravelli, T., Ranzi, E., Oßwald, P., and Kohse-Höinghaus, K. *Combust. Flame*, vol. 159, no. 7 (July 2012), pp. 2295–2311. DOI: [10.1016/j.combustflame.2012.03.002](https://doi.org/10.1016/j.combustflame.2012.03.002).
- [122] Welz, O., Savee, J. D., Eskola, A. J., Sheps, L., Osborn, D. L., and Taatjes, C. A. *Proc. Combust. Inst.*, vol. 34, no. 1 (June 2013), pp. 493–500. DOI: [10.1016/j.proci.2012.05.058](https://doi.org/10.1016/j.proci.2012.05.058).
- [123] Silva, G. da, Bozzelli, J. W., Liang, L., and Farrell, J. T. *J. Phys. Chem. A*, vol. 113, no. 31 (Aug. 2009), pp. 8923–8933. DOI: [10.1021/jp903210a](https://doi.org/10.1021/jp903210a).
- [124] Heufer, K. A., Sarathy, S. M., Curran, H. J., Davis, A. C., Westbrook, C. K., and Pitz, W. J. *Energy Fuel*, vol. 26, no. 11 (Oct. 2012), pp. 6678–6685. DOI: [10.1021/ef3012596](https://doi.org/10.1021/ef3012596).
- [125] Welz, O., Klippenstein, S. J., Harding, L. B., Taatjes, C. A., and Zádor, J. *J. Phys. Chem. Lett.*, vol. 4, no. 3 (Feb. 2013), pp. 350–354. DOI: [10.1021/jz302004w](https://doi.org/10.1021/jz302004w).
- [126] Ray, D. and Waddington, D. *Combust. Flame*, vol. 20, no. 3 (June 1973), pp. 327–334. DOI: [10.1016/0010-2180\(73\)90024-2](https://doi.org/10.1016/0010-2180(73)90024-2).
- [127] Sway, M. I. and Waddington, D. *J. Chem. Soc. Perkin Trans. 2*, no. 2 (1983), p. 139. DOI: [10.1039/p29830000139](https://doi.org/10.1039/p29830000139).

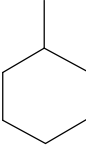
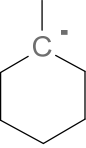
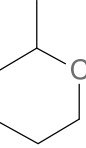
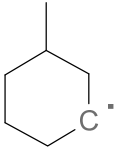
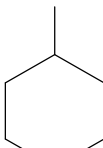
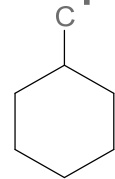
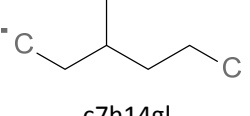
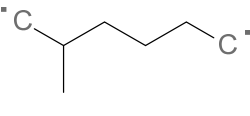
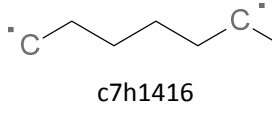
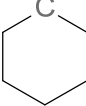
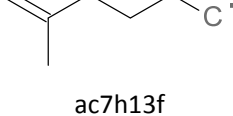
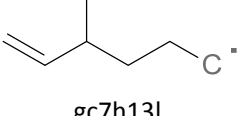
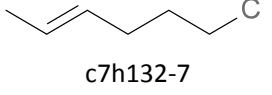
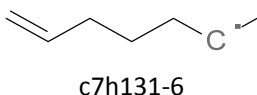
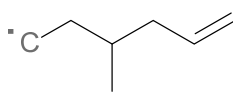
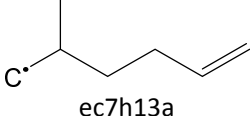
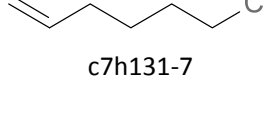
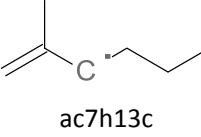
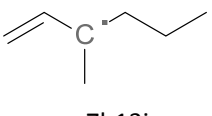
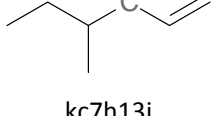
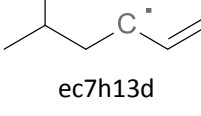
- [128] Weber, B. W., Pitz, W. J., Mehl, M., Silke, E. J., Davis, A. C., and Sung, C.-J. *Combust. Flame* (Feb. 2014), pp. 1–12. DOI: [10.1016/j.combustflame.2014.01.018](https://doi.org/10.1016/j.combustflame.2014.01.018).
- [129] Nakamura, H., Darcy, D., Mehl, M., Tobin, C. J., Metcalfe, W. K., Pitz, W. J., et al. *Combust. Flame*, vol. 161, no. 1 (Jan. 2014), pp. 49–64. DOI: [10.1016/j.combustflame.2013.08.002](https://doi.org/10.1016/j.combustflame.2013.08.002).
- [130] Silke, E. J., Pitz, W. J., Westbrook, C. K., and Ribaucour, M. *J. Phys. Chem. A*, vol. 111, no. 19 (May 2007), pp. 3761–3775. DOI: [10.1021/jp067592d](https://doi.org/10.1021/jp067592d).
- [131] Sivaramakrishnan, R. and Michael, J. *Combust. Flame*, vol. 156, no. 5 (May 2009), pp. 1126–1134. DOI: [10.1016/j.combustflame.2008.10.010](https://doi.org/10.1016/j.combustflame.2008.10.010).
- [132] Sarathy, S. M., Westbrook, C. K., Mehl, M., Pitz, W. J., Togbé, C., Dagaut, P., et al. *Combust. Flame*, vol. 158, no. 12 (Dec. 2011), pp. 2338–2357. DOI: [10.1016/j.combustflame.2011.05.007](https://doi.org/10.1016/j.combustflame.2011.05.007).
- [133] Pitz, W. J., Skeen, S. A., Mehl, M., Hansen, N., and Silke, E. J. “Chemical Kinetic Modeling of Low Pressure Methycyclohexane Flames”. In: *8th US Natl. Tech. Meet. Combust. Inst.* University of Utah. Park City, UT, May 2013, Paper 1B12.
- [134] Fernandes, R. X., Zádor, J., Jusinski, L. E., Miller, J. A., and Taatjes, C. A. *Phys. Chem. Chem. Phys.*, vol. 11, no. 9 (Mar. 2009), pp. 1320–1327. DOI: [10.1039/b819825j](https://doi.org/10.1039/b819825j).
- [135] Curran, H. J., Gaffuri, P., Pitz, W. J., and Westbrook, C. K. *Combust. Flame*, vol. 129, no. 3 (May 2002), pp. 253–280. DOI: [10.1016/S0010-2180\(01\)00373-X](https://doi.org/10.1016/S0010-2180(01)00373-X).
- [136] Zádor, J., Taatjes, C. A., and Fernandes, R. X. *Prog. Energy Combust. Sci.*, vol. 37, no. 4 (Aug. 2011), pp. 371–421. DOI: [10.1016/j.pecs.2010.06.006](https://doi.org/10.1016/j.pecs.2010.06.006).
- [137] Aguilera-Iparraguirre, J., Curran, H. J., Klopper, W., and Simmie, J. M. *J. Phys. Chem. A*, vol. 112, no. 30 (July 2008), pp. 7047–54. DOI: [10.1021/jp8012464](https://doi.org/10.1021/jp8012464).

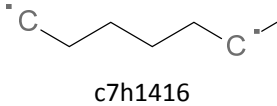
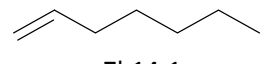
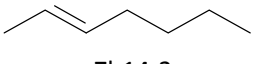
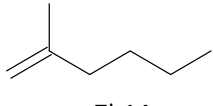
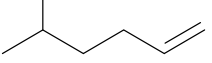
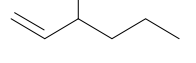
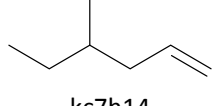
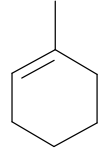
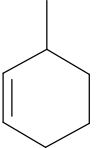
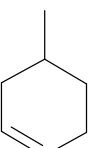
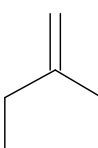
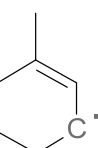
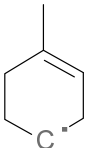
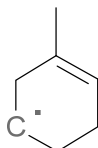
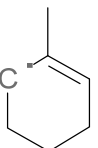
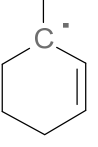
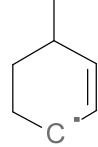
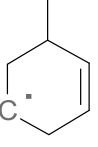
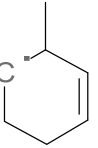
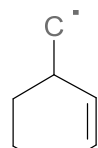
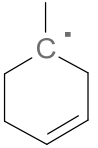
Appendix A

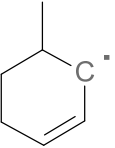
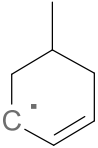
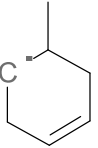
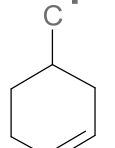
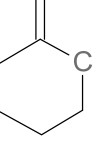
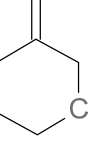
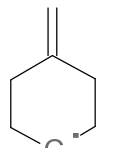
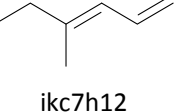
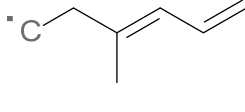
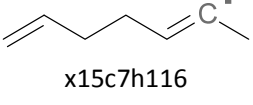
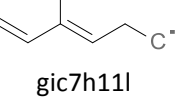
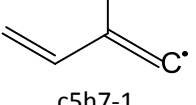
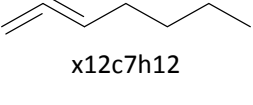
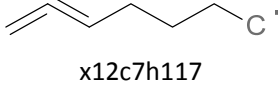
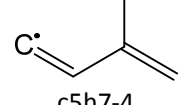
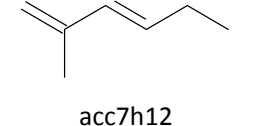
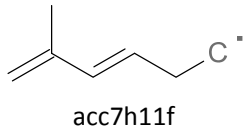
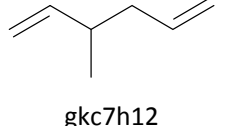
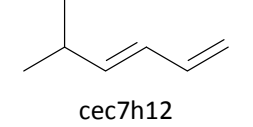
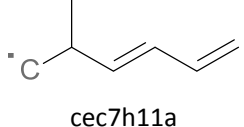
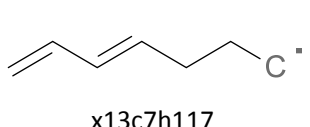
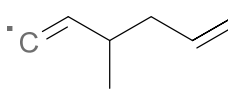
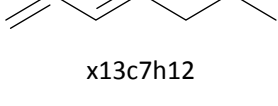
Definition of Species Names in the Methylcyclohexane Mechanism

The following is also available as supplemental material to the associated article [128]. It was generated by Dr. William J. Pitz, Lawrence Livermore National Laboratory.

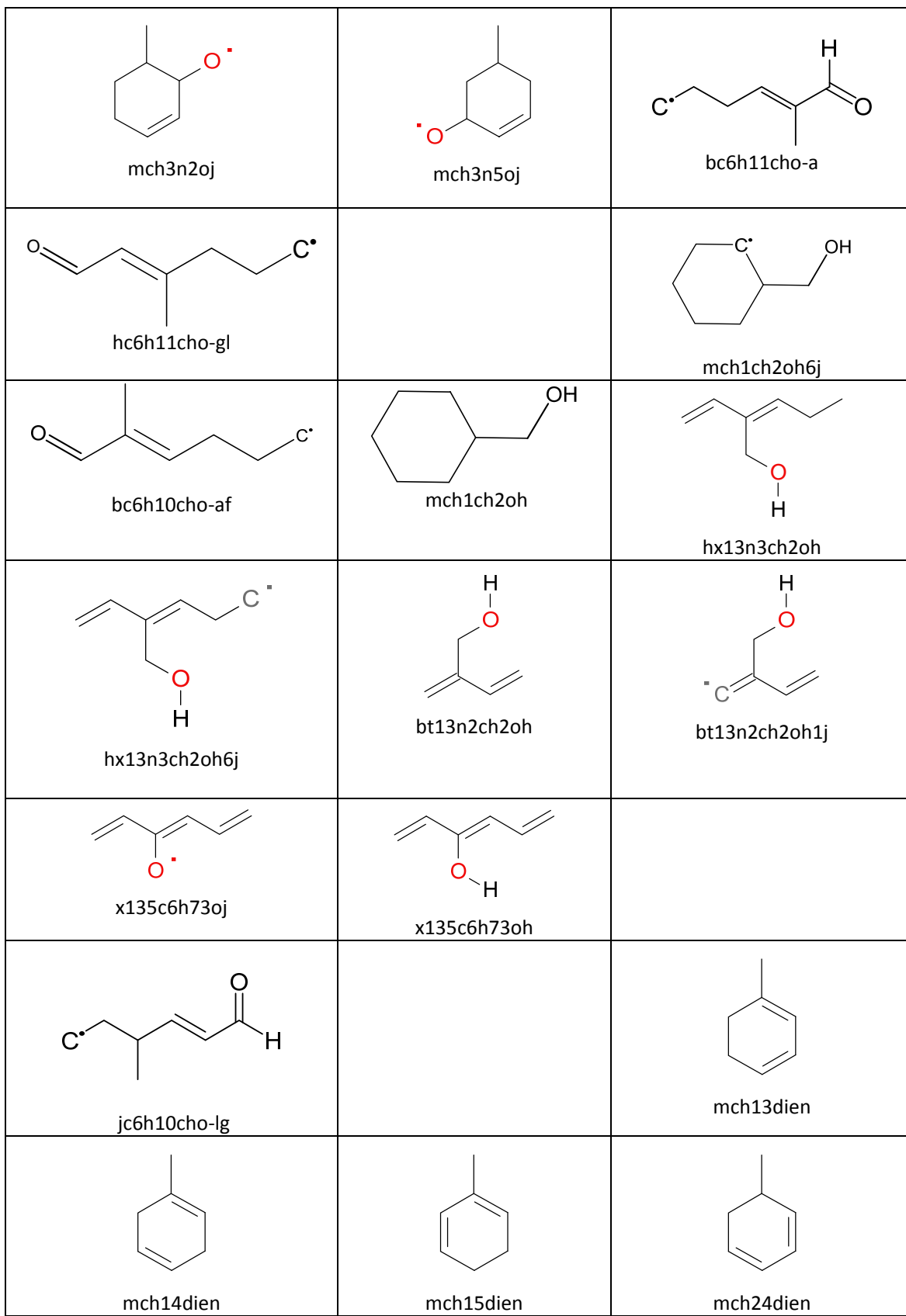
MCH species dictionary

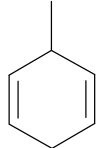
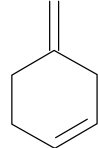
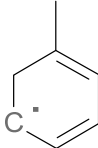
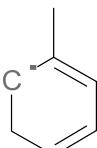
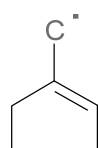
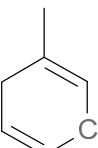
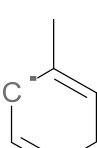
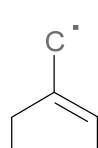
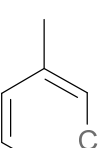
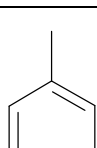
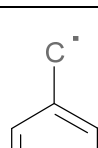
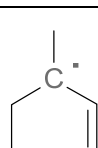
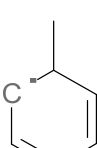
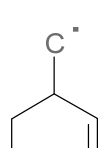
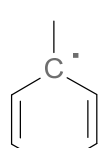
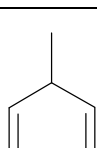
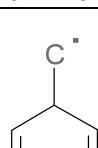
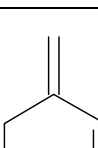
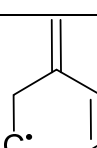
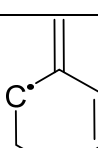
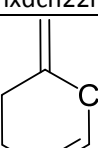
 mch	 mchr1	 mchr2
 mchr3	 mchr4	 cyhexch2
 c7h14gl	 c7h14af	 c7h1416
 chxrad	 ac7h13f	 gc7h13l
 c7h132-7	 c7h131-6	 kc7h13g
 ec7h13a	 c7h131-7	 ac7h13c
 gc7h13i	 kc7h13j	 ec7h13d

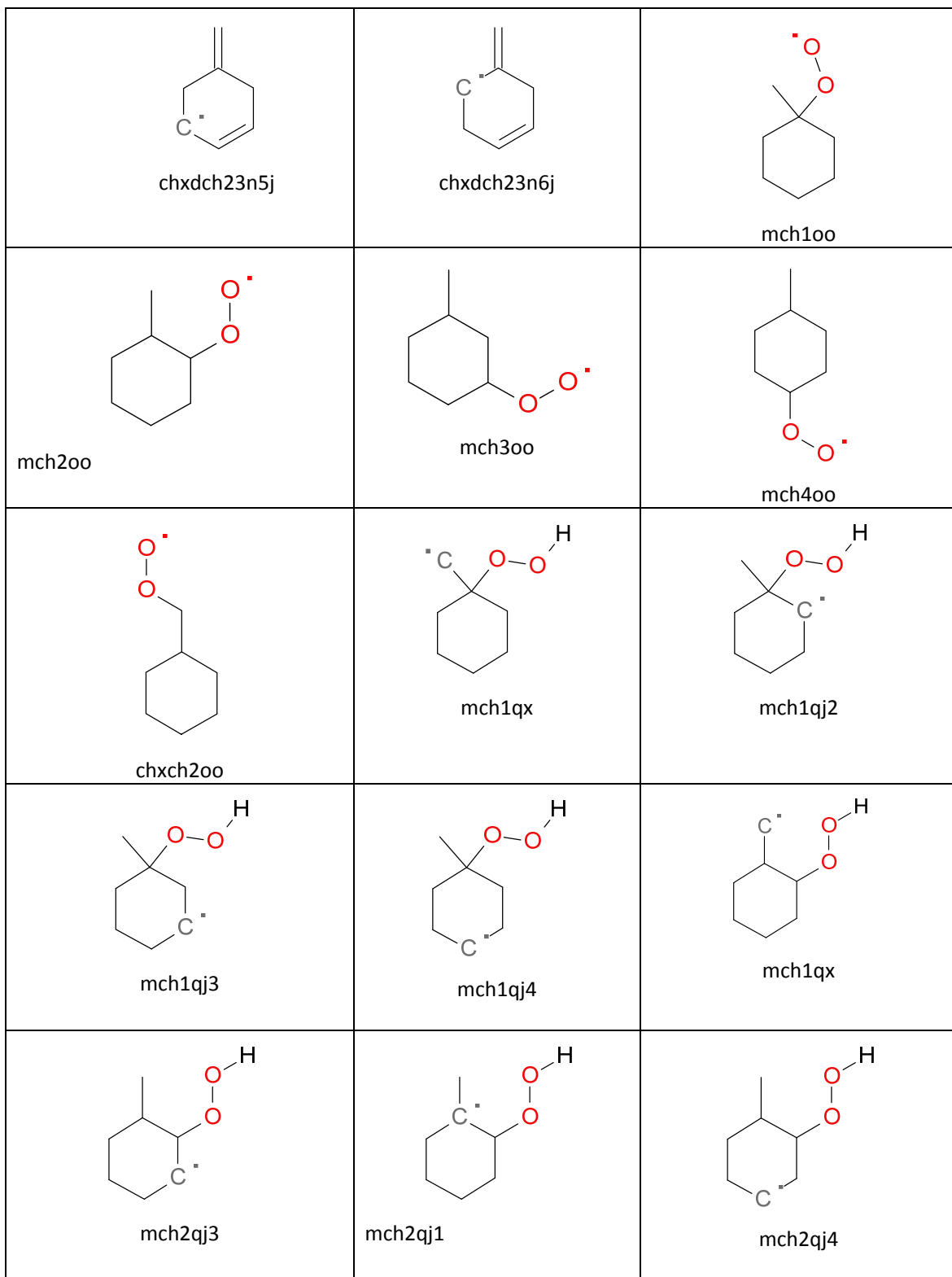
 c7h1416	 c7h14-1	 c7h14-2
 ac7h14	 ec7h14	 gc7h14
 kc7h14	 mch1ene	 mch2ene
 mch3ene	 chxdch2	 mch1n3j
 mch1n4j	 mch1n5j	 mch1n6j
 mch2n1j	 mch2n4j	 mch2n5j
 mch2n6j	 mch2nch2j	 mch3n1j

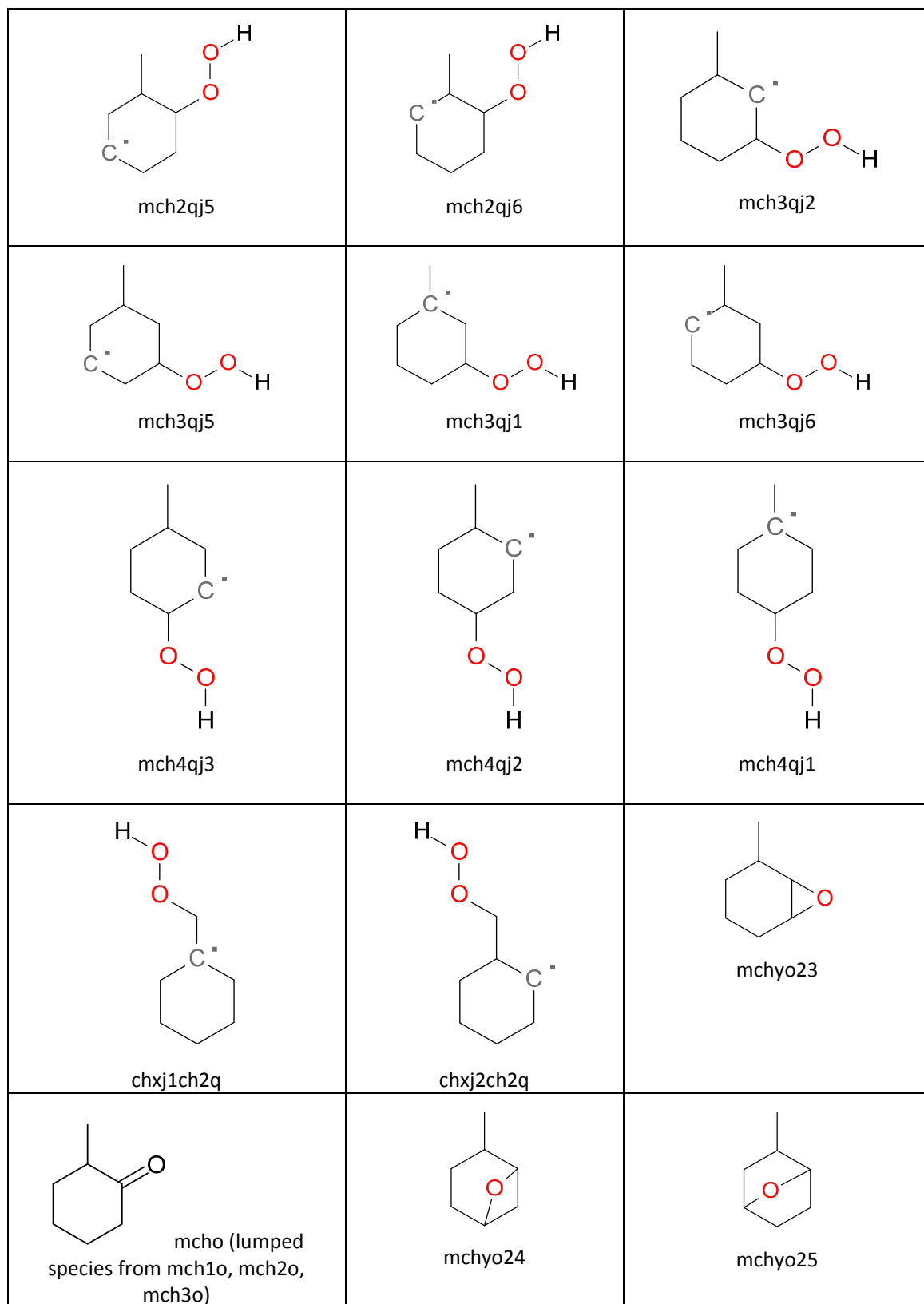
 mch3n2j	 mch3n5j	 mch3n6j
 mch3nch2j	 chxdch22j	 chxdch23j
 chxdch24j	 ikc7h12	 ikc7h11g
 x15c7h116	 gic7h11l	 c5h7-1
 x12c7h12	 x12c7h117	 c5h7-4
 acc7h12	 acc7h11f	 gkc7h12
 cec7h12	 cec7h11a	 x13c7h117
 gkc7h11g	 x13c7h12	

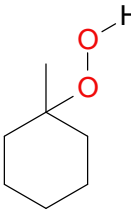
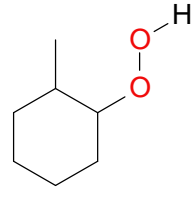
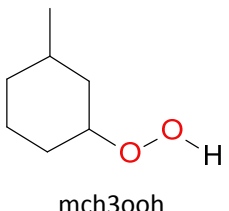
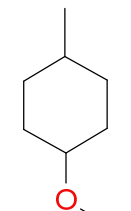
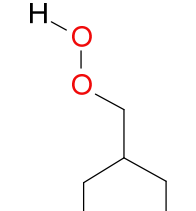
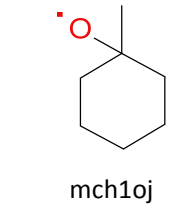
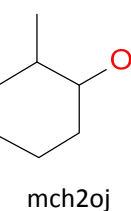
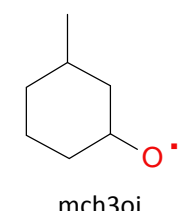
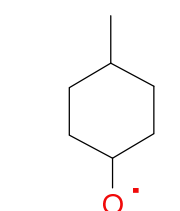
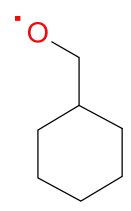
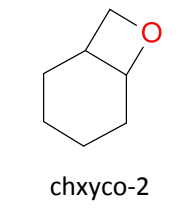
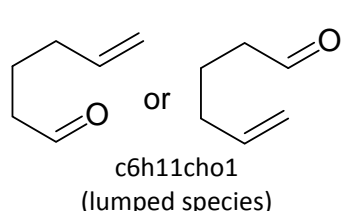
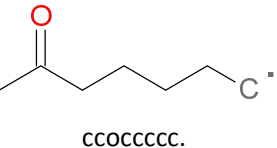
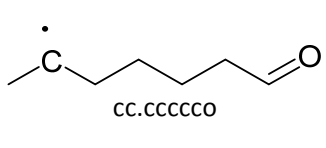
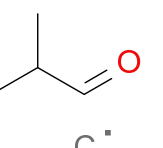
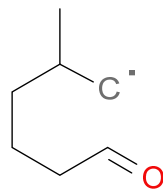
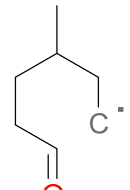
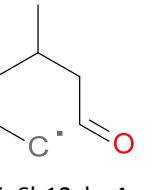
 x13c7h116	 x24c7h12	 x14c7h12
 x24c7h117	 c5h713-1	 c5h714-3
 x14c7h117	 c5h81-4	 gmc7h12
 c5h714-1	 c5h714-4	 kmc7h11g
 gmc7h11l	 kmc7h12	 aec7h12
 x16c7h12	 x16c7h112	 mch1n6oj
 aec7h11a	 mch1n3oj	 mch2n4oj
 mch1nch2oj	 mch2n1oj	 chxdch22oj

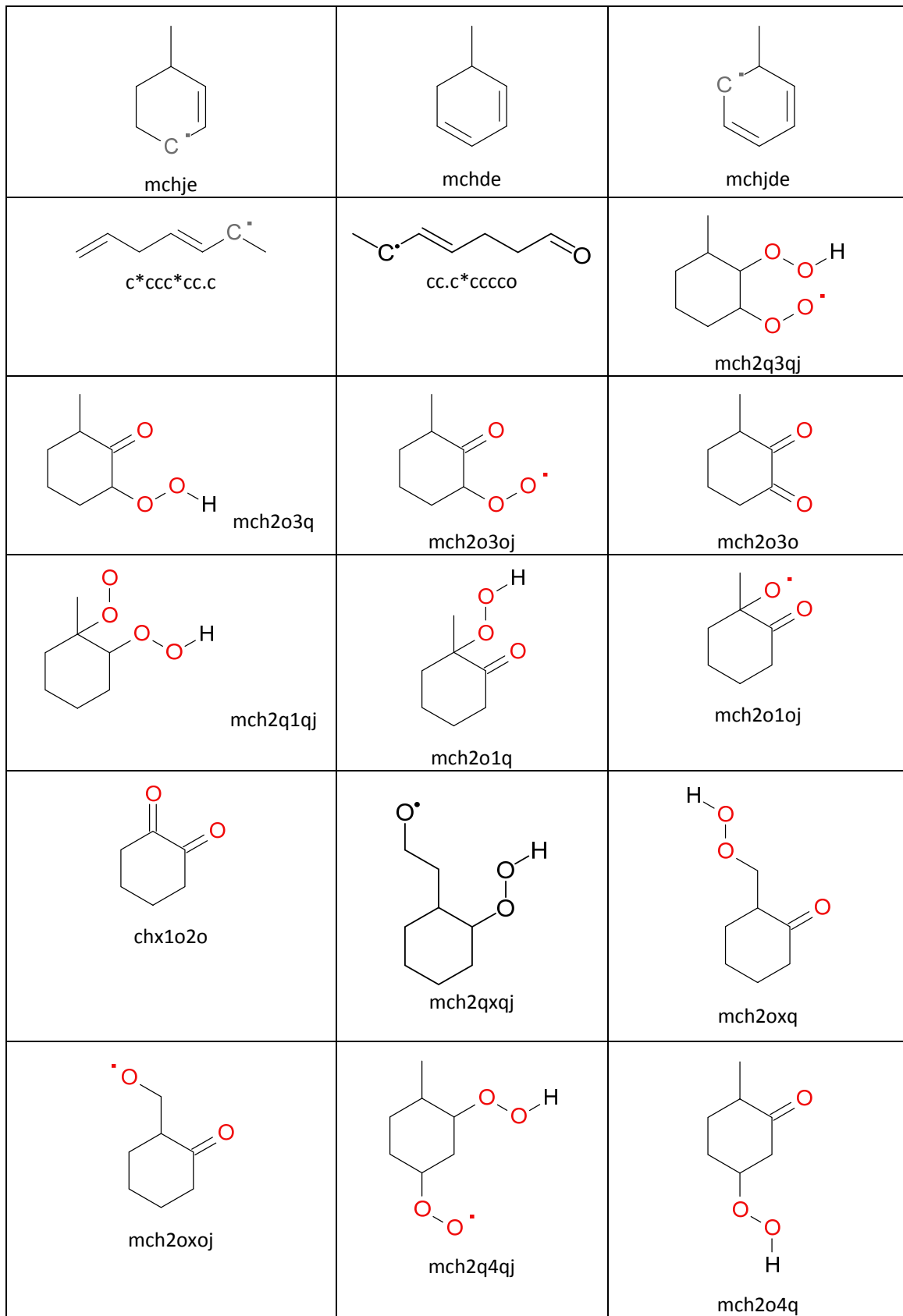


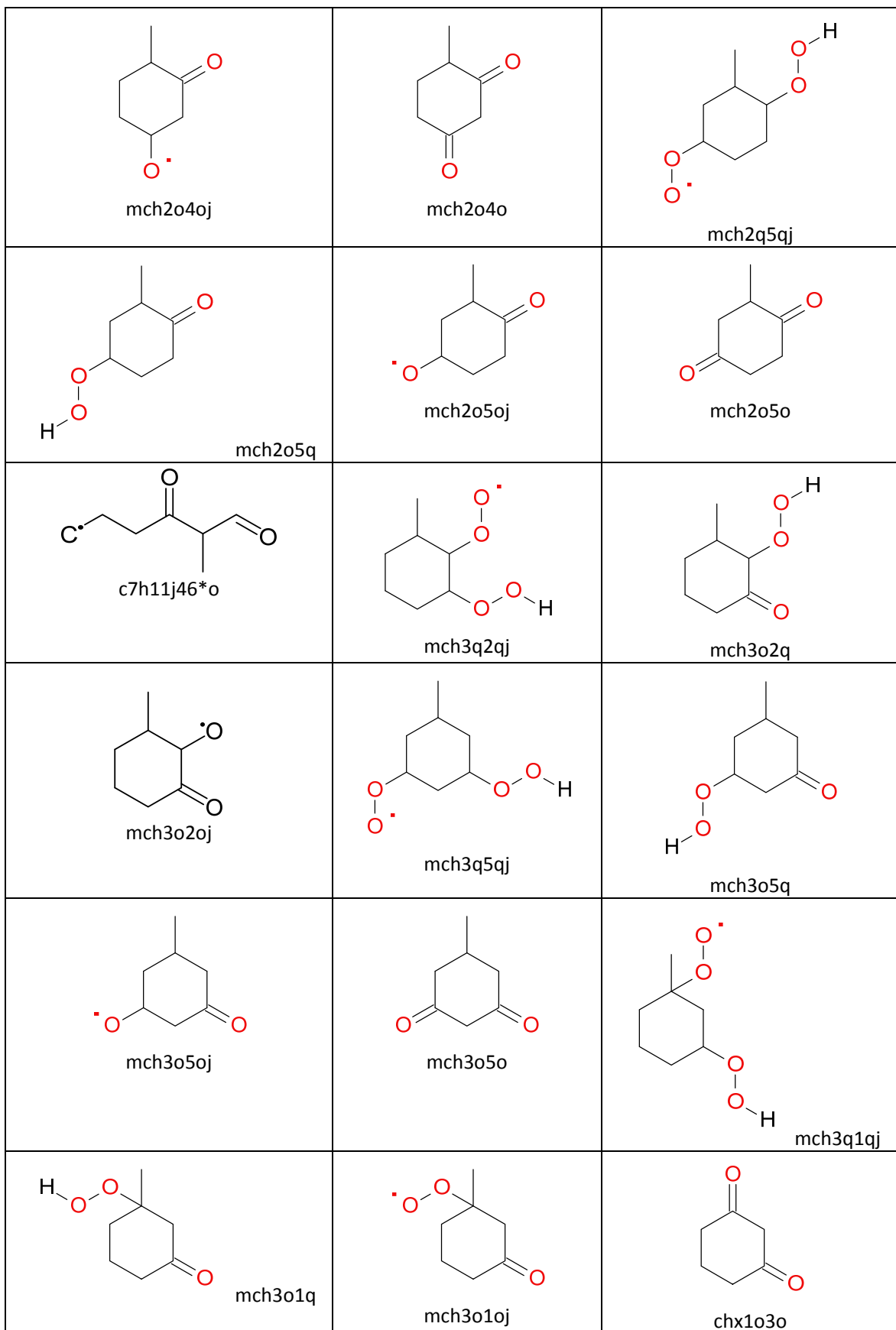
		
		
		
		
		
		
		

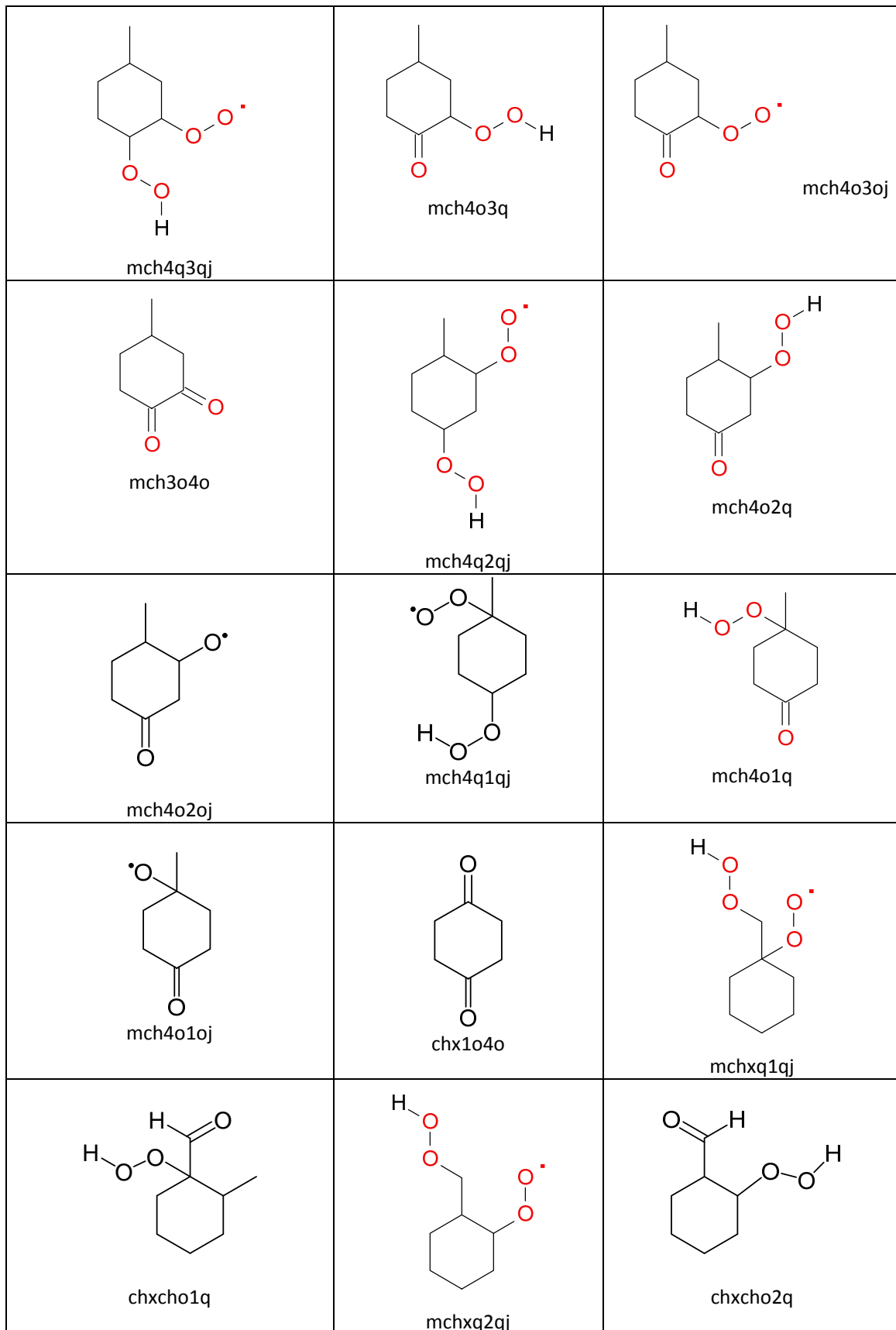


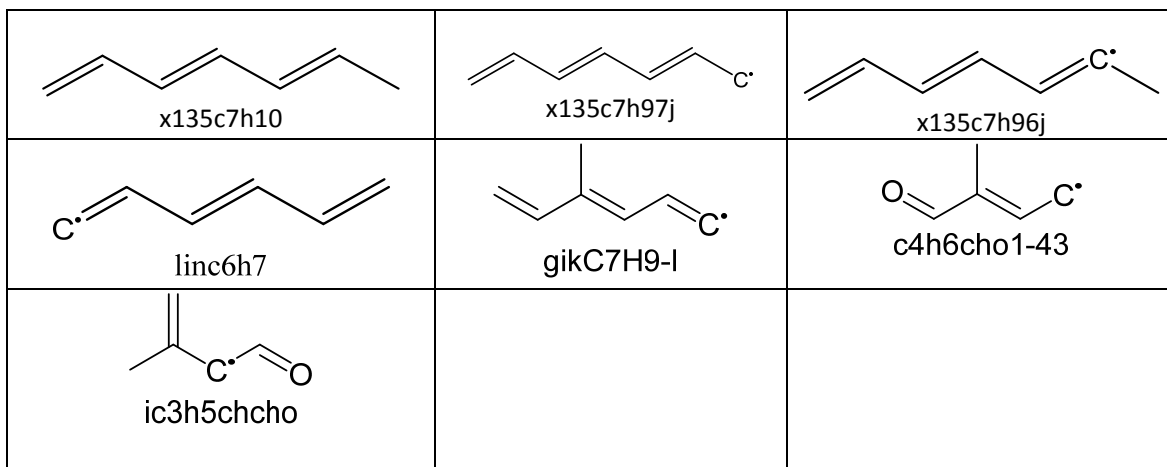


 mch1ooh	 mch2ooh	 mch3ooh
 mch4ooh	 chxch2ooh	 mch1oj
 mch2oj	 mch3oj	 mch4oj
 chxch2oj	 chxyco-2	 c6h11cho1 (lumped species)
 ccocccccc.	 cc.cccccco	 ic6h12cho5
 ic6h12cho2	 ic6h12cho3	 ic6h12cho4

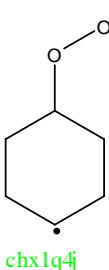
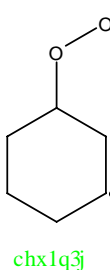
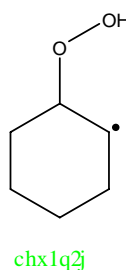
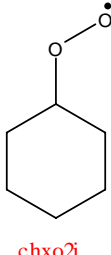
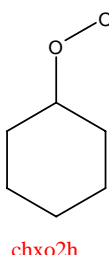
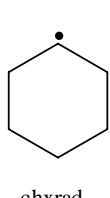
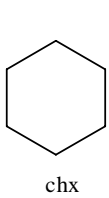






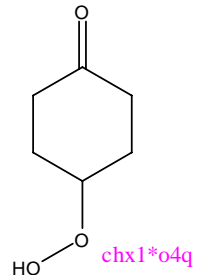
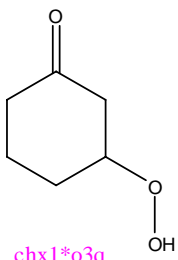
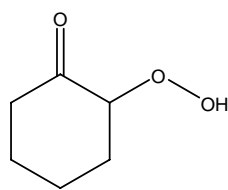
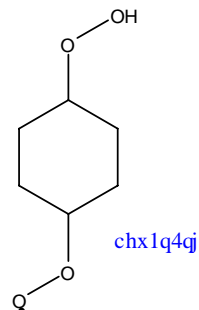
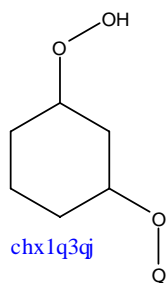
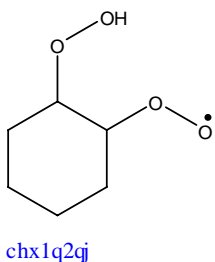


Species Glossary of Species Important at Low Temperature for CHX (Cyclohexane)



Colour highlights major species according to the Low Temperature Rxn Scheme
 RH & R·
 RO₂
 ·OOH
 ·QOOH
 O₂QOOH
 Keto

where Q = -OOH
 J = radical site



Naming Conventions

chx = cyclohexane structure

hx, h, or hex = hexane structure

q = OOH structure

al = carbonyl group

ene or n = C-C double bond

* = double bond

j = radical site

yoi_j = oxygen containing ring connected on the i and j carbon

bt or but = n-butane structure

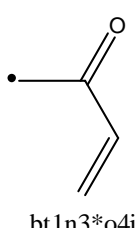
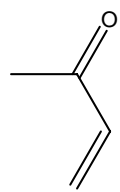
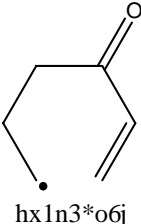
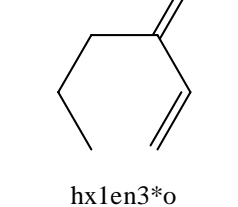
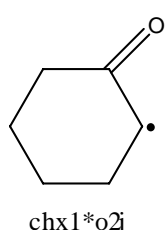
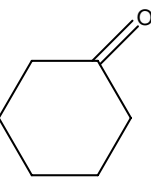
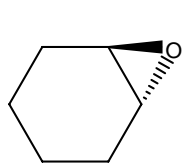
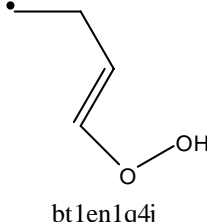
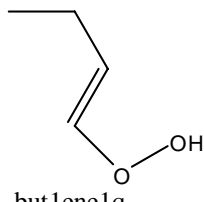
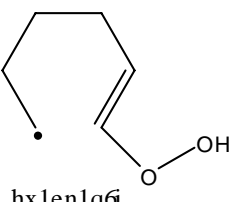
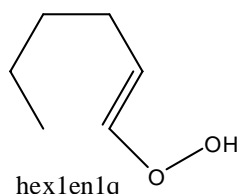
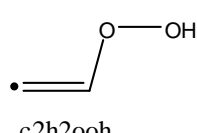
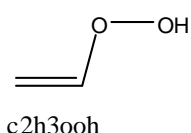
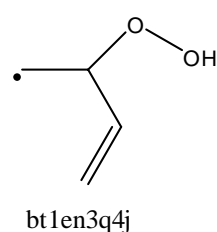
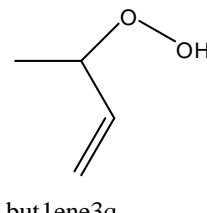
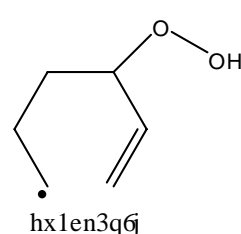
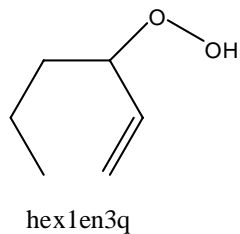
dial = di-aldehyde species specifically -C=O group

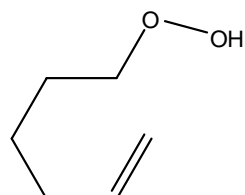
ol = alcohol group

pro = propane structure

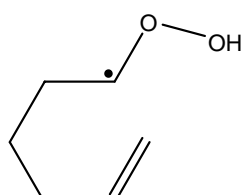
Species_glos_all.doc

QOOH decomposition routes:
The structure and naming of new species formed via these channels

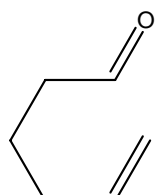




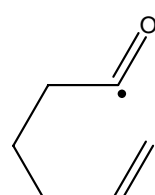
hex1en6q



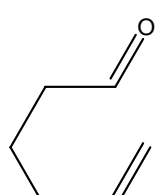
hx1en6q6j



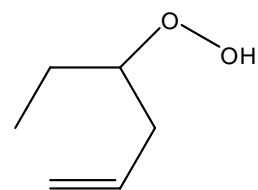
hex5enal



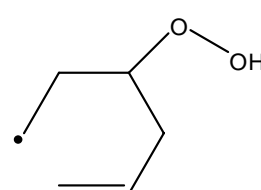
hx5enallj



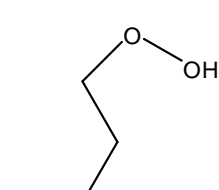
hx5enal4j



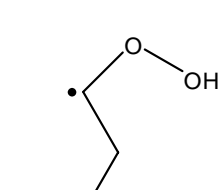
hex1en4q



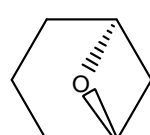
hx1en4q6j



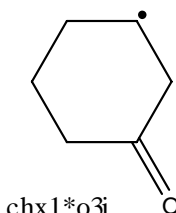
but1ene4q



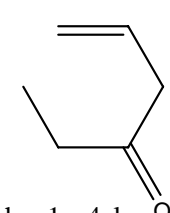
bt1en4q4j



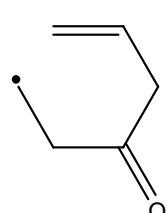
chxyo13



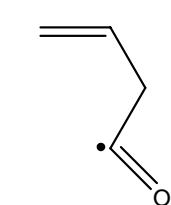
chx1*o3j



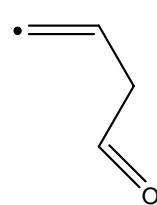
hex1en4al



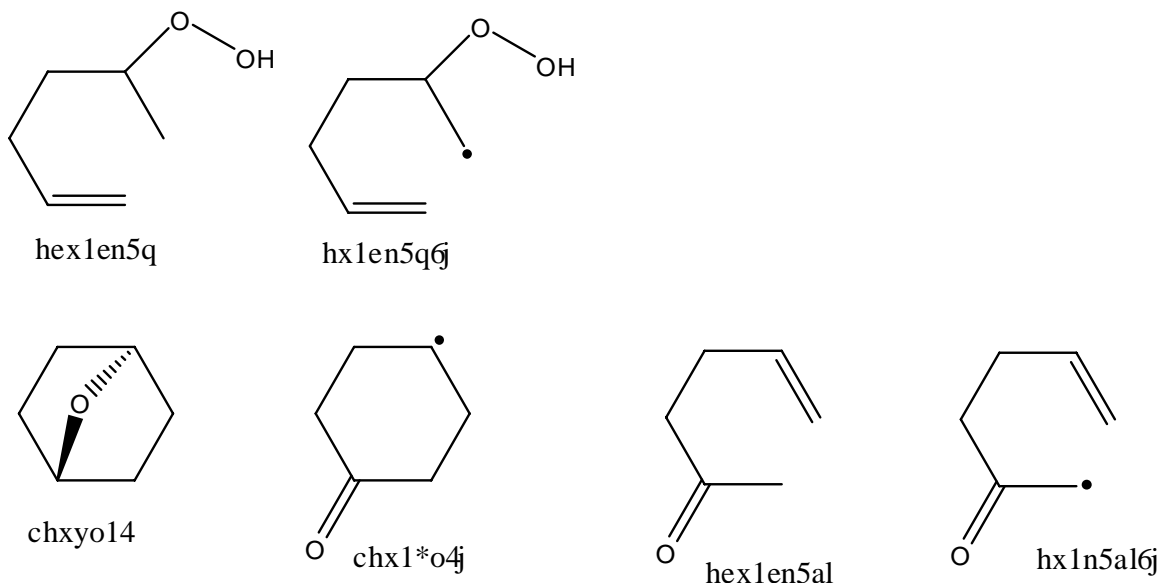
hxen4al6j



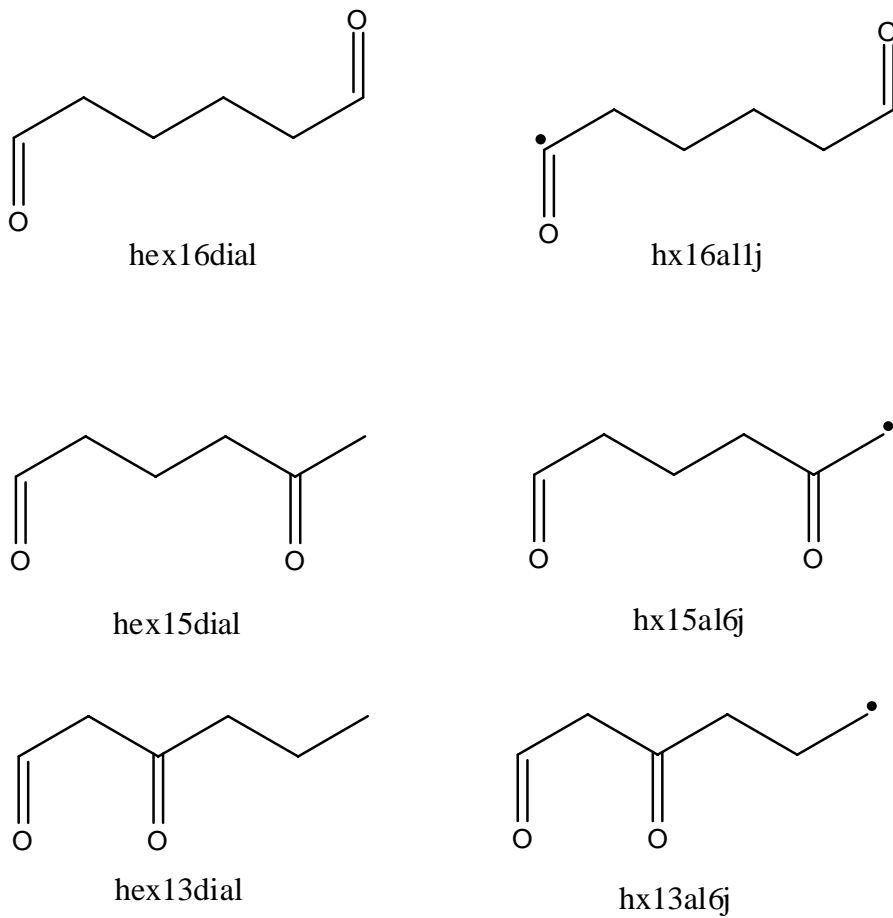
ac3h5c*o4

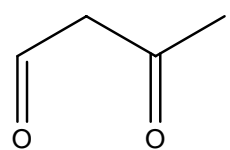


ac3h4cho1

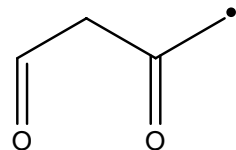


Decomposition of Ketohydroperoxides :
 The structure and naming of new species formed via these channels

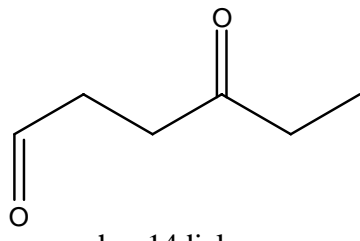




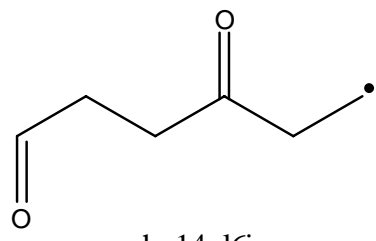
but13dial



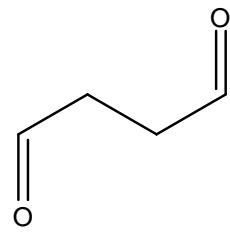
bt13al4j



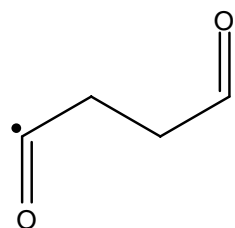
hex14dial



hx14al6j

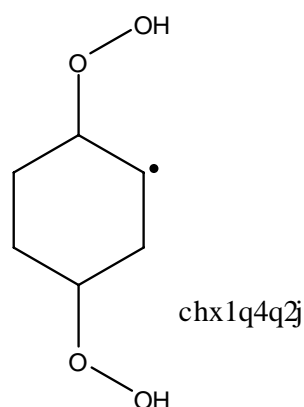
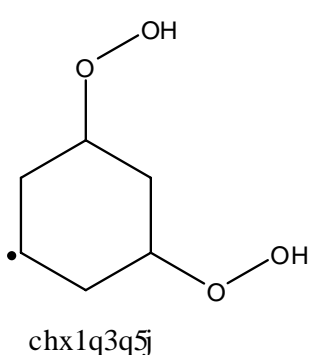
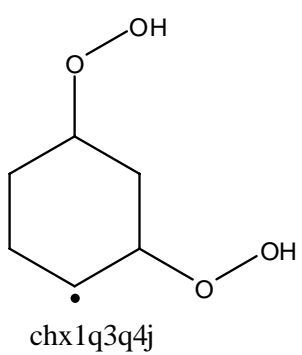
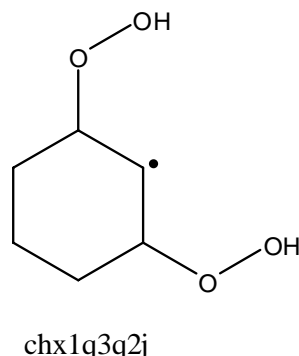
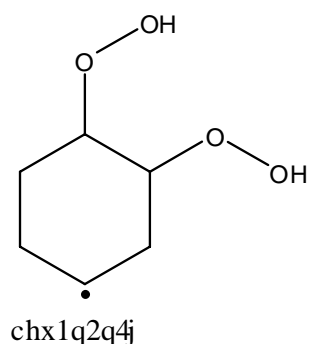
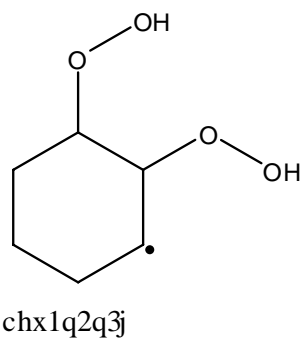


but14dial

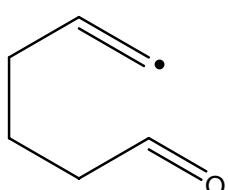
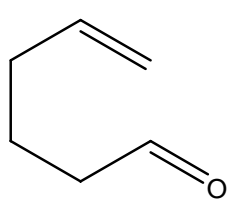
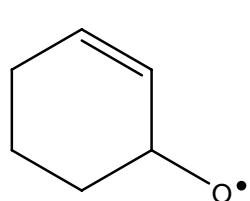
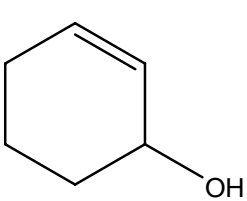
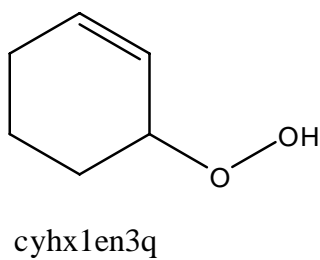


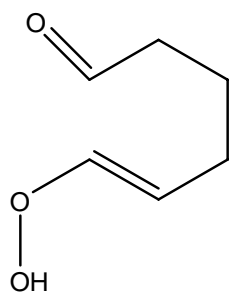
bt14al1j

O_2QOOH Alternatives:
Structure and naming of new species formed via this channel

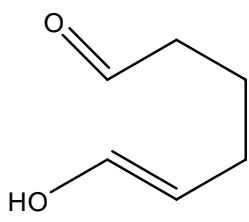


Decomposition of O_2QOOH Alternatives:
Structure and naming of new species formed via these channels

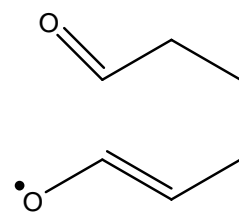




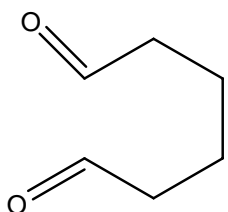
hx1n1q6al



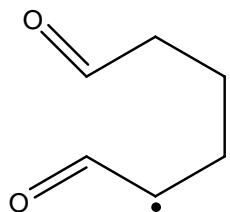
hx1nol6al



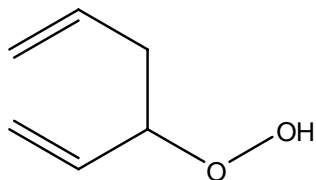
hx1noj6al



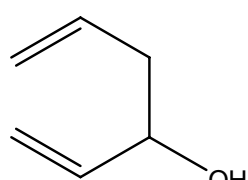
hex16dial
(duplicated here)



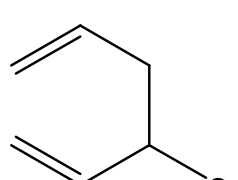
hx16al2j



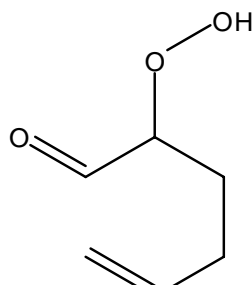
hex15en3q



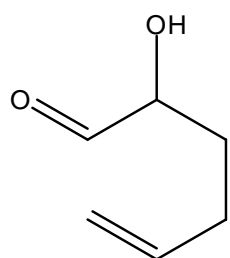
hx15en3ol



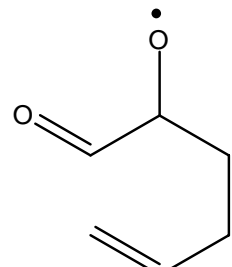
hx15en3oj



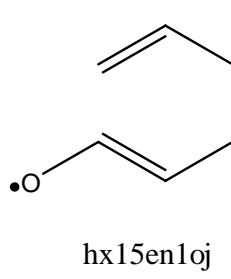
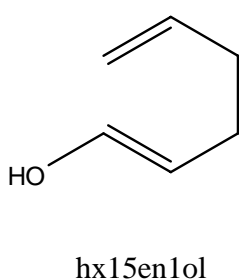
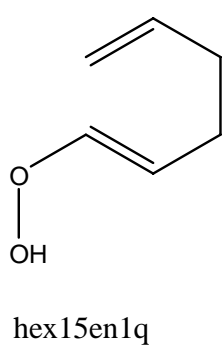
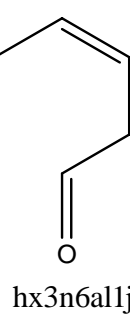
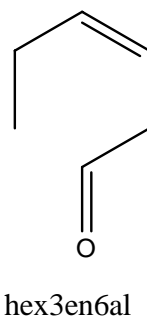
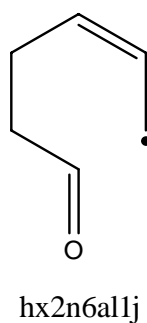
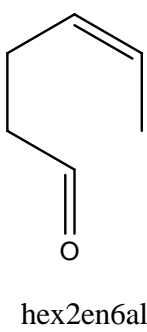
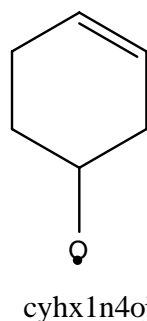
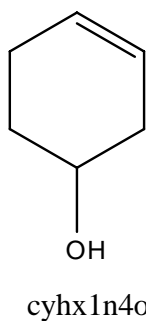
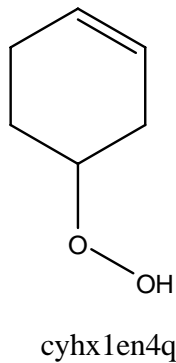
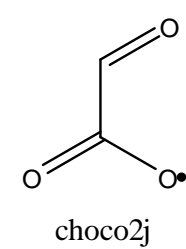
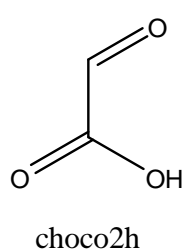
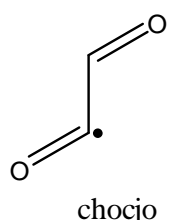
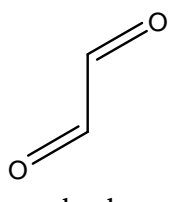
hx1n5q6al

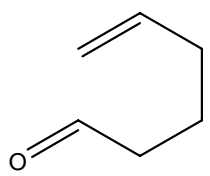


h1n5ol6al

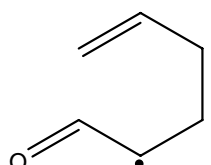


h1n5oj6al

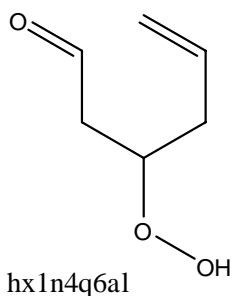




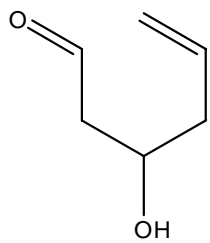
hex1en6al



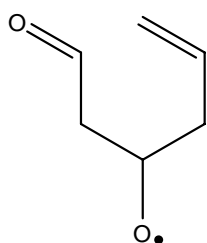
hx1n6al5j



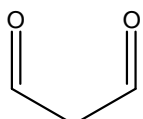
hx1n4q6al



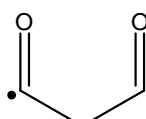
h1n4ol6al



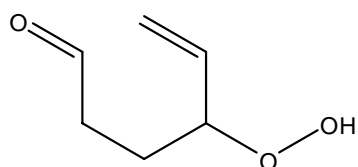
h1n4oj6al



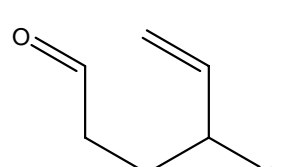
pro13dial



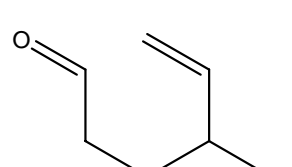
pro13al1j



hx1n3q6al



h1n3ol6al



h1n3oj6al

Appendix B

CanSen

CanSen is a Python script that I wrote to simplify the transition from Senkin-style, input-file-based usage to the Cantera-style script-based usage. The documentation included below is also available on the Web at <http://bryanweber.github.io/CanSen/html/index.html>.

CanSen Documentation

Release 1.1.0

Bryan W. Weber

April 14, 2014

CONTENTS

Summary	1
1 Installation and Usage Manual	2
1.1 CanSen Installation Guide	2
1.2 Usage	3
1.3 Supported Input Keywords	4
1.4 Internal Combustion Engine Model	10
1.5 Postprocessing	12
1.6 Code Documentation	14
2 Notice	19
3 License	20
4 Indices and tables	21
Python Module Index	22

Summary

CanSen is a Python script that provides a SENKIN-like wrapper around the open-source [Cantera](#) package. The motivation for this project is to ease the transition from SENKIN to using Cantera. Many researchers have knowledge of how to build SENKIN input files, and many may have SENKIN input files available that they use. CanSen enables the use of SENKIN-formatted input files with Cantera.

CanSen can be used with any version of Python ≥ 2.6 .

CanSen is hosted at [GitHub](#), if you are interested in the source code and development. Please report any bugs there.

INSTALLATION AND USAGE MANUAL

1.1 CanSen Installation Guide

CanSen can be installed on any platform that supports Python and Cantera. This guide contains instructions for Windows and Ubuntu 12.04.

CanSen has several dependencies, including:

- Cantera
- NumPy
- PyTables

1.1.1 Windows

Python can be downloaded and installed from the [Python.org](#) page. Installation instructions for Cantera on Windows can be found on the [Google code](#) page. Make sure to download the correct version for your Python and 32- or 64-bit Windows, depending on which version your OS is. If NumPy is not already installed, download the proper version from the [Windows Binaries](#) page. From the same page, download the installer for [PyTables](#) and its dependency [numexpr](#).

Then, download the most recent release of CanSen from [GitHub](#). Unzip the zip file, and you're ready to go!

Alternatively, you can use Git to download the developer version. **WARNING:** The developer version of CanSen is not guaranteed to be working at any given commit. Proceed with caution.:

```
git clone git://github.com/bryanweber/CanSen.git
```

will download the repository into a folder called CanSen.

1.1.2 Ubuntu

These instructions are for Ubuntu 12.04, but should work with only slight changes for most major releases of Linux. Optionally, download Python 3 from the apt repositories. At the same time, it is good to download some other dependencies:

```
sudo apt-get install python3 python3-dev libhdf5-serial-dev
```

Then, install distribute and pip:

```
wget https://bitbucket.org/pypa/setuptools/raw/bootstrap/ez_setup.py \
-O - | sudo python3.2
sudo easy_install-3.2 pip
```

or

```
wget https://bitbucket.org/pypa/setuptools/raw/bootstrap/ez_setup.py \
-O - | sudo python
sudo easy_install pip
```

Finally, with pip installed, install NumPy, Cython, numexpr, and finally, PyTables:

```
sudo pip-3.2 install numpy cython numexpr
sudo pip-3.2 install pytables
```

or

```
sudo pip install numpy cython numexpr
pip install pytables
```

Instructions for more complicated cases can be found on the [PyTables documentation](#).

Compilation/installation instructions for Cantera can be found in the [Cantera documentation](#).

Finally, get the most recent stable release of CanSen from [GitHub](#). Untar the tarball, and you're ready to go!

```
tar -xzf CanSen-X.Y.Z.tar.gz
```

Alternatively, you can use Git to download the developer version. **WARNING:** The developer version of CanSen is not guaranteed to be working at any given commit. Proceed with caution.:

```
git clone git://github.com/bryanwweber/CanSen.git
```

will download the repository into a folder called CanSen.

1.2 Usage

The following are instructions for usage of CanSen.

1.2.1 Windows

CanSen can be run from the command line (`cmd.exe`) or from within [IPython](#). From the command line, change into the directory with the CanSen script, and run:

```
py cansen.py [options]
```

In IPython, type:

```
In [1]: %run cansen.py [options]
```

1.2.2 Ubuntu

CanSen can be run either as an executable, or as a script with Python (2 or 3) or [IPython](#). To run as an executable, change to the directory where CanSen is located, add the execute bit to `cansen.py`, and run:

```
chmod +x cansen.py
./cansen.py [options]
```

To run as a script, change to the directory where CanSen is located and:

```
python3 cansen.py [options]
```

or

```
python cansen.py [options]
```

Or, in IPython:

```
In [1]: %run cansen.py [options]
```

1.2.3 Options

All of the previous commands have shown [options] to indicate where command line options should be specified. The following options are available, and can also be seen by using the -h or --help options:

```
-i:
    Specify the simulation input file in SENKIN format. Required.
-o:
    Specify the text output file. Optional, default: ``output.out``
-x:
    Specify the binary save output file. Optional, default:
    ``save.hdf``
-c:
    Specify the chemistry input file, in either CHEMKIN, Cantera
    CTI or CTML format. Optional, default: ``chem.xml``
-d:
    Specify the thermodynamic database. Optional if the
    thermodynamic database is specified in the chemistry input
    file. Otherwise, required.
--convert:
    Convert the input mechanism to CTI format and quit. If
    ``--convert`` is specified, the SENKIN input file is optional.
-h, --help:
    Print this help message and quit.
```

1.3 Supported Input Keywords

The following is a list of the currently supported keywords in the input file. Keywords that include “CanSen specific keyword” should be placed after the ‘END’ keyword to maintain SENKIN compatibility, although CanSen has no preference for the order.

```
ADD ATLS ATOL BORE CMPR CONP CONT CONV COTV CPRD
CRAD DEG0 DELT DTIGN DTSV END EQUI FUEL ICEN IGNBREAK
LOLR OXID PRES REAC RODL RPM RTLS RTOL SENS STPT
STROKE TEMP TIME TLIM TPRO TTIM VOL VOLC VOLD VPRO
VTIM
```

ADD: Mole fractions of species that should be included in the initial composition but excluded from the calculation of the equivalence ratio. Only valid when the equivalence ratio option is used to specify the composition. See [CPROD](#), [EQUI](#), [FUEL](#), [OXID](#), [REAC](#).

Example:

```
ADD Ar 0.1
```

ATLS: Absolute tolerance of the accuracy of the sensitivity coefficients. Optional keyword, default: 1E-06

Example:

```
ATLS 1E-06
```

ATOL: Absolute tolerance of the accuracy of the solution. Should be set smaller than the smallest meaningful species mass fraction. Optional keyword, default: 1E-20

Example:

```
ATOL 1E-20
```

BORE: CanSen specific keyword. Bore diameter of the engine cylinder. Units: cm.

Example:

```
BORE 1.0
```

CMPR: Specify the compression ratio for the internal combustion engine model. Defined as the maximum total volume in the cylinder divided by the clearance volume. See the [documentation](#). See also: [VOLC](#), [VOLD](#).

Example:

```
CMPR 10.0
```

CONP: Solve a constant pressure reactor with the energy equation on. One of [CONP](#), [CONT](#), [CONV](#), [COTV](#), [ICEN](#), [TPRO](#), [TTIM](#), [VPRO](#), or [VTIM](#) must be specified.

CONT: Solve a constant pressure reactor with the energy equation off. One of [CONP](#), [CONT](#), [CONV](#), [COTV](#), [ICEN](#), [TPRO](#), [TTIM](#), [VPRO](#), or [VTIM](#) must be specified.

CONV: Solve a constant volume reactor with the energy equation on. One of [CONP](#), [CONT](#), [CONV](#), [COTV](#), [ICEN](#), [TPRO](#), [TTIM](#), [VPRO](#), or [VTIM](#) must be specified.

COTV: Solve a constant volume reactor with the energy equation off. One of [CONP](#), [CONT](#), [CONV](#), [COTV](#), [ICEN](#), [TPRO](#), [TTIM](#), [VPRO](#), or [VTIM](#) must be specified.

CPROD: Complete products of stoichiometric combustion for the given fuel and oxidizer compositions. Only valid when the equivalence ratio option is used to specify the composition. All of the elements specified in the [FUEL](#) and [OXID](#) must be included in the set of species specified in **CPROD**. See [ADD](#), [EQUI](#), [FUEL](#), [OXID](#), [REAC](#).

Example:

```
CPROD H2O  
CPROD CO2
```

CRAD: CanSen specific keyword. Specify the crank radius. Units: cm.

Example:

```
CRAD 3.5
```

DEG0: Specify the initial crank angle of the simulation. Units: degrees. Default: 180 deg.

Example:

```
DEG0 180
```

DELT: Time interval for printing to the screen and the text output file. Optional keyword, default: [TIME](#)/100.Units: seconds.

Example:

```
DELT 1E-03
```

DTIGN: Temperature threshold used to determine the ignition delay. Ignition temperature is the initial temperature [TEMP](#) plus this value. Will be ignored for cases with the energy equation turned off. If both [DTIGN](#) and [TLIM](#) are specified, [TLIM](#) will override [DTIGN](#). See [TLIM](#). Optional keyword, default: 400. Units: K.

Example:

```
DTIGN 400
```

DTSV: Time interval for saving to the binary save file. Values are stored at the nearest time step to the save time interval. Optional keyword, by default, all time points are saved to the binary save file. Units: seconds.

Example:

```
DTSV 1E-05
```

END: Signifies the end of the input file in SENKIN. It is included in CanSen for compatibility with SENKIN input files, but does not do anything. Any CanSen specific keywords can be placed after [END](#) and the same input file can be used with SENKIN with no changes.

EQUI: Equivalence ratio desired for the initial mixture. If [EQUI](#) is specified, all of [COPROD](#), [FUEL](#), and [OXID](#) also must be specified, and [ADD](#) can be optionally specified. If [EQUI](#) is not specified, the reactants must be specified with [REAC](#). See [ADD](#), [COPROD](#), [FUEL](#), [OXID](#), [REAC](#).

Example:

```
EQUI 1.0
```

FUEL: Relative mole fractions of components in the fuel mixture for equivalence ratio calculations. The sum of the fuel mole fractions should be 1.0; if they are not, they will be normalized and a warning message will be printed. If [EQUI](#) is specified, [FUEL](#) must be specified. See [ADD](#), [CPROD](#), [EQUI](#), [OXID](#), [REAC](#).

Example:

```
FUEL CH4 1.0
```

ICEN: Specify the internal combustion engine model be used. See *the documentation for the model* for information on the derivation. See also [BORE](#), [CMPR](#), [CRAD](#), [DEGO](#), [LOLR](#), [RODL](#), [RPM](#), [STROKE](#), [VOLD](#), and [VOLC](#). One of [CONP](#), [CONT](#), [CONV](#), [COTV](#), [ICEN](#), [TPRO](#), [TTIM](#), [VPRO](#), or [VTIM](#) must be specified.

IGNBREAK: CanSen specific keyword. Indicates that the simulation should exit when ignition is encountered, instead of continuing until the end time [TIME](#) is reached. The criterion for ignition is specified by [DTIGN](#) or [TLIM](#). Optional keyword.

LOLR: Specify the ratio of the connecting rod length, ℓ , to the crank radius, a . See [RODL](#), [CRAD](#).

Example:

```
LOLR 3.5
```

OXID: Relative mole fractions of components in the oxidizer mixture for equivalence ratio calculations. The sum of the oxidizer mole fractions should be 1.0; if they are not, they will be normalized and a warning message will be printed. If [EQUI](#) is specified, [OXID](#) must be specified. See [ADD](#), [CPROD](#), [EQUI](#), [FUEL](#), [REAC](#).

Example:

```
OXID O2 1.0
OXID N2 3.76
```

PRES: Initial reactor pressure. Required keyword. Units: atmospheres.

Example:

```
PRES 1.0
```

REAC: Initial mole fraction of a reactant gas in the reactor. Required keyword if [EQUI](#) is not specified; however, only one of [REAC](#) or [EQUI](#) may be specified. If the mole fractions of the components given on [REAC](#) lines do not sum to 1.0, they will be normalized and a warning message will be printed.

Example:

```
REAC CH4 1.0
REAC O2 1.0
REAC N2 3.76
```

RODL: CanSen specific keyword. Specify the connecting rod length, ℓ . Units: cm.

Example:

```
RODL 5.0
```

RPM: Specify the rotation rate of the engine in revolutions per minute.

Example:

```
RPM 1500
```

RTLS: Relative tolerance of the accuracy of the sensitivity coefficients. Optional keyword, default: 1E-04

Example:

```
RTLS 1E-04
```

RTOL: Relative tolerance of the accuracy of the solution. Can be interpreted roughly as the number of significant digits expected in the solution. Optional keyword, default: 1E-08

Example:

```
RTOL 1E-08
```

SENS: Calculate sensitivity coefficients for the solution variables. The sensitivity coefficients are stored in a 2-D array, with dimensions of (number of solution variables, number of reactions). For [CONV](#), [COTV](#), [VPRO](#) and [VTIM](#) cases, the order of the sensitivity coefficients (i.e. the rows) is:

- 0 - mass
- 1 - volume
- 2 - temperature
- 3+ mass fractions of the species

For [CONP](#), [CONT](#), [TPRO](#), and [TTIM](#) cases, the order of the sensitivity coefficients (i.e. the rows) is

- 0 - mass
 - 1 - temperature
 - 2+ - mass fractions of the species
-

STPT: Maximum internal time step for the solver. Optional keyword. If any of [DELT](#), [DTSV](#), or [STPT](#) are specified, the minimum of these is used as the maximum internal time step. Otherwise, the default maximum time step is the end time [TIME](#)/100.

Example:

```
STPT 1E-5
```

STROKE: CanSen specific keyword. Specify the stroke length of the engine, L . Units: cm.

Example:

STROKE 7.0

TEMP: Initial reactor temperature. Required keyword. Units: K.

Example:

```
TEMP 800
```

TIME: End time for the integration. Unless, `IGNBREAK` is specified and its condition satisfied, the solver will integrate until `TIME` is reached. Required keyword. Units: seconds.

Example:

```
TIME 1E-03
```

TLIM: Ignition temperature. Ignition is considered to have occurred when this temperature is exceeded. If both `DTIGN` and `TLIM` are specified, `TLIM` overrides `DTIGN`. Optional keyword, default: `TEMP + 400`. Units: K.

Example:

```
TLIM 1200
```

TPRO: Warning: `TPRO` is broken in CanSen v1.1 due to incompatibilities with Cantera 2.1. Specify the reactor temperature as a function of time. Multiple invocations of this keyword build a profile of the temperature over the given times. This profile is linearly interpolated to set the reactor temperature at any solver time step. When the end time of the profile is exceeded, the temperature remains constant at the last specified value. One of `CONP`, `CONT`, `CONV`, `COTV`, `ICEN`, `TPRO`, `TTIM`, `VPRO`, or `VTIM` must be specified. Units: seconds, K.

Example:

```
TPRO 0.0 800  
TPRO 0.1 900
```

TTIM: Warning: `TTIM` is broken in CanSen v1.1 due to incompatibilities with Cantera 2.1. Specify the reactor temperature as a user-provided function of time. To use this keyword, the user must edit the `TemperatureFunctionTime` class in the `user_routines` file. Any parameters to be read from external files should be loaded in the `__init__` method so that they are not read on every time step. The parameters should be stored in the `self` instance of the class so that they can be accessed in the `__call__` method. The `__call__` method should contain the actual calculation and return of the temperature given the input `time`. One of `CONP`, `CONT`, `CONV`, `COTV`, `ICEN`, `TPRO`, `TTIM`, `VPRO`, or `VTIM` must be specified. Units: K.

VOL: Initial volume of the reactor. Optional keyword, default: `1E6 cm**3`. Units: `cm**3`.

Example:

```
VOL 1.0
```

VOLC: Specify the clearance volume, V_c . Units: `cm**3`. See `CMPR`, `VOLD`.

Example:

```
VOLC 1.0
```

VOLD: Specify the swept or displaced volume, V_d . Units: cm **3 . See [CMPR](#), [VOLC](#).

Example:

```
VOLD 10.0
```

VPRO: Specify the reactor volume as a function of time. Multiple invocations of this keyword build a profile of the volume over the given times. This profile is linearly interpolated to set the reactor volume at any solver time step. When the end time of the profile is exceeded, the volume remains constant at the last specified value. One of [CONP](#), [CONT](#), [CONV](#), [COTV](#), [ICEN](#), [TPRO](#), [TTIM](#), [VPRO](#), or [VTIM](#) must be specified. Units: seconds, m **3 .

Example:

```
VPRO 0.0 1E-5  
VPRO 0.1 1E-6
```

VTIM: Specify the reactor volume as a user-provided function of time. To use this keyword, the user must edit the `VolumeFunctionTime` class in the `user_routines` file. Any parameters to be read from external files should be loaded in the `__init__` method so that they are not read on every time step. The parameters should be stored in the `self` instance of the class so that they can be accessed in the `__call__` method. The `__call__` method should contain the actual calculation and must return the velocity of the wall given the input `time`. One of [CONP](#), [CONT](#), [CONV](#), [COTV](#), [ICEN](#), [TPRO](#), [TTIM](#), [VPRO](#), or [VTIM](#) must be specified. Units: m/s.

1.4 Internal Combustion Engine Model

The internal combustion engine model in CanSen is included to enable simulations of a reciprocating internal combustion engine. The equation of motion for the piston follows from Heywood¹, Ch. 2.

Assuming the piston roughly appears as in Fig. 1.1 where s is distance from the crank axis to the piston pin axis, ℓ is the connecting rod length, a is the crank radius, θ is the crank angle, with 0° at the top of the crank, L is the stroke length, B is the cylinder bore, V_d is the swept, or displacement, volume, V_c is the clearance volume, and TDC and BDC are top dead center and bottom dead center respectively (i.e. the top and bottom of the stroke).

The compression ratio of the cylinder is defined as:

$$r_c = \frac{V_d + V_c}{V_c}$$

The swept volume can either be specified directly, or can be calculated from the cylinder bore and stroke length:

$$V_d = L * \pi * \frac{B^2}{4}$$

The initial volume of the cylinder (the volume at BDC) is:

$$V_0 = V_d + V_c = r_c * V_c = \frac{V_d}{r_c - 1} + V_d$$

¹ John B. Heywood. *Internal Combustion Engine Fundamentals*. New York: McGraw Hill, 1988. Print.

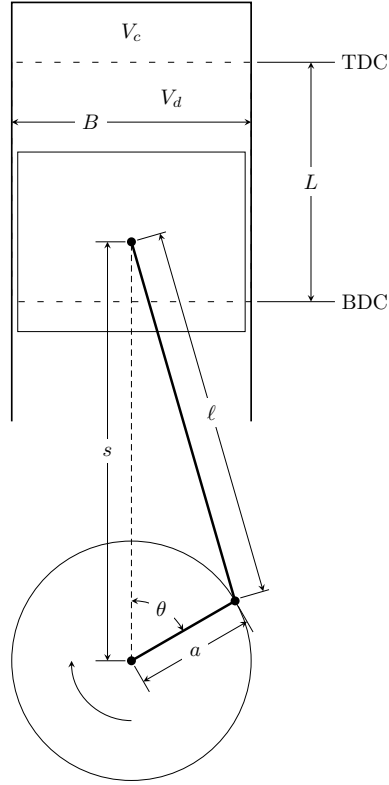


Figure 1.1: Model of piston

The distance from the crank center to the piston pin is given by:

$$s = a \cos(\theta) + \sqrt{\ell^2 - a^2 \sin^2(\theta)}$$

Cantera expects a moving wall to be given a velocity, so we find the piston velocity by differentiating with respect to time:

$$\frac{ds}{dt} = -a \sin(\theta) \frac{d\theta}{dt} + \frac{a^2 \sin(\theta) \cos(\theta) \frac{d\theta}{dt}}{\sqrt{\ell^2 - a^2 \sin^2(\theta)}}$$

Defining $\frac{d\theta}{dt}$, the angular velocity of the crank, as ω , and using the definition of the stroke length L and the connecting rod length to crank radius ratio R :

$$L = 2a$$

$$R = \frac{\ell}{a}$$

the equation for the velocity can be simplified to:

$$\frac{ds}{dt} = -\omega \frac{L}{2} \sin(\theta) \left[1 + \frac{\cos(\theta)}{\sqrt{R^2 - \sin^2(\theta)}} \right]$$

In CanSen, the angular velocity of the crank is input in revolutions per minute, so it must be converted to radians per second:

$$\frac{rad}{s} = RPM * \frac{\pi}{30}$$

By default, the starting crank angle is 180° , or BDC, 0° is TDC and the piston reaches BDC again at -180° . The starting crank angle can be set with the `DEG0` keyword, so θ is calculated as a function of time by:

$$\theta = \frac{DEG0 * \pi}{180} - \omega * t$$

1.5 Postprocessing

CanSen saves the solution information to a binary save file in a standard format called **HDF5**. Many programming and scripting languages have interfaces for HDF5 files, including **C++**, **MATLAB**, **Fortran 90** and Python. Notably, these are all of the interfaces that Cantera supports. The Python interface will be demonstrated in this tutorial, but the structure of the data and thus the main content of this tutorial will remain the same for all of the interfaces.

There are several Python interfaces for HDF5, but the one we will be using is called PyTables. The documentation for PyTables can be found on [their GitHub page](#).

Note that on the following lines, the `>>>` indicates that you should type the text at a Python prompt, not including the `>>>`. First, we will import the necessary libraries:

```
>>> import tables  
>>> import cantera as ct
```

If either of these don't work, make sure that PyTables and Cantera are both properly installed.

To print information about the save file, just type the name of its variable

```
>>> save_file
```

The data is saved in the save file with the Table format. Each Row in the Table represents one time step. Each Row further consists of a number of Columns where the data is stored. The Columns can be of arbitrary shape - thus, the entire 2-D sensitivity array is saved in one Column on each time step (i.e. in each row).

The format of the save file is hierarchical. The Table with each time step is stored in a Group, which is stored in the Root. It can be thought of as nested directories, with the Root as the top directory, then the Group, then the Table, like so:

```
Root  
| -Group  
|   | -Table
```

To access the information in the Table, it should be stored in a variable for quick access. The name of the Group in the save files from CanSen is `reactor`.

```
>>> table = save_file.root.reactor
```

The Table can now be used like any other class instance. In particular, the Table class defines a number of useful functions and attributes, such as `nrows`, which prints the number of rows in the Table.

```
>>> table.nrows
```

PyTables provides a method to iterate over the rows in a table automatically, called `iterrows`. Here we introduce one way to access information in a particular Column in the Table, by using natural name indexing. In this case, we print the value of the time at each time step.

```
>>> for row in table.iterrows():  
    print(row['time'])
```

Note that numerical indexing is also supported. The following is equivalent to the above:

```
>>> for row in table.iterrows():
    print(row[0])
```

The information stored by CanSen is written into case-sensitive columns named:

0. time
1. temperature
2. pressure
3. volume
4. massfractions
5. sensitivity

Columns 0-3 have a single value in each row. Column 4 (massfractions) contains a vector with length of the number of species in the mechanism. Column 5 is optional and included only if the user requested sensitivity analysis during the simulation. The dimensions of Column 5 are (n_vars, n_sensitivity_params).

In addition to the method of iterating through Rows, entire Columns can be accessed and stored in variables. First, all of the Columns can be stored in a variable.

```
>>> all_cols = table.cols
```

In this method, different Columns are accessed by their numerical index. The first index to `all_cols` gives the row and the second index gives the column number. Remembering that Python is zero-based, to access the mass fractions on the 4th time step, do

```
>>> mass_fracs_4 = all_cols[3][4]
```

Individual Columns can be stored in variables as well. This is done by the natural naming scheme.

```
>>> all_mass_fracs = table.cols.massfractions
```

This stores an instance of the Column class in `all_mass_fracs`. It may be more useful to store the data in a particular column in a variable. To do that, get a slice of the column by using the index and the colon operator. For instance, to store all of the mass fraction data in a variable

```
>>> all_mass_fracs = table.cols.massfractions[:]
```

Or, to store the fifth through tenth time steps

```
>>> mass_fracs_5_10 = table.cols.massfractions[4:9]
```

Or, to store every other time step from the sixth through the 20th

```
>>> mass_fracs_alt = table.cols.massfractions[5:19:2]
```

Once the data has been extracted from the save file, we need to actually be able to do something with it. Fortunately, Cantera offers a simple way to do this, by initializing a Solution to the desired conditions.

```
>>> gas = ct.Solution('mech.xml')
>>> for row in table.iterrows():
    gas.TPY = row['temperature'], row['pressure'], row['massfractions']
    print(gas.creation_rates)
```

This will print the creation rates of each species at each time step. Any method or parameter supported by the Solution class can be used to retrieve data at any given time step.

Further information about the PyTables package can be found at <http://pytables.github.io/usersguide/index.html> and information about Cantera can be found at <http://cantera.github.io/docs/sphinx/html/index.html>

1.6 Code Documentation

1.6.1 cansen module

`cansen.main (filenames, convert, version)`

The main driver function of CanSen.

Parameters

- **filenames** – Dictionary of filenames related to the simulation.
- **convert** – Boolean indicating that the user wishes only to convert the input mechanism and quit.
- **version** – Version string of CanSen.

`cansen.cansen (argv)`

CanSen - the SENKIN-like wrapper for Cantera written in Python.

Usage:

- i: Specify the simulation input file in SENKIN format. Required.
- o: Specify the text output file. Optional, default: `output.out`
- x: Specify the binary save output file. Optional, default: `save.hdf`
- c: Specify the chemistry input file, in either CHEMKIN, Cantera CTI or CTML format. Optional, default: `chem.xml`
- d: Specify the thermodynamic database. Optional if the thermodynamic database is specified in the chemistry input file. Otherwise, required.
- convert: Convert the input mechanism to CTI format and quit. If --convert is specified, the SENKIN input file is optional.
- h, -help: Print this help message and quit.

1.6.2 printer module

`class printer.Tee (name, mode)`

Bases: `builtins.object`

Write to screen and text output file

Initialize output.

Parameters

- **name** – Output file name.
- **mode** – Read/Write mode of the output file.

`close()`

Close output file and restore standard behavior

1.6.3 profiles module

`class profiles.VolumeProfile (keywords)`

Bases: `builtins.object`

Set the velocity of the piston by using a user specified volume profile. The initialization and calling of this class are handled by the `Func1` interface of Cantera. Used with the input keyword `VPRO`

Set the initial values of the arrays from the input keywords.

The time and volume are read from the input file and stored in the `keywords` dictionary. The velocity is calculated by assuming a unit area and using the forward difference, calculated by `numpy.diff`. This function is only called once when the class is initialized at the beginning of a problem so it is efficient.

Parameters `keywords` – Dictionary of keywords read from the input file

`__call__(t)`

Return the velocity when called during a time step.

Using linear interpolation, determine the velocity at a given input time `t`.

Parameters `t` – Input float, current simulation time.

`class profiles.TemperatureProfile(keywords)`

Bases: `builtins.object`

Set the temperature of the reactor by using a user specified temperature profile. The initialization and calling of this class are handled by the `Func1` interface of Cantera. Used with the input keyword `TPRO`

Set the initial values of the arrays from the input keywords.

The time and temperature are read from the input file and stored in the `keywords` dictionary as lists. This function is only called once when the class is initialized at the beginning of a problem so it is efficient.

`__call__(t)`

Return the temperature when called during a time step.

Using linear interpolation, determine the temperature at a given input time `t`.

Parameters `t` – Input float, current simulation time.

`class profiles.ICEngineProfile(keywords)`

Bases: `builtins.object`

Set the velocity of the wall according to the parameters of a reciprocating engine. The initialization and calling of this class are handled by the `Func1` interface of Cantera. Used with the input keyword `ICEN`.

Set the initial values of the engine parameters.

The parameters are read from the input file into the `keywords` dictionary.

`__call__(time)`

Return the velocity of the piston when called.

The function for the velocity is given by Heywood. See *Internal Combustion Engine Model*.

Parameters `time` – Input float, current simulation time

`class profiles.PressureProfile`

Bases: `builtins.object`

Dummy class for the pressure profile, to be implemented in CanSen v2.0

1.6.4 run_cases module

`class run_cases.SimulationCase(filenames)`

Bases: `builtins.object`

Class that sets up and runs a simulation case.

Initialize the simulation case.

Read the SENKIN-format input file is read into the `keywords` dictionary.

Parameters `filenames` – Dictionary containing the relevant file names for this case.

setup_case()

Sets up the case to be run. Initializes the ThermoPhase, Reactor, and ReactorNet according to the values from the input file.

run_case()

Actually run the case set up by `setup_case`. Sets binary output file format, then runs the simulation by using `ReactorNet.step(self.tend)`.

run_simulation()

Helper function that sequentially sets up the simulation case and runs it. Useful for cases where nothing needs to be changed between the setup and run. See `setup_case` and `run_case`.

reactor_state_printer(state, end=False)

Produce pretty-printed output from the input reactor state.

In this function, we have to explicitly pass in the reactor state instead of using `self.reac` because we might have interpolated to get to the proper time.

Parameters

- `state` – Vector of reactor state information.
- `end` – Boolean to tell the printer this is the final print operation.

1.6.5 user_routines module

class user_routines.VolumeFunctionTime

Bases: `builtins.object`

Calculate the volume of the reactor as a user specified function of time.

Set up the function to be calculated.

The init function should be used to import any parameters for the volume as a function of time from external files. Do not calculate the volume as a function of time here. Store all of the parameters in the `self` instance. The reason for this is to avoid running the `__init__` function on every time step. See the example below.

Example to load polynomial parameters from a file:

```
# Read the file into the list ''self.params''. The lines of
# the file are read as strings.
with open('file.txt','r') as input_file:
    self.params = input_file.readlines()
# Convert the strings to floats.
self.params = [float(param) for param in self.params]
self.area = 1 # m**2
```

__call__(time)

Return the velocity of the piston at the given time.

The call function should be where the implementation of the volume as a function of time is done. Cantera expects the velocity to be returned - $v = dV/dt * 1/A$. Get all of the needed parameters that were stored in the `self` instance. See the example below.

Example to use the previously stored polynomial parameters:

```

volume = (self.params[0] + self.params[1]*time +
          self.params[2]*time**2 + self.params[3]*time**3) # m**3
dvoldt = (self.params[1] + 2*self.params[2]*time +
          3*self.params[3]*time**2) # m**3/s
velocity = dvoldt/self.area # m/s
return velocity

```

class user_routines.TemperatureFunctionTime

Bases: builtins.object

Calculate the temperature of the reactor as a user specified function of time.

Set up the function to be calculated.

The init function should be used to import any parameters for the temperature as a function of time from external files. Do not calculate the temperature as a function of time here. Store all of the parameters in the `self` instance. The reason for this is to avoid running the `__init__` function on every time step. See the example below.

Example to load polynomial parameters from a file:

```

# Read the file into the list ''self.params''. The lines of
# the file are read as strings.
with open('file.txt','r') as input_file:
    self.params = input_file.readlines()
# Convert the strings to floats.
self.params = [float(param) for param in self.params]

```

`__call__(time)`

Return the velocity of the piston at the given time.

The call function should be where the implementation of the temperature as a function of time is done. Get all of the needed parameters that were stored in the `self` instance. See the example below. Note: None is not a valid return value, so this function does not work as written.

Example to use the previously stored polynomial parameters:

```

temperature = (self.params[0] + self.params[1]*time +
               self.params[2]*time**2 + self.params[3]*time**3) # K
return temperature

```

1.6.6 utils module

utils.convert_mech(mech_filename, thermo_filename)

Convert a mechanism and return a string with the filename.

Convert a CHEMKIN format mechanism to the Cantera CTI format using the Cantera built-in script `ck2cti`.

Parameters

- **mech_filename** – Filename of the input CHEMKIN format mechanism. The converted CTI file will have the same name, but with `.cti` extension.
- **thermo_filename** – Filename of the thermodynamic database. Optional if the thermodynamic database is present in the mechanism input.

utils.read_input_file(input_filename)

Read a formatted input file and return a dictionary of keywords.

Parameters `input_filename` – Filename of the SENKIN input file.

```
utils.cli_parser(argv)
```

Parse command line interface input.

Parameters *argv* – List of command line options.

```
utils.reactor_interpolate(interp_time, state1, state2)
```

Linearly interpolate the reactor states to the given input time.

Parameters

- **interp_time** – Time at which the interpolated values should be calculated
- **state1** – Array of the state information at the previous time step.
- **state2** – Array of the state information at the current time step.

```
utils.equivalence_ratio(gas, eq_ratio, fuel, oxidizer, complete_products, additional_species)
```

Calculate the mixture mole fractions from the equivalence ratio.

Given the equivalence ratio, fuel mixture, oxidizer mixture, the products of complete combustion, and any additional species for the mixture, return a string containing the mole fractions of the species, suitable for setting the state of the input ThermoPhase.

Parameters

- **gas** – Cantera ThermoPhase object containing the desired species.
- **eq_ratio** – Equivalence ratio
- **fuel** – Dictionary of molecules in the fuel mixture and the fraction of each molecule in the fuel mixture
- **oxidizer** – Dictionary of molecules in the oxidizer mixture and the fraction of each molecule in the oxidizer mixture.
- **complete_products** – List of species in the products of complete combustion.
- **additional_species** – Dictionary of molecules that will be added to the mixture. The mole fractions given in this dictionary are as a fraction of the total mixture.

**CHAPTER
TWO**

NOTICE

I have tested this software to the best of my abilities. Any user uses this software with the express understanding that there may be bugs, non-working features, and other gremlins that prevent a user from using the software to their specification. If you find problems, please report them in the [issue tracker](#).

ALL USERS ARE ENCOURAGED TO CHECK THEIR RESULTS WITH AN INDEPENDENT PROGRAM! Researchers especially are encouraged *not* to treat this software as a black box. Always remember: Garbage in equals garbage out!

**CHAPTER
THREE**

LICENSE

Also available in [LICENSE.txt](#)

The MIT License (MIT)

Copyright (c) 2014 Bryan W. Weber

Permission is hereby granted, free of charge, to any person obtaining a copy of this software and associated documentation files (the “Software”), to deal in the Software without restriction, including without limitation the rights to use, copy, modify, merge, publish, distribute, sublicense, and/or sell copies of the Software, and to permit persons to whom the Software is furnished to do so, subject to the following conditions:

The above copyright notice and this permission notice shall be included in all copies or substantial portions of the Software.

THE SOFTWARE IS PROVIDED “AS IS”, WITHOUT WARRANTY OF ANY KIND, EXPRESS OR IMPLIED, INCLUDING BUT NOT LIMITED TO THE WARRANTIES OF MERCHANTABILITY, FITNESS FOR A PARTICULAR PURPOSE AND NONINFRINGEMENT. IN NO EVENT SHALL THE AUTHORS OR COPYRIGHT HOLDERS BE LIABLE FOR ANY CLAIM, DAMAGES OR OTHER LIABILITY, WHETHER IN AN ACTION OF CONTRACT, TORT OR OTHERWISE, ARISING FROM, OUT OF OR IN CONNECTION WITH THE SOFTWARE OR THE USE OR OTHER DEALINGS IN THE SOFTWARE.

CHAPTER
FOUR

INDICES AND TABLES

- *genindex*
- *modindex*
- *search*

c

cansen, 14

p

printer, 14
profiles, 14

r

run_cases, 15

u

user_routines, 16
utils, 17